Polycrystalline CdS thin films and their role in CdS/CdTe photovoltaic devices

Martin David Archbold

How to cite:

Archbold, Martin David (2007) Polycrystalline CdS thin films and their role in CdS/CdTe photovoltaic devices. Doctoral thesis, Durham University.

Durham
University

Polycrystalline CdS thin films and their role in CdS/CdTe photovoltaic devices

By Martin David Archbold, MSci

A thesis presented in candidature for the degree of Doctor of Philosophy
in the University of Durham

Department of Physics
May 2007

Abstract

This thesis represents a systematic study of polycrystalline CdS thin films and their role as an *n*-type window layer in CdS/CdTe photovoltaic devices. This work encompasses the growth of CdS, primarily by the solution deposition method, and the subsequent characterisation of these films in isolation and as part of thin film CdS/CdTe device structures.

A novel solution deposition approach was devised in order to grow high quality CdS thin films. Structural, electrical and chemical characterisation methods applied to these have shown that in their as-grown state they are highly oriented (in either the c[111] or h[002] direction), possess a small grain size of approximately 10-15 nm, and contain a considerable level of compressive strain. Annealing treatments in the presence of the fluxing agent $CdCl_2$ have been shown to strongly modify the properties of these films, they are converted to a polycrystalline hexagonal structure with a significantly reduced level of strain, possess a larger grain size (27-28 nm) and a considerably enhanced crystalline quality.

Novel 'hybrid' films comprising two CdS layers grown by different growth methods, one grown directly upon the other, have been studied. It has been shown that there are remarkable differences in morphology between these and films grown by a single growth method alone.

Complete CdS/CdTe devices have been fabricated from several types of film grown in this study. Cell efficiencies of 9.80% were attained for a limited batch of devices, suggesting that these films possess good qualities for PV device fabrication.

Early results from a novel tubular photovoltaic device concept are presented. This geometry has the potential to reduce manufacturing costs, may open up new routes to enhance the efficiency of CdS/CdTe devices, and is an attractive candidate for PV/solar thermal power generation.

Declaration

I hereby declare that the work contained within this thesis is the work of the author. No part of this work has been previously submitted for any other degree or qualification.

CdTe and back contact growth for devices in section 7.4 was carried out by Dr Samantha Mazzamuto, Department of Physics, University of Parma, Italy.

Electrodeposition of CdTe material discussed in section 8.4 was carried out by Dr Anura Samantilleke, Department of Chemistry, University of Bath, UK.

Dr Douglas Halliday ....
Supervisor

Mr Martin Archbold ....
Candidate

Acknowledgements

I would like to express my warmest thanks to Dr Douglas Halliday for his guidance and kind support during my time under his supervision at Durham University.

I would also like to thank many colleagues, both at Durham and at other institutions, who have helped me immeasurably in undertaking and understanding my work. Thank you to Professor Ken Durose, Dr David Smyth-Boyle, Dr Kuveshni Govendar, Dr Tom Hase, Alex Pym, Dr Anura Samantilleke, Dr Chris Ottley, David Pattinson, Norman Thompson, Dr Vincent Barrioz, Dr Samantha Mazzamuto, Dr Del Atkinson, Dr Andy Brinkman and Dr Richard Thompson.

I would also like to thank many people for their friendship and help, people who have made living and working at Durham a pleasure. Thanks to Chris Hodgeson, Jon Major, Guillaume Zoppi, Tom Hindmarch, Keriya Mam, Yuri Proskuryakov, Mohammed Alturkestani and Ben Cantwell.

Dedication

This thesis is dedicated to three special people in my life, to my parents John and Jeanette who have cared for me, taught and guided me and have always been there to help me, and to Julia, a warm, caring and fun person whom I am fortunate to know and share my life with.

Contents

List of symbols

AM_0	Air mass factor 0	-
$AM_{1.5}$	Air mass factor 1.5	-
B	Magnetic induction	$\mathrm{Wbm^{-1}}$
c	Lattice constant	Å
C_1, C_2	Correction factors	-
d	Film thickness	m
d_{hkl}	Lattice spacing	Å
D_n, D_p	Electron (hole) diffusion constant	$\mathrm{cm^2s^{-1}}$
e	Electronic charge	C
E_a	Acceptor bound energy level	eV
E_C	Conduction band edge energy	eV
E_d	Donor bound energy level	eV
E_g	Bandgap energy	eV
E_i	Intrinsic energy level	eV
E_V	Valence band edge energy	eV
E_{vac}	Vacuum level energy	eV
$E(x)$	Electric field vector	$\mathrm{Vm^{-1}}$
FF	Fill factor	-
$\hbar$	Planck's constant	Js
I_{mp}	Current at maximum power point	mA
I_{sc}	Short circuit current	mA
J	Current density	$\mathrm{mAcm^{-2}}$
J_0	Saturation current density	$\mathrm{mAcm^{-2}}$
J_{dark}	Dark current density	$\mathrm{mAcm^{-2}}$
J_{mp}	Current density at maximum power point	$\mathrm{mAcm^{-2}}$
J_n, J_p	Current density for electrons (holes)	$\mathrm{mAcm^{-2}}$

J_{ph}	Photocurrent current density	mAcm^{-2}
J_{sc}	Short circuit current density	mAcm^{-2}
k	Wavenumber	m^{-1}
k_B	Boltzmann's constant	JK^{-1}
K_{sp}	Solubility product	-
L_n, L_p	Electron (hole) diffusion length	cm
m_c^*	Conduction band effective mass	Kg
m_V^*	Valence band effective mass	Kg
n	Electron number density	cm^{-3}
n_i	Intrinsic carrier density	cm^{-3}
n_s	Electron sheet carrier density	cm^{-3}
n_n, p_n	Electron (hole) density in *n*-type semiconductor	cm^{-3}
n_p, p_p	Electron (hole) density in *p*-type semiconductor	cm^{-3}
n_{n0}, p_{n0}	Equilibrium electron (hole) density in *n*-type semiconductor	cm^{-3}
n_{p0}, p_{p0}	Equilibrium electron (hole) density in *p*-type semiconductor	cm^{-3}
N_A	Donor density	cm^{-3}
N_C	Effective density of states in the conduction band	cm^{-3}
N_D	Acceptor density	cm^{-3}
N_V	Effective density of states in the valence band	cm^{-3}
p	Hole number density	cm^{-3}
p_s	Hole sheet carrier density	cm^{-3}
ppb, ppt	Parts per billion/trillion	-
P_{in}	Input power	Js^{-1}
P_{mp}	Power at maximum power point	Js^{-1}
P_{out}	Output power	Js^{-1}
q	Magnitude of electronic charge	C
R_s	Sheet resistance	$\Omega\square^{-1}$
R_{series}	Series resistance	Ω

R_{shunt}	Shunt resistance	Ω
t	Film thickness	m
T	Temperature	K
V_{bi}	Built-in voltage	V
V_H	Hall voltage	V
V_{mp}	Voltage at maximum power point	V
V_{oc}	Open circuit voltage	V
$V(x)$	Electrostatic potential	V
x_n, x_n	Junction region limits	m
α	Lattice constant	Å
Γ	Broadening parameter	e
$\Delta(2\theta)$	Diffraction peak broadening	rad
ε	Electric permittivity	Fm^{-1}
ε_0	Electric permittivity of free space	Fm^{-1}
η	Efficiency	-
η_H	Hall mobility	$cm^2v^{-1}s^{-1}$
κ	Scherrer constant	-
λ	Wavelength	m
μ	Reduced electron-hole mass	Kg
μ_n	Electron mobility	$cm^2V^{-1}s^{-1}$
μ_p	Hole mobility	$cm^2V^{-1}s^{-1}$
ν	Frequency	s^{-1}
ρ, ρ_0	Resistivity	$\Omega\, cm^{-1}$
$\rho(x)$	Charge density	Ccm^{-3}
σ	Conductivity	$\Omega^{-1}\, cm$
ϕ_m	Work function of a metal	eV
ϕ_n	Work function of an *n*-type semiconductor	eV
ϕ_p	Work function of a *p*-type semiconductor	eV
ϕ_b	Barrier height	eV

ϕ, φ	Electrostatic potential	V
χ	Electron affinity	eV
ω	Angular frequency	s^{-1}

1. Introduction

1.1. Climate change

There is now significant scientific evidence which shows that climate change is a serious threat to human existence [1]. The mean global temperature of the Earth has risen dramatically in the last 150 years [2], fuelled by substantial increases in the production, and consequent incorporation into the atmosphere, of carbon dioxide (CO_2) and other greenhouse gasses (Figures 1.1a, b). If this rise in emissions continues, climate models predict an unprecedented increase in mean global temperature [3] which will likely result in adverse and dramatic changes to the geography of our environment.

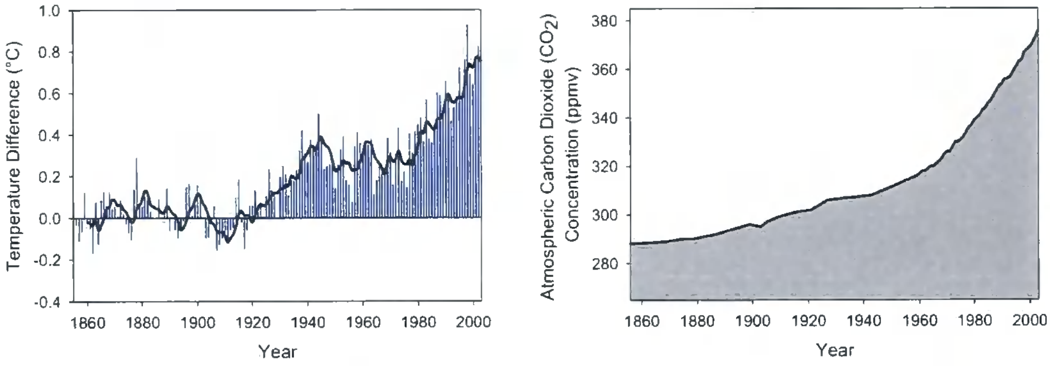

Figure 1.1. a) Global average temperatures have risen dramatically in the last 150 years [2], largely due to b) the acceleration in production of the greenhouse gas CO_2.

The most evident solution to this problem is to substantially reduce emissions of greenhouse gasses, in particular CO_2, in order to achieve this we must develop clean, efficient, renewable sources of energy. Photovoltaic (PV) cells which convert sunlight directly into electricity are presently one of the leading potential candidates to supply this energy.

1.2. The sun as an energy source

The Earth's surface receives a continuous supply of over 120,000 TJ (12×10^{16} J) of energy from the sun in the form of electromagnetic radiation each second, this is sufficient to supply the world's entire annual energy requirement in less than one hour. Figure 1.2 shows the average local solar irradiance impinging on the surface of the Earth, the black square positioned over the Sahara desert in Northern Africa represents the area of PV cells which would be required in order to generate the current world's energy requirement, assuming only a modest 10% PV cell efficiency. It is clear from this figure that the land area needed to supply our power requirements is reasonable in comparison with the vast regions which have already been industrialised or mined in order to cater for our energy needs.

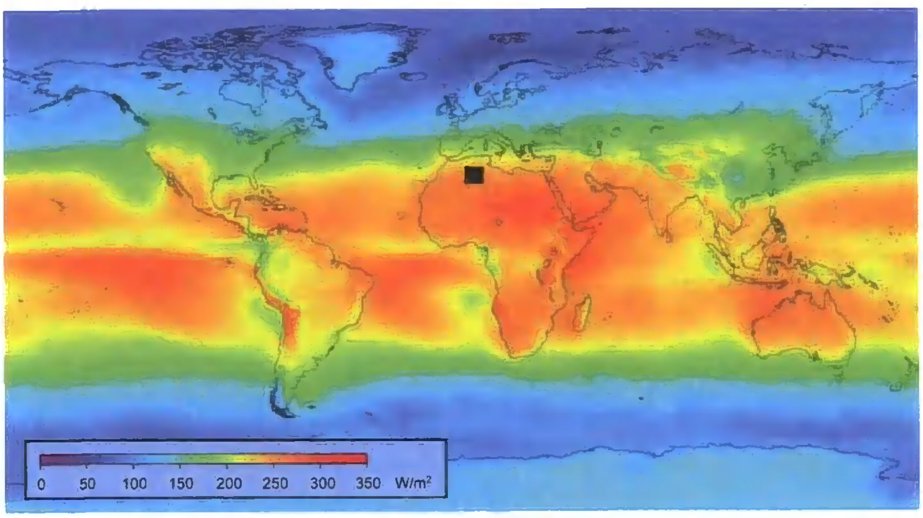

Figure 1.2. Mean solar irradiance averaged over 24 hours which impinges on the surface of the earth [4-8].

At the top of the atmosphere, the total power density summed over all wavelengths is known as the solar constant, this has a value of 1370 Wm^{-2}. The spectrum of this radiation is changed in shape and significantly attenuated by absorption and scattering effects due to the earth's atmosphere. As a greater path length will incur a larger attenuation, this path length is quantified by an *air mass factor* (AM_i), where i is defined as the ratio of the optical path length through the atmosphere to the optical path length through the atmosphere if the sun is directly overhead, this is given by:

$$i = \mathrm{cosec}(\theta) \tag{1.1}$$

where θ is the angle from the incident ray to the vertical, as shown in Figure 1.3.

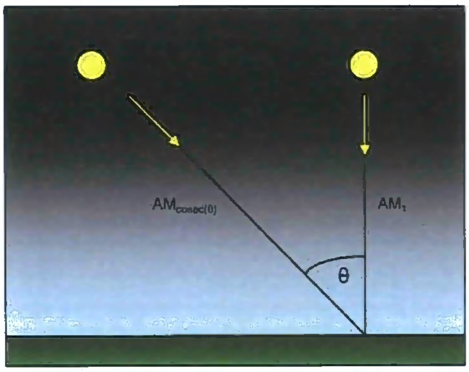

Figure 1.3. Air mass factor.

Although the choice of air mass factor is arbitrary, a value of $AM_{1.5}$ (θ=42°) is often chosen for standard reference and comparison in laboratory work. The corresponding energy spectrum is shown in figure 1.4 along with two additional spectra, AM_0 which corresponds to that directly above the Earth's atmosphere, and the blackbody spectrum at an effective temperature of 5760 K, the approximate surface temperature of the Sun. Attenuation effects due to the atmosphere are apparent at wavelengths < 300 nm due to atomic and molecular oxygen, whilst water vapour and CO_2 gas are mainly responsible for attenuation in the 900-2600 nm region.

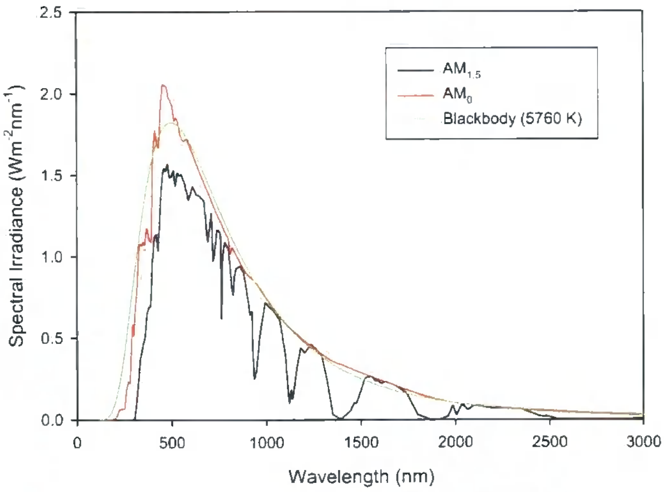

Figure 1.4. Solar irradiance as a function of wavelength for AM_0 and $AM_{1.5}$ spectra, compared with a blackbody spectrum having a characteristic temperature of 5760 K.

It is important to note that although the mean irradiance of the $AM_{1.5}$ spectrum (total energy summed over all wavelengths) is approximately 900 Wm^{-2}, this is generally normalised to 1000 Wm^{-2} for numerical convenience. When quoting efficiency values for PV devices, the standard spectrum used is $AM_{1.5}$ normalised to 1000 Wm^{-2} (equivalent to 100 $mWcm^{-2}$), this is generated in practise by using the approximately blackbody spectrum of a tungsten halogen light source attenuated by appropriate filters, refer to section 4.3.2 for experimental details.

1.3. Historical background

The PV effect was first discovered by Edmond Becquerel in 1839 upon observing that the action of light on a platinum electrode immersed in a liquid electrolyte produced an electric current. Although the magnitude of this effect was too small to be useful for energy generation, it nonetheless found many applications and as a consequence stimulated much research work in order to further understand the effect. The next significant development arose from the discovery in 1873 by Smith of the photoconductive effect in selenium, closely followed three years later by the discovery of the same effect in selenium by Adams and Day [9]. The latter experiment consisted of a solid piece of selenium with heated platinum contacts, and was the first demonstration of the PV effect in a solid-state system. In 1883 the American inventor Fritts [10] produced the first thin-film PV device by applying a layer of gold leaf to a thin layer of selenium; he was also one of the first to recognise the enormous potential of PV devices, and took out many patents over his lifetime. In 1914 Goldman and Brodsky were the first to relate the operation of this type of cell to a rectifying action, however it was not until the 1930's that the metal-semiconductor junction effect was put on a firm theoretical footing by Schottky, Mott and others. In the 1950's the intense research interest in semiconductor materials and the production of high purity silicon wafers for microelectronics applications brought about the development of PV devices in which useful amounts of power could now be extracted. In 1954 Chapin [11] produced a crystalline silicon device with an efficiency of 6%, closely followed by an improvement to 11% one year later. At this time there was an intense research effort in satellite technology, photovoltaic cells were found to be ideal satellite power sources and in 1958 the first PV powered satellite Vanguard I was launched (Figure 1.5). The six single crystal silicon panels produced 0.1 W of power and operated successfully for over eight years.

Figure 1.5. The first PV powered satellite Vanguard 1, measuring only 15 cm in diameter and weighing 1.5 kg it had six single crystal silicon PV cells (four are visible in the above image).

With the 1970's oil crisis there was a renewed interest in terrestrial PV, and many classes of devices were researched, with the emphasis on large area and cost reduction. This motivated a great deal of research into thin-film devices such as CdS/Cu_2S, amorphous silicon, CdS/CIGS and the main object of this current study, the CdS/CdTe device.

1.4. Current status and research interest

The amount of energy currently produced by PV devices is insignificant (< 1%) in comparison to conventional fossil fuel, nuclear and hydroelectric power sources, however a massive expansion in PV production and installation is presently taking place. Figure 1.6 shows the cumulative installed PV capacity over that last decade, this reveals a significant uptrend, and an even higher growth rate is predicted in the future.

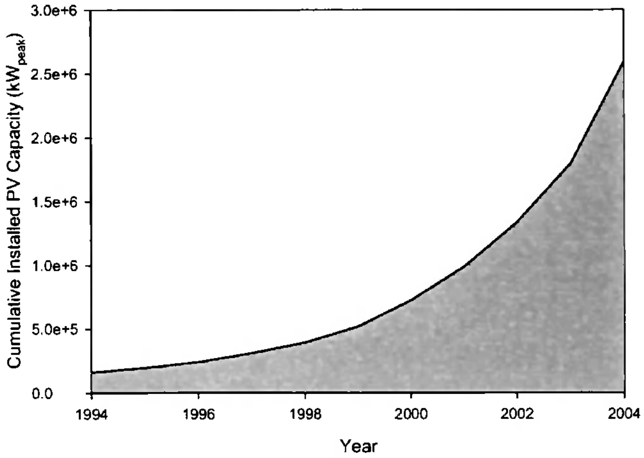

Figure 1.6. Cumulative worldwide installed PV capacity.

At the present time the vast majority of commercial PV production is in silicon devices, whether in single crystal, polycrystalline or multi-crystalline form; this is due to silicon being an established technology and thus there are many standard industrial processes which are well researched and produce consistent and highly optimised devices. Thin film PV installations account for around only 6% of market share, the majority of this being amorphous silicon with the remainder consisting of CdS/CdTe and CdS/CIGS. Both CdS/CdTe and CdS/CIGS PV technologies are maturing quickly and are currently emerging as a major force, with several manufacturers now producing significant output.

Research in the area of PV materials and devices has never been more active. Advances are constantly being made in many diverse areas of materials science and engineering which are directly relevant to PV. Some recent advances include devices incorporating nano-materials and quantum dot structures, major efficiency improvements in dye sensitised and organic PV cells, the exploration of photonic bandgap materials and the precise engineering of tandem and multiple bandgap designs which now lend themselves to use in commercial scale concentrator systems. The growth in these technologies and the associated understanding of the physics involved will unquestionably lead to advances in PV device technology in the coming years.

1.5. References

1. Stern, N., *Stern Review on the Economics of Climate Change.* HM Treasury Independent review, 2006.

2. Brohan, P., J.J. Kennedy, I. Harris, S.F.B. Tett, and P.D. Jones, *Uncertainty estimates in regional and global observed temperature changes: A new data set from 1850.* Journal of Geophysical Research-Atmospheres, 2006. **111**(D12).

3. Wigley, T.M.L. and S.C.B. Raper, *Interpretation of high projections for global-mean warming.* Science, 2001. **293**(5529): p. 451-454.

4. Loster, M., *Total primary energy supply: Land area requirements.* 2006. (Accessed:02/08/2006). http://www.loster.com/ml/solar_land_area

5. NGDC, *National Geophysical Data Center (NGDC), NOAA Satellite and Information Service, Coastline Extractor.* (Accessed:02/08/2006). http://rimmer.ngdc.noaa.gov/mgg/coast/

6. Bishop, J.K.B. and W.B. Rossow, *Spatial and Temporal Variability of Global Surface Solar Irradiance.* Journal of Geophysical Research-Oceans, 1991. **96**(C9): p. 16839-16858.

7. ISCCP, *International Satellite Cloud Climatology Project.* (Accessed:02/08/2006). http://isccp.giss.nasa.gov/

8. IEA, *International Energy Agency - Key World Energy Statistics 2005.* (Accessed:02/08/2006). http://www.iea.org/

9. Adams, W.G. and R.E. Day, *The action of light on selenium.* Proceedings of the Royal Society A, 1876. **25**: p. 113–117.

10. Fritts, C.E., *A new form of selenium cell.* American Journal of Science, 1883. **26**: p. 465–472.

11. Chapin, D.M., C.S. Fuller, and G.L. Pearson, *A New Silicon P-N Junction Photocell for Converting Solar Radiation into Electrical Power.* Journal of Applied Physics, 1954. **25**(5): p. 676-677.

2. Fundamentals of photovoltaic devices

2.1. Introduction

PV devices rely on the fundamental electrical and optical properties of their constituent solid state materials; in this chapter an overview is given of the three general classifications of materials: metals, semiconductors and insulators. The PV effect is then introduced, focussing on common device configurations, and then the physics of the device commonly used in this work, the *p-n* junction is explained in detail. Finally, real-world PV devices are described, including common parameters used in their characterisation, and real-world effects are discussed with emphasis on the consequences that these have on device performance.

2.2. Metals, semiconductors and insulators

Solid state materials can generally be assigned to one of three categories: metals, semiconductors or insulators, depending on the ease with which they conduct an electric current. Table 2.1 shows electrical resistivity values for three materials, gold, silicon and polytetrafluoroethylene (PTFE), which belong to these groupings; their resistivities span a huge 24 orders of magnitude.

Material	**Resistivity (Ω cm)**	**Classification**
Gold	2.2×10^{-6}	Metal
Silicon	$\sim 2.4 \times 10^{5}$	Semiconductor
PTFE	$> 1 \times 10^{18}$	Insulator

Table 2.1. Resistivity values for gold (metal), silicon (semiconductor) and PTFE (insulator) at room temperature. For silicon the intrinsic donor concentration is 1.22×10^{10} cm^{-3} [1-3].

This enormous range can be explained by band theory. In a crystalline solid the atoms are packed into a regular three dimensional structure which is determined by the atom type; as these atoms are densely packed the outer orbitals will overlap causing the discrete electron energy levels in the free atoms to be broadened into bands. Figure 2.1 shows a simplified schematic of the electron occupancy levels in the three cases at room temperature.

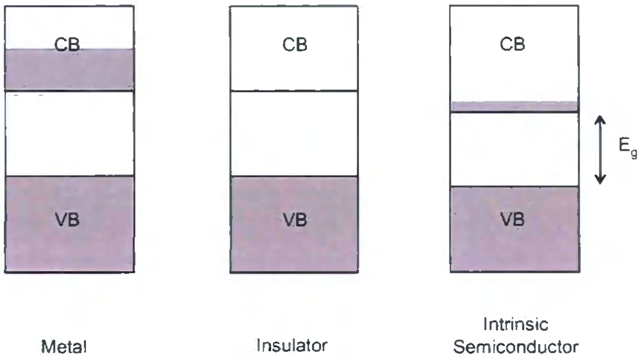

Figure 2.1. Schematic of the electron occupancy levels for a monovalent metal, insulator and intrinsic semiconductor material. Shading indicates electron occupancy levels.

General features include the valence band (VB) which contains valence electrons used in bonding, the conduction band (CB) containing conduction electrons which are free to move throughout the material, and the forbidden energy gap (E_g) which is the energy difference of the CB and VB edges:

$$E_g = E_c - E_v \qquad (2.1)$$

In a metal (here only a monovalent metal is considered, for simplicity) there are many unfilled electron energy states in the CB, thus if electrons in the CB are acted upon by an electromagnetic (EM) field these electrons can easily be perturbed to a higher energy state and therefore these conduction electrons are free to move in the solid and so metals have low electrical resistivities. In an insulator there are very few electrons in the CB and the VB is fully occupied, as the VB electrons are bound (they cannot respond to small perturbations by an EM field as there are no unfilled energy states for the electron to move into) there can be little conduction in the solid, therefore insulators have high electrical resistivity values. In the case of an intrinsic semiconductor the band schematic is similar to that of an insulator; however E_g is generally smaller than that of an insulator, and so at room temperature some electrons may be thermally excited to the CB where they can take part in conduction, therefore the electrical resistivity of an intrinsic semiconductor is between that of a metal and insulator at finite temperature. The behaviour as described above is fully quantified in the nearly free electron model, where Schrödinger's equation is solved taking into account the infinite array of periodic atomic potentials throughout the crystal lattice; for a full treatment see Kittel [4]. An example energy-wavevector band structure diagram for a direct gap semiconductor near k = 0 is shown in Figure 2.2 (note that for simplicity multiple-hole bands have been omitted).

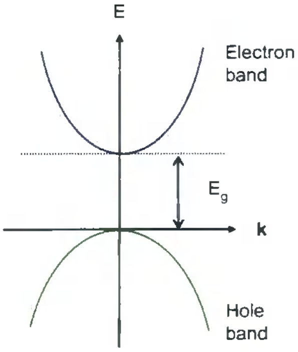

Figure 2.2. Band structure diagram for a direct bandgap semiconductor.

It can be shown that the density of states (DOS) function for a semiconductor with this band structure is given by:

$$g(\hbar\omega) = 0 \qquad \text{for } \hbar\omega < E_g \qquad (2.2)$$

$$g(\hbar\omega) = \frac{1}{2\pi^2}\left(\frac{2\mu}{\hbar^2}\right)^{3/2}\left(\hbar\omega - E_g\right)^{1/2} \qquad \text{for } \hbar\omega \geq E_g \qquad (2.3)$$

where μ is the reduced electron-hole mass. By using Fermi's golden rule:

$$W_{i\to f} = \frac{2\pi}{\hbar}|M|^2 g(\hbar\omega) \qquad (2.4)$$

where W is the quantum mechanical transition rate for exciting an electron from an initial to a final quantum state by absorption of a photon of angular frequency ω, and

M is the matrix element [5], it is apparent that for photon energies greater than the bandgap the transition rate (and hence the absorption coefficient) will rise as a factor of $(\hbar\omega - E_g)^{1/2}$.

$$\alpha(\hbar\omega) = 0 \qquad \text{for } \hbar\omega < E_g \tag{2.5}$$

$$\alpha(\hbar\omega) \propto (\hbar\omega - E_g)^{1/2} \qquad \text{for } \hbar\omega \geq E_g \tag{2.6}$$

This model must be modified in order to describe the absorption coefficients of indirect bandgap materials, however all the materials used in this study possess direct bandgaps. Figure 2.3a shows the calculated energy band structure for CdS in the hexagonal wurtzite modification, with the Brillouin zone of the wurtzite lattice shown in Figure 2.3b for reference [6].

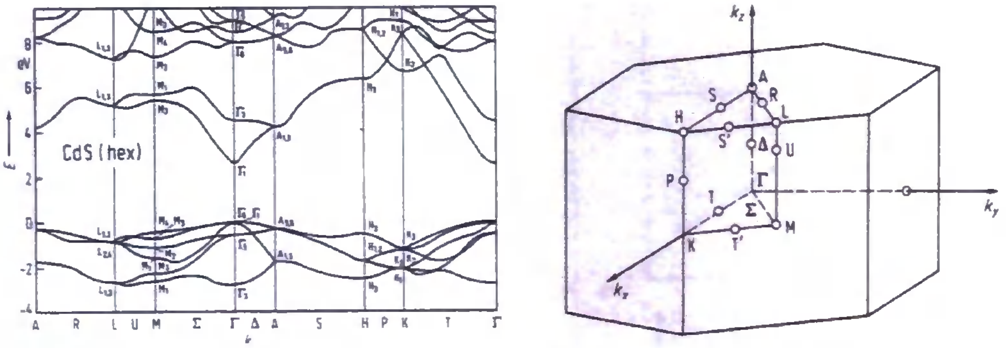

Figure 2.3. a) Band energy structure for CdS in the hexagonal modification and b) the corresponding Brillouin zone scheme.

2.2.1. Intrinsic semiconductors

The electrical properties of an intrinsic semiconductor are defined only by the structure of the pure material. The properties of such a semiconductor will be considered, and then extended to extrinsic semiconductors in which the presence of dopant impurities substantially affect the electrical properties of the material.

An electron in a semiconductor will occupy the lowest available energy level, filling up vacant states in order of increasing energy; the energy up to which states are filled is called the Fermi energy (E_F). At finite temperatures the electrons will possess kinetic energy through thermal interactions, and therefore a proportion (with $E > E_g$) will be excited into states above E_F, leaving unoccupied states in the VB. These unoccupied states are equivalent to the absence of an electron, and can be treated as a positively charged carrier called a *hole*. In order to calculate the number density of electrons (n) in the CB (and analogously the number density of holes in the VB (p)) we first need to find the number density per energy interval dE, this is given by:

$$n(E)dE = g(E)f(E)dE \qquad (2.7)$$

where $g(E)$ is the DOS function and $f(E)$ is the probability that a state at a certain energy and temperature will be occupied. This quantity is integrated from the CB edge to infinity to give us the electron density in the CB:

$$n = \int_{E_c}^{\infty} g(E)f(E)dE \qquad (2.8)$$

where the DOS function (cf. Equation 2.3) for the conduction band is given by:

$$g(E) = \frac{1}{2\pi^2}\left(\frac{2m_c^*}{\hbar^2}\right)^{3/2}(E - E_c)^{1/2} \qquad (2.9)$$

where m_c^* is the CB effective mass and E_c is the conduction band edge (where the wavevector $\boldsymbol{k}$ is taken to be zero). The probability of state occupancy is given by the Fermi Dirac distribution function:

$$f(E) = \frac{1}{\exp\left(\frac{E - E_F}{k_B T}\right) + 1} \tag{2.10}$$

As the Fermi level E_F lies in the bandgap we can assume that $E >> E_F$, thus equation 2.10 simplifies to the Maxwell-Boltzmann form:

$$f(E) \approx \exp\left(\frac{E_F - E}{k_B T}\right) \tag{2.11}$$

In this form equation 2.8 can be evaluated using equations 2.9 and 2.10 exactly to give:

$$n = N_c \exp\left(\frac{E_F - E_c}{k_B T}\right) \tag{2.12}$$

where N_c is the effective density of states in the conduction band:

$$N_c = 2\left(\frac{m_c^* k_B T}{2\pi\hbar^2}\right)^{3/2} \tag{2.13}$$

The same process can be applied to holes in the valence band, to give:

$$p = N_v \exp\left(\frac{E_v - E_F}{k_B T}\right) \tag{2.14}$$

where N_v is the effective density of states in the valence band:

$$N_v = 2\left(\frac{m_v^* k_B T}{2\pi\hbar^2}\right)^{3/2} \tag{2.15}$$

where m_v^* is the VB effective mass. Equations 2.12 and 2.14 show that the electron and hole densities vary exponentially with the position of the Fermi level in the bandgap. If we take the product of the electron and hole densities:

$$np = N_c N_v \exp\left(\frac{E_F - E_c}{k_B T}\right) \exp\left(\frac{E_v - E_F}{k_B T}\right) \tag{2.16}$$

$$np = N_c N_v \exp\left(\frac{E_v - E_c}{k_B T}\right) \tag{2.17}$$

$$np = N_c N_v \exp\left(-\frac{E_g}{k_B T}\right) \tag{2.18}$$

It is apparent that this is a constant for the material at a specified temperature, and is often written as:

$$n_i^2 = np \tag{2.19}$$

$$n_i = (N_c N_v)^{1/2} \exp\left(-\frac{E_g}{2k_B T}\right) \tag{2.20}$$

where n_i is the intrinsic carrier density and is equal to the density of electrons which are thermally excited into the conduction band of a pure semiconductor in thermal equilibrium. As each excited electron leaves a corresponding hole, n_i is also equal to the number of holes left behind in the valence band. Often the electron and hole densities are stated in terms of the intrinsic energy level E_i:

$$n = n_i \exp\left(\frac{E_F - E_i}{k_B T}\right) \tag{2.21}$$

$$p = n_i \exp\left(\frac{E_i - E_F}{k_B T}\right) \tag{2.22}$$

where:

$$E_i = \frac{1}{2}(E_c + E_v) - \frac{1}{2}k_B T \ln\left(\frac{N_c}{N_v}\right) \qquad (2.23)$$

In a pure semiconductor at equilibrium, E_i is close to the centre of the bandgap and is equal to the Fermi level.

2.2.2. Extrinsic behaviour

An extrinsic semiconductor is a material in which there is present an active dopant species, whether present inadvertently or added deliberately; as a consequence the electrical behaviour of the material is radically modified.

In a pure material the electron and hole concentrations are equal since a hole in the VB can only be created by the excitation of an electron into the CB, however by introducing an impurity this is no longer the case. Consider an infinite lattice of tetravalent atoms, for example silicon. Each silicon atom uses its four valence electrons to form covalent bonds with four neighbouring atoms. If a pentavalent species, such as arsenic, is substituted into one of the silicon sites (replacing a silicon atom), four of the arsenic valence electrons will be used for bonding, and there is one additional electron that is weakly bound to the arsenic atom. The binding energy of this electron is small compared to $k_B T$ at room temperature, therefore it will be ionised (the energy of ionisation can be calculated approximately using an approximate 'hydrogen like' model) to the CB leaving behind a positively charged arsenic ion; this electron is now available for conduction. The substitutional arsenic atom is known as a *donor*, and a material containing donor species is known as *n-type*. This process can be represented by a donor bound level in the band diagram of the material (E_d), refer to Figure 2.4a. Similarly, if a silicon atom is substituted by a trivalent compound such as boron, then an electron from the VB will be used to form a covalent bond creating a loosely bound hole in the VB. This will be ionised at room temperature and therefore the hole will be available for conduction. This trivalent atom is known as an *acceptor*, and a material containing acceptor species is known as *p-type*. This process creates an acceptor bound level (E_a) in the band diagram of the material, as shown in Figure 2.4b.

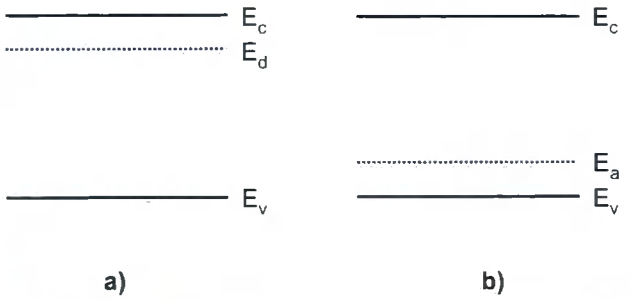

Figure 2.4. a) Donor and b) acceptor bound levels in an extrinsic semiconductor.

The conductivity of a semiconductor material is proportional to the number density and mobility of the free carriers; this is equivalent for both electrons and holes:

$$\sigma = q\mu_n n + q\mu_p p \tag{2.24}$$

or considering resistivity:

$$\rho = \frac{1}{\sigma} = \frac{1}{q\mu_n n + q\mu_p p} \tag{2.25}$$

As the intrinsic carrier density is very small compared to the number of atoms of the material for pure semiconductors ($n_i \approx 1\text{x}10^{10}$ cm^{-3} at 300 K for silicon), by intentionally adding dopants the resistivity can be changed by many orders of magnitude, as shown in Table 2.2.

	Dopant Concentration (cm^{-3})	**Resistivity (Ω cm)**
Silicon	1.6x10^{21}	1x10^{-4}
	4.0x10^{11}	1x10^{4}

Table 2.2. Electrical resistivity of arsenic doped silicon [2].

2.2.3. Self doping and deficit semiconductors

Semiconductors may also contain intrinsic defects which introduce levels into the bandgap and modify the electronic properties, this is termed *self doping*. This effect is particularly common in the case of polycrystalline materials, where a large number of defects present at grain boundaries may cause an otherwise intrinsic material to become *n*-type or *p*-type.

Another effect which may be important in compound semiconductors is the *deficit* effect, this may occur if one constituent of the compound is stoichiometrically more prevalent than another; this imbalance can act as an impurity. This effect is especially important in the principal material investigated in this work, cadmium sulphide, as this semiconductor is typically cadmium rich (sulphur deficient) causing the material to be *n*-type.

2.3. The photovoltaic effect

The PV effect is the direct conversion of light energy into electrical energy. It is the result of two independent processes in a device, firstly the generation of mobile charge carriers by the action of incident photons, and secondly the separation and subsequent extraction of these charge carriers to an external circuit. If a photon of energy $\hbar\omega$ is incident upon a semiconductor with a bandgap value E_g and $\hbar\omega \geq E_g$ then an electron hole pair will be produced, this electron hole pair will eventually recombine releasing energy in the form of heat (phonons) or light (photons), and therefore must be separated before recombination in order to produce useful energy. There are many types of PV device configuration which are capable of separating charge carriers; in the following discussion two important classes will be qualitatively discussed, metal-semiconductor and semiconductor-semiconductor junctions.

2.3.1. Metal-semiconductor junctions

2.3.1.1. Schottky diode

A Schottky diode metal-semiconductor junction is one of the simplest methods of inducing charge separation, and was one of the earliest PV device configurations to be explored [7]. Consider a metal of work function Φ_m and an *n*-type semiconductor of a lower work function Φ_n which are brought into intimate contact (Figure 2.5). Because the semiconductor has a lower work function, there will be a transfer of electrons from the semiconductor to the surface of the metal until the Fermi levels equilibrate, thus creating an electric field in a layer close to the metal-semiconductor interface. This leaves behind a region of positively charged uncompensated donor atoms in the semiconductor; as there are no majority charge carriers (electrons) in this region this is known as the *depletion region*. Any electron hole pairs created in the depletion region or within approximately one diffusion length of this will be influenced by this field, free electrons will be driven to the left, holes will be driven to the right, and the net effect is that electrons will accumulate in the semiconductor and holes will accumulate in the metal. This causes a negative potential to develop in the semiconductor, and the potential difference across the junction will decrease. The electron quasi-Fermi level in the semiconductor will increase, and the result is an induced photovoltage which is equal to the difference in the Fermi levels in the semiconductor and metal. The important point to note is that the junction is able to develop a photovoltage provided that it presents a barrier to majority carriers, in this case electrons.

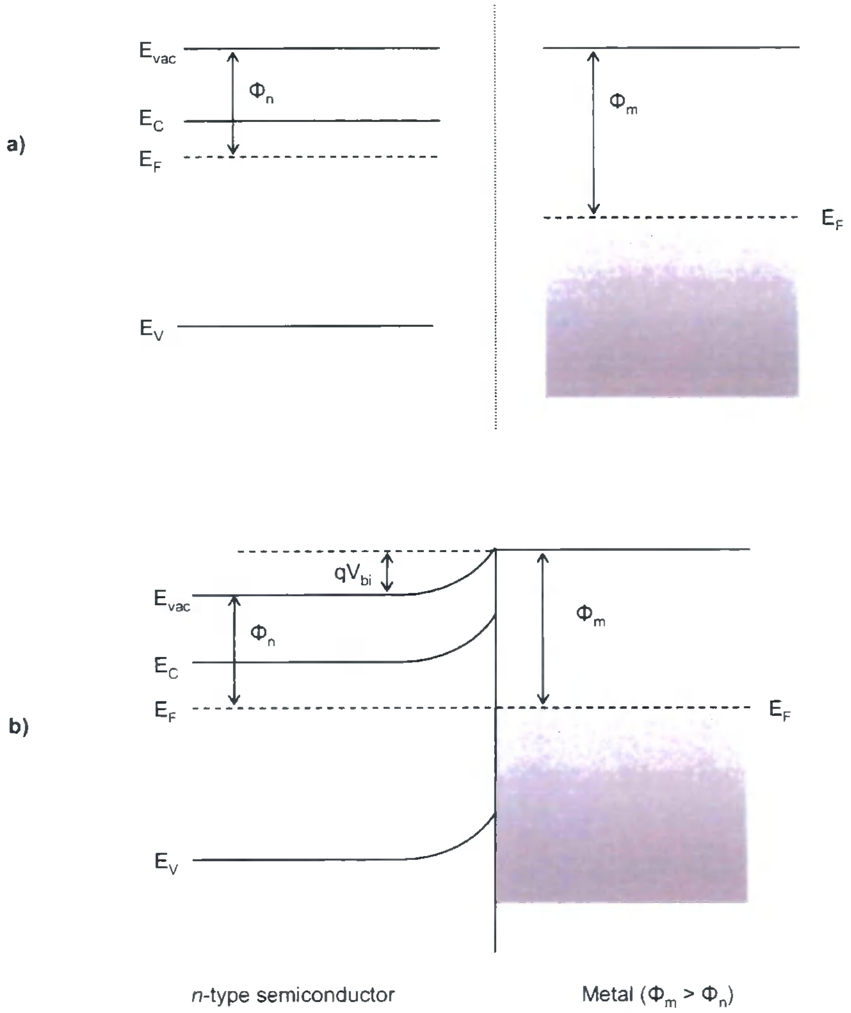

Figure 2.5. Band diagram of an *n*-type semiconductor of work function Φ_n and a metal of work function Φ_m a) before contact. b) after contact.

The presence of band bending in the metal-semiconductor device also governs the current-voltage characteristics of the junction. Charge transport in the *n*-type semiconductor is by electron flow, however the junction will act as a barrier to electrons travelling from the semiconductor to the metal, therefore there can be little current flow in this direction. If the junction is forward biased however the barrier height is decreased and therefore electrons can flow through the junction more easily (the diode equation derivation in section 2.4.2 gives a full treatment for a semiconductor-semiconductor junction). The situation outlined above is completely analogous when considering a *p*-type semiconductor in contact with a metal with a smaller work function ($\Phi_m < \Phi_p$).

2.3.1.2. Ohmic contact

Consider a metal-semiconductor junction where $\Phi_m < \Phi_n$ for an *n*-type semiconductor, or $\Phi_m > \Phi_p$ for a *p*-type semiconductor. The properties of this junction will be very different to that of a Schottky junction as the band bending which occurs will do so in such a way as to encourage the transport of majority carriers across the junction. This has the effect that there can be no charge separation and therefore this junction cannot be used as a PV device. This structure will encourage the injection of majority carriers into the material and will therefore act as an ohmic contact, such a contact is essential for efficient carrier collection from the two metal contacts in a PV device, and the practicalities of this will be discussed in section 3.2.2 and 3.2.5.

2.3.2. Semiconductor-semiconductor junctions

Schottky barrier type photovoltaic devices are limited to low photovoltages, as if the barrier height becomes larger than $E_g/2$ the minority carriers outnumber the majority carriers near the junction, and an inversion layer is formed. A more effective type of PV structure that can sustain higher photovoltages is the semiconductor-semiconductor junction; two types are now briefly discussed, the *p-n* homojunction and the *p-n* heterojunction.

2.3.2.1. *p-n* homojunction

A *p-n* homojunction is formed by doping two regions of the same semiconductor material differently; one side is doped with acceptor species (*p*-type) while the other is doped with donor species (*n*-type). As in the Schottky junction discussed in section 2.3.1.1, there will be a transfer of carriers (in this case electrons from the *n*-type region move to the *p*-type region where they recombine with holes) which results in a depletion region on both sides of the junction. This depletion region provides a barrier to majority carriers, which is a prerequisite for PV action. In a PV device, the minority carriers photogenerated in each side of the depletion region, or within one diffusion length of the depletion region, are driven to opposite sides of the junction (electrons are driven to the *n*-side and holes to the *p*-side) creating a photovoltage. The *p-n* homojunction is widely used in electronic and photovoltaic devices; in section 2.4 a derivation and full explanation is given of the characteristics of this junction.

2.3.2.2. *p-n* heterojunction

A *p-n* heterojunction is similar to the device outlined above, however two different semiconductor materials with different bandgaps form the *p*-type and *n*-type layers. The mechanism of photocurrent generation is the same, however there is an added complication that the difference in bandgap between the two materials cause discontinuities in the conduction and valence bands at the junction interface. The CdS/CdTe device, the main device structure discussed in this work is a *p-n* heterojunction device and will be discussed in detail in chapter 3.

2.4. *p-n* junction physics

The *p-n* homojunction is the most common type of structure used in PV devices, in this section the behaviour of this junction is considered in detail under three situations:

i) At equilibrium
ii) Under the influence of an external bias
iii) Under illumination.

2.4.1. At equilibrium

Consider an *n*-type and a *p*-type semiconductor in intimate contact (Figure 2.6a) where $N_A > N_D$ and it is assumed that the abrupt junction approximation holds, that is the transition from *n*-type to *p*-type material is instantaneous at the junction. For thermal equilibrium to exist there must be a uniform chemical potential throughout this region, this is achieved by a transfer of electrons from the *n*-type material to the *p*-type material which creates a depletion region free of carriers (Figure 2.6b).

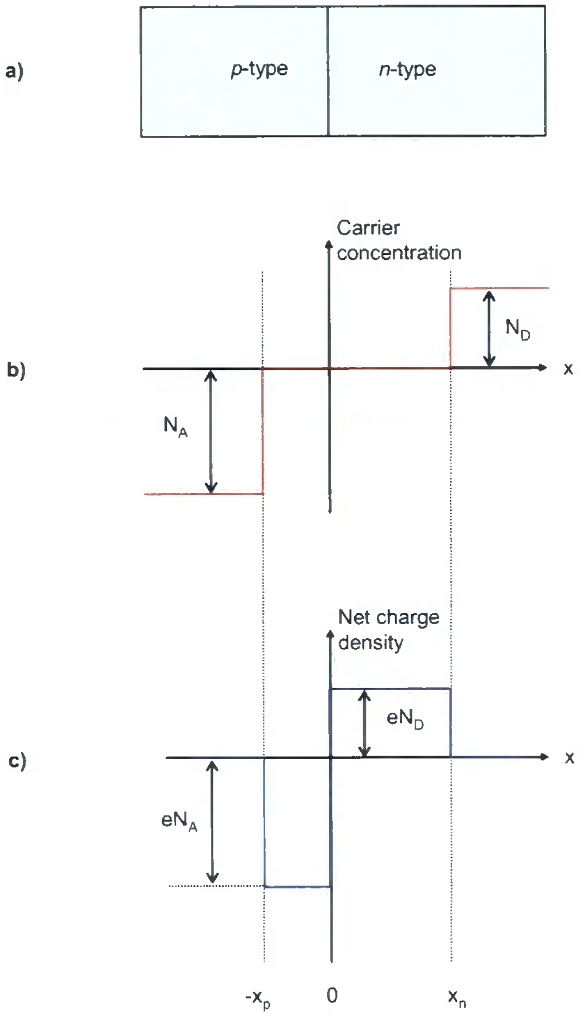

Figure 2.6.a) *n*-type and *p*-type semiconductors in intimate contact, b) Carrier concentration profile c) Net charge density.

On both sides of the junction there are now uncompensated donor and acceptor atoms which create regions of net charge density (Figure 2.6c), here it is assumed that the carrier concentrations have decreased from their bulk values to zero rapidly; thus the charge density is given by:

$$\rho(x) = \begin{cases} -N_A e & -x_p < x < 0 \\ N_D e & 0 < x < x_n \\ 0 & elsewhere \end{cases} \tag{2.26}$$

By using Poisson's equation for the electrostatic potential:

$$\frac{d^2\phi}{dx^2} = -\frac{\rho(x)}{\varepsilon\varepsilon_0} \tag{2.27}$$

and noting that the electric field is related to the potential by:

$$E = -\frac{d\phi}{dx} \tag{2.28}$$

it follows that by taking the integral of 2.27 using the charge densities 2.26 and appropriate boundary conditions, the electric field in the depletion layer is given by:

$$E(x) = \begin{cases} \dfrac{-N_A e}{\varepsilon\varepsilon_0}(x + x_p) & -x_p < x < 0 \\ \\ \dfrac{N_D e}{\varepsilon\varepsilon_0}(x - x_n) & 0 < x < x_n \end{cases} \tag{2.29}$$

This linear relationship is shown in figure 2.7a.

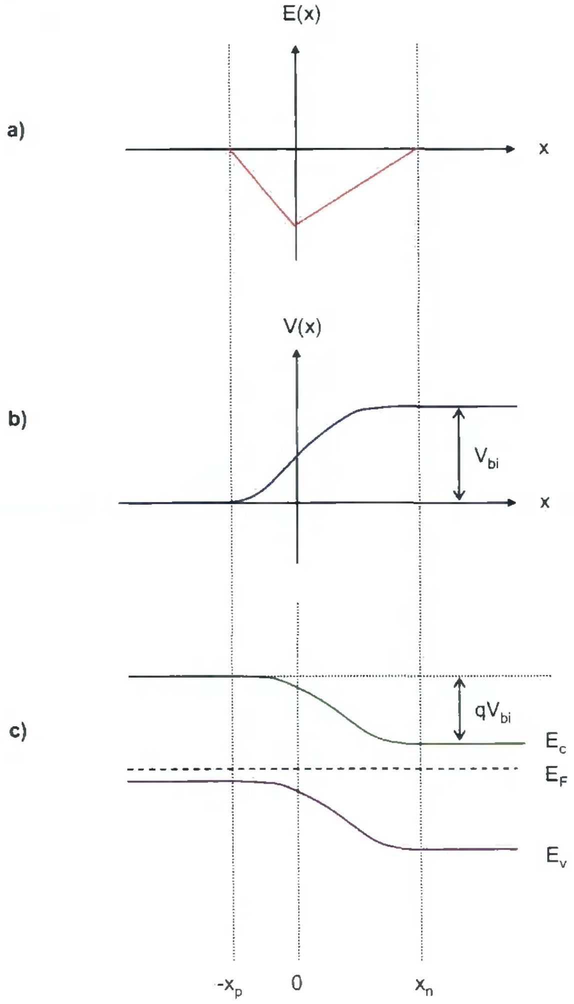

Figure 2.7. a) Electric field b) potential and c) band diagram for a *p-n* abrupt homojunction.

By integrating 2.29, the form of the potential in the junction region (Figure 2.7b) is given by:

$$\phi(x) = \begin{cases} \dfrac{N_A e}{2\varepsilon\varepsilon_0}(x + x_p)^2 & -x_p < x < 0 \\[2ex] V_{bi} - \dfrac{N_D e}{2\varepsilon\varepsilon_0}(x - x_n)^2 & 0 < x < x_n \end{cases} \tag{2.30}$$

This results in the band diagram of Figure 2.7c for this junction

2.4.2. Under external bias

The current-voltage characteristics of an ideal *p-n* homojunction as derived by Shockley [8] is based on four assumptions:

- The abrupt depletion layer approximation holds (refer to section 2.4.1)
- The Boltzmann approximation is valid throughout the depletion layer (refer to section 2.2.1)
- The low injection assumption holds, that is the injected minority carrier densities are small compared with the majority carrier densities
- No generation current exists in the depletion layer (the electron and hole currents are constant throughout the depletion layer).

First consider the Boltzmann relations for electrons and holes at equilibrium (equations 2.17 and 2.18):

$$n = n_i \exp\left(\frac{E_F - E_i}{k_B T}\right) \tag{2.17}$$

$$p = p_i \exp\left(\frac{E_i - E_F}{k_B T}\right) \tag{2.18}$$

And by defining the potentials:

$$\phi \equiv \frac{-E_F}{q} \tag{2.31}$$

$$\psi \equiv \frac{-E_i}{q} \tag{2.32}$$

equations 2.17 and 2.18 become:

$$n = n_i \exp\left(q\frac{(\psi - \phi)}{k_B T} \right) \tag{2.33}$$

$$p = p_i \exp\left(q\frac{(\phi - \psi)}{k_B T} \right) \tag{2.34}$$

At thermal equilibrium it has been shown that the product of the electron and hole densities are constant (equation 2.19), however, when a bias is applied to the junction the minority carrier densities on both sides of the junction are changed and this relation no longer holds. Under bias the carrier densities are defined as:

$$n = n_i \exp\left(q\frac{(\psi - \phi_n)}{k_B T} \right) \tag{2.32}$$

$$p = p_i \exp\left(q\frac{(\phi_p - \psi)}{k_B T} \right) \tag{2.33}$$

where ϕ_n and ϕ_p are the quasi-Fermi levels for electrons and holes respectively:

$$\phi_n \equiv \psi - \left(\frac{k_B T}{q} \right) \ln\left(\frac{n}{n_i} \right) \tag{2.34}$$

$$\phi_p \equiv \psi - \left(\frac{k_B T}{q} \right) \ln\left(\frac{p}{n_i} \right) \tag{2.35}$$

Taking the product of 2.32 and 2.33 gives:

$$pn = n_i^2 \exp\left(q\frac{(\phi_p - \phi_n)}{k_B T} \right) \tag{2.36}$$

It is apparent from this relation that under forward bias, where $(\phi_p - \phi_n) > 0$:

$$pn > n_i^2 \tag{2.37}$$

and under reverse bias, where $(\phi_p - \phi_n) < 0$:

$$pn < n_i^2 \tag{2.38}$$

By using equation 2.32, the current density equation for electrons:

$$\underline{J}_n = q\mu_n n\underline{E} + qD_n \nabla n \tag{2.38}$$

where D_n is the electron diffusion constant given by the Einstein relationship:

$$D_n = \left(\frac{k_B T}{q}\right)\mu_n \tag{2.39}$$

and equation 2.28 in vector form:

$$\underline{E} = -\nabla \psi \tag{2.40}$$

it follows that:

$$\underline{J}_n = q\mu_n \left(n\underline{E} + \frac{k_B T}{q}\nabla n\right) \tag{2.41}$$

$$\underline{J}_n = q\mu_n n(-\nabla \psi) + q\mu_n \frac{k_B T}{q}\left(\frac{qn}{k_B T}(\nabla \psi - \nabla \phi_n)\right) \tag{2.42}$$

$$\underline{J}_n = -q\mu_n n \nabla \phi_n \tag{2.43}$$

Using a similar argument the hole current density is given by:

$$\underline{J}_p = -q\mu_p p \nabla \phi_p \tag{2.44}$$

Thus the electron and hole current densities are proportional to the gradients of the electron and hole quasi-Fermi levels respectively. As the electron density n varies in the junction from the n-side to the p-side by many orders of magnitude while $\underline{J}_n$ remains approximately constant, it follows from equations 2.43 and 2.44 that ϕ_n and ϕ_p must be approximately constant throughout the depletion layer. Therefore, as the electrostatic potential is given by:

$$V = \phi_p - \phi_n \tag{2.45}$$

equations 2.36 and 2.45 combine to give the carrier densities at the boundaries of the depletion layer region:

$$n_p = \frac{n_i^2}{p_p} \exp\left(\frac{qV}{k_B T}\right) = n_{p0} \exp\left(\frac{qV}{k_B T}\right) \qquad \text{at } x = -x_p \tag{2.46}$$

$$p_n = \frac{n_i^2}{n_n} \exp\left(\frac{qV}{k_B T}\right) = p_{n0} \exp\left(\frac{qV}{k_B T}\right) \qquad \text{at } x = x_n \tag{2.47}$$

These are the boundary conditions for the ideal diode equation, by using the continuity equations for the steady state (refer to [9] for an in-depth discussion) under low injection conditions in one dimension it follows that:

$$-U + \mu_n E \frac{\partial n_n}{\partial x} + \mu_n n_n \frac{\partial E}{\partial x} + D_n \frac{\partial^2 n_n}{\partial x^2} = 0 \tag{2.48}$$

$$-U + \mu_p E \frac{\partial p_n}{\partial x} - \mu_p p_n \frac{\partial E}{\partial x} + D_p \frac{\partial^2 p_n}{\partial x^2} = 0 \tag{2.49}$$

where U is the net recombination rate. It is assumed charge neutrality holds, therefore:

$$n_n - n_{n0} \approx p_n - p_{no} \tag{2.50}$$

By multiplying 2.48 by $\mu_p p_n$ and 2.49 by $\mu_n n_n$ and using the Einstein relation (2.39):

$$-\frac{p_n - p_{n0}}{\tau_a} + D_a \frac{\partial^2 p_n}{\partial x^2} - \frac{n_n - p_n}{\left(\frac{n_n}{\mu_p} + \frac{p_n}{\mu_n}\right)} E \frac{\partial p_n}{\partial x} = 0 \tag{2.51}$$

where D_a is the ambipolar diffusion coefficient:

$$D_a = \frac{n_n + p_n}{\left(\frac{n_n}{D_p} + \frac{p_n}{D_n}\right)} \tag{2.52}$$

and τ_a is the ambipolar lifetime:

$$\tau_a = \frac{p_n - p_{n0}}{U} = \frac{n_n - n_{n0}}{U} \tag{2.53}$$

From the low injection assumption it follows that:

$$p_n << n_n \approx n_{n0} \qquad (n\text{-type region}) \tag{2.54}$$

and so equation 2.51 reduces to:

$$-\frac{p_n - p_{n0}}{\tau_p} + D_p \frac{\partial^2 p_n}{\partial x^2} - \mu_p E \frac{\partial p_n}{\partial x} = 0 \tag{2.55}$$

In the neutral region where there is no electric field, equation 2.55 reduces to:

$$\frac{\partial^2 p_n}{\partial x^2} - \frac{p_n - p_{n0}}{D_p \tau_p} = 0 \tag{2.56}$$

The solution to equation 2.56 with the boundary condition 2.47 and $p_n(x=\infty)=p_{n0}$ gives:

$$p_n - p_{no} = p_{n0}\left(\exp\left(\frac{qv}{k_B T}-1\right)\exp\left(-\frac{(x-x_n)}{L_p}\right)\right) \tag{2.57}$$

where the diffusion length L_p is given by:

$$L_p \equiv \sqrt{D_p \tau_p} \tag{2.58}$$

At $x = x_n$ the electron and hole current densities are therefore given by:

$$J_p = -qD_p \left.\frac{\partial p_n}{\partial x}\right|_{x_n} = \frac{qD_p p_{n0}}{L_p}\left(\exp\left(\frac{qV}{k_B T}\right)-1\right) \qquad n\text{-side} \tag{2.59}$$

$$J_n = qD_n \left.\frac{\partial n_p}{\partial x}\right|_{-x_p} = \frac{qD_n n_{p0}}{L_n}\left(\exp\left(\frac{qV}{k_B T}\right)-1\right) \qquad p\text{-side} \tag{2.60}$$

with the total current given by the sum of 2.59 and 2.60:

$$J = J_p + J_n = J_o\left(\exp\left(\frac{qV}{k_B T}\right)-1\right) \tag{2.61}$$

where the saturation current density J_0 is given by:

$$J_0 \equiv \frac{qD_p p_{n0}}{L_p} + \frac{qD_n n_{p0}}{L_n} \tag{2.62}$$

The Shockley equation (2.61) gives the behaviour of an ideal *p-n* junction under bias, as shown in Figure 2.8.

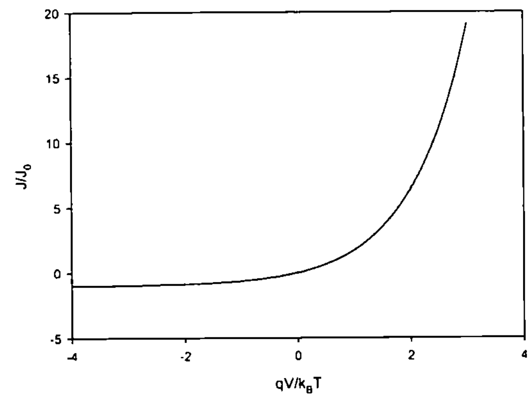

Figure 2.8. JV characteristic for the ideal diode law.

When reverse biased the current saturates at J_0 (in a real device this relationship would eventually break down at a high bias value) and when forward biased the current gain is exponential. This behaviour closely resembles the operation of real *p-n* junctions, including the case of a *p-n* junction based PV device which is not under illumination.

2.4.3. Under illumination

When a *p-n* junction is illuminated, a photocurrent is generated due to the separation of electron hole pairs in the junction region, the magnitude of this photocurrent can be estimated by modelling, however due to the complexity of real devices and materials it is more commonly a measured parameter. The *JV* behaviour of a PV device under illumination can to a first approximation be modelled by superimposing the dark *JV* characteristics (equation 2.61) with a photocurrent assumed to be constant with applied potential:

$$J = J_{dark} - J_{ph} \tag{2.63}$$

$$J = J_0\left(\exp\left(\frac{qV}{k_B T}\right) - 1\right) - J_{ph} \tag{2.64}$$

here the negative sign of J_{ph} is necessary as the two currents have opposing directions.

2.5. Real PV devices

2.5.1. Characterisation parameters

The performance of real PV devices are quantified in practice by analysing the *JV* curve, both in the dark and under illumination, Figure 2.9 shows a simulated *JV* curve for a PV device in the dark and under illumination. There are several commonly used electrical characterisation parameters that can subsequently be used to assess the quality of the device, these are now discussed.

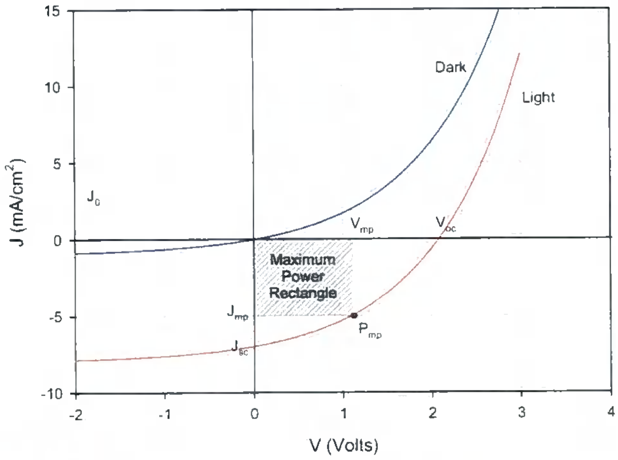

Figure 2.9. Simulated dark and light JV curves, showing common PV device characterisation parameters.

2.5.1.1. Short circuit current density (J_{sc})

The short circuit current density is defined as the current density when no external bias is applied to the device, in an ideal device J_{sc} is equal to the current density generated by irradiance J_{ph}; no power is extracted at this point. The short circuit current I_{sc} is defined as the product of J_{sc} and the area of the device:

$$I_{sc} = AJ_{sc} \tag{2.65}$$

2.5.1.2. Open circuit voltage (V_{oc})

The open circuit voltage is the bias voltage at which the current flowing in the cell is zero; no power is extracted from the device operating at V_{oc}. By rearranging equation 2.64, for an ideal device V_{oc} is proportional to the logarithm of I_{sc}:

$$V_{oc} = \left(\frac{k_B T}{q}\right)\ln\left(1+\frac{J_{ph}}{J_0}\right) \tag{2.66}$$

2.5.1.3. Maximum power point (P_{mp})

The maximum power point is the point on the JV curve where the power output is at a maximum. As the power is equal to the product of the current through the device and the potential difference across it:

$$P_{mp} = I_{mp}V_{mp} \tag{2.67}$$

$$P_{mp} = AJ_{mp}V_{mp} \tag{2.68}$$

The point at which P_{mp} is attained is indicated by the maximum power rectangle in the third quadrant of Figure 2.9.

2.5.1.4. Fill Factor (FF)

The fill factor (FF) is defined as the ratio between the power output of the cell at the maximum power point to the product of the short circuit current and open circuit voltage:

$$FF = \frac{P_{mp}}{I_{sc}V_{oc}} \tag{2.69}$$

It is a measure often expressed in percentage terms, effectively describing the 'squareness' of the JV curve.

2.5.1.5. Efficiency (η)

The efficiency of a PV device is defined as the ratio of the power output of the device at the maximum power point (P_{mp}) to the incident power of light impinging on the surface of the device:

$$\eta = \frac{P_{mp}}{P_{in}} \qquad (2.70)$$

or equivalently:

$$\eta = FF\left(\frac{V_{oc} I_{sc}}{P_{in}}\right) \qquad (2.71)$$

Efficiency is commonly expressed in percentage terms.

2.5.2. Non ideal effects

Real PV devices show deviations from the ideal diode equation (2.61) as they are not ideal diodes and do not contain ideal current sources. Additionally, there are terms which deal with material imperfections and electrical resistances inherent in any practical structure. Therefore, to model the behaviour of a PV device more realistically, several non-ideal effects must be taken into account, in this section these are analysed and the effects on device performance are treated qualitatively. An ideal PV device can be modelled as an equivalent circuit (Figure 2.10) containing a current source representing the photocurrent (J_{ph}) and a diode representing the *p-n* junction:

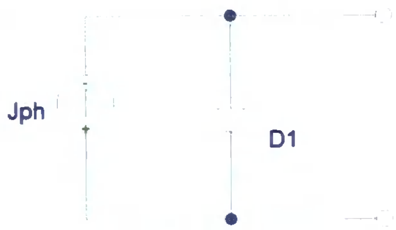

Figure 2.10. Equivalent circuit of an ideal PV device.

The *JV* characteristic curve for this circuit has been simulated using the PSpice [10] modelling package, the results are shown in Figure 2.11 (note that the value of J_{ph} has been arbitrarily chosen).

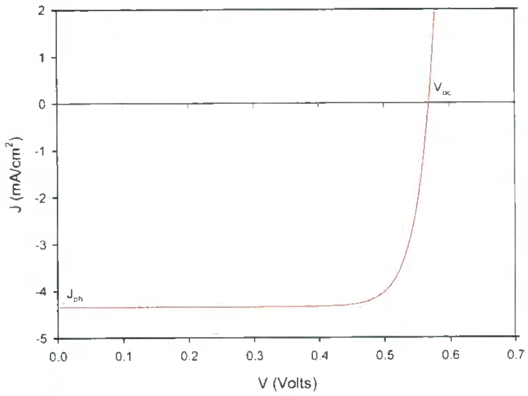

Figure 2.11. Idealised JV curve for a PV device under illumination. $J_o=1\times10^{-8}$ mA/cm^2, $J_{ph}=4.3$ mA/cm^2.

2.5.2.1. Series resistance (R_{series})

PV devices are subject to resistive losses, as the photocurrent generated in the device travels not only through the semiconductor material of the *p-n* junction, but also through the metal contacts to these layers, the current collecting bus and connections to the external circuit. These series resistances can be modelled as components of one consolidated resistance:

$$R_{series} = R_{junction} + R_{contacts} + R_{connections} \tag{2.72}$$

The ideal diode equation can then be modified to take account of this resistance:

$$J = J_0\left(\exp\left(\frac{q(V - AJR_{series})}{k_BT}\right) - 1\right) - J_{ph} \tag{2.73}$$

and the equivalent circuit now becomes:

Figure 2.12. Equivalent circuit containing a series resistance.

Figure 2.13 shows how different values of the series resistance affect the *JV* characteristics of a typical PV device.

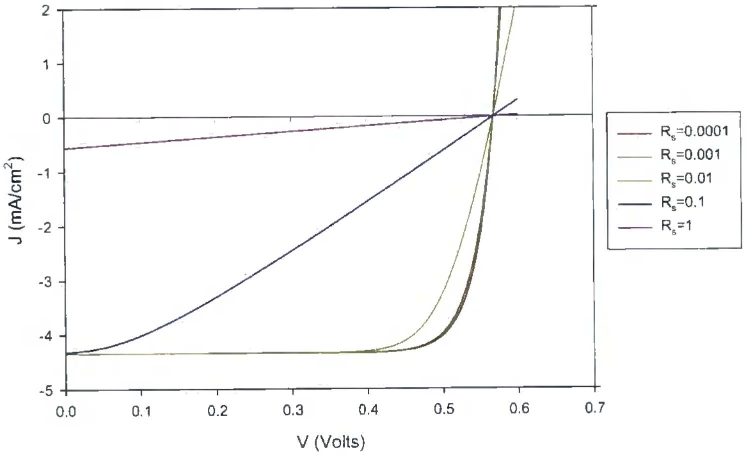

Figure 2.13. JV curves for R$_{series}$ values from 1x10^{-4} Ω to 1 Ω.

The major effect is that as R_{series} increases the *FF* decreases markedly, causing deterioration in the device performance; it is also apparent that at very large values of R_{series} the J_{sc} decreases also. Note that the V_{oc} is relatively unaffected. Ideally in a PV device R_{series} should be as close to zero as possible.

2.5.2.2. Shunt resistance (R_{shunt})

The shunt resistance term deals with physical imperfections in the semiconductor junction layers, these are often short circuit paths through the junction, such as pinholes (refer to section 5.4.1.1), or at the edges of the device. The effects of shunt resistance can be represented by a resistance placed in parallel with the *p-n* junction diode:

Figure 2.14. Equivalent circuit containing a shunt resistance.

and an extra term is added to the diode equation:

$$J = J_0\left(\exp\left(\frac{qV}{k_B T}\right)-1\right)+\left(\frac{V}{AR_{shunt}}\right)-J_{ph} \tag{2.74}$$

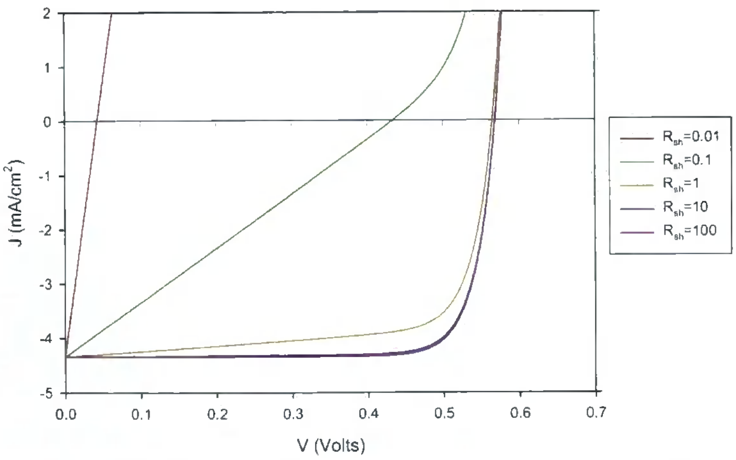

Figure 2.15. JV curves for R_{shunt} values from $1\times10^{-2}\ \Omega$ to $100\ \Omega$.

As shown in Figure 2.15, as R_{shunt} decreases the major effect is upon the *FF* which decreases markedly, at very small R_{shunt} the V_{oc} is also degraded. In a real device ideally R_{shunt} should be as large as possible.

2.5.2.3. Junction recombination

Within the junction region there will inevitably be some recombination of the electron and hole pairs before collection, this can be modelled by inserting an additional diode (the recombination diode) with an ideality factor different to one. The ideality diode factor is generally taken to be between 1 and 2, with a value of 2 being often used.

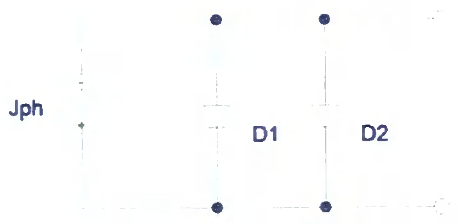

Figure 2.16. Equivalent circuit containing a junction recombination diode.

$$J = J_0\left(\exp\left(\frac{qV}{k_BT}\right)-1\right)+J_{02}\left(\exp\left(\frac{qV}{2k_BT}\right)-1\right)-J_{ph} \qquad (2.75)$$

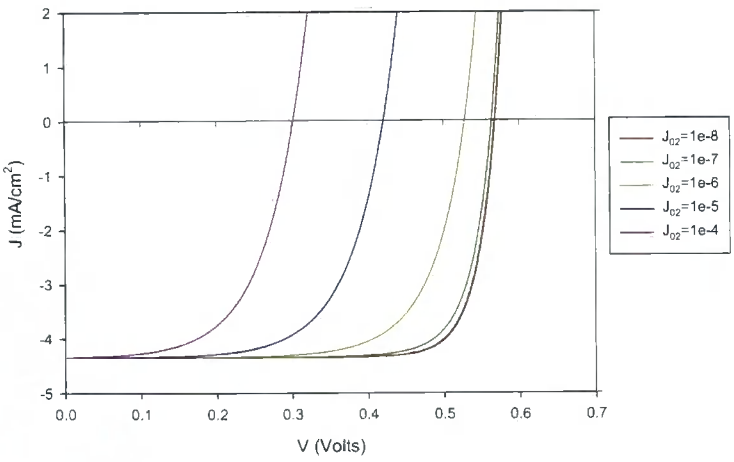

Figure 2.17. JV curves for J_{02} values from 1×10^{-4} mA/cm^2 to 1×10^{-8} mA/cm^2.

As junction recombination becomes more important, the saturation current density term J_{02} increases, this has the effect of decreasing V_{oc} and to a lesser extent the *FF*.

2.5.2.4. Non-ideality of the diffusion diode

Real diodes do not behave in an ideal way, this is accounted for by inserting a non-ideality factor n into the diode equation. The equivalent circuit is similar to that in section 2.5.2, however with a different diode ideality factor. The diode equation becomes:

$$J = J_0\left(\exp\left(\frac{qV}{nk_BT}\right)-1\right)-J_{sc} \tag{2.76}$$

where n is taken to be between 1 and 2; n=1.1 has been empirically found to satisfactorily describe PV device characteristics accurately.

2.5.2.5. Combined result

The total JV characteristic of a real PV device is found by incorporating these four modifications into the ideal model, this gives the equivalent circuit shown below:

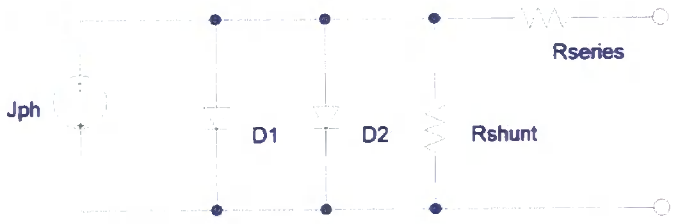

Figure 2.18. Equivalent circuit combining the four previous non-ideal effects.

The equivalent diode equation is given by equation 2.77:

$$J = J_0\left(\exp\left(\frac{q(V-AJR_{series})}{nk_BT}\right)-1\right)+J_{02}\left(\exp\left(\frac{q(V-AJR_{series})}{2k_BT}\right)-1\right)+\left(\frac{V-AJR_{series}}{AR_{shunt}}\right)-J_{ph}$$

By using this model, from a measured JV curve for a PV device, the parameters discussed in section 2.5.1 can be extracted and thus give an indication of the performance of the device. These ideas will be related to real CdS/CdTe photovoltaic cells in chapter 7.

2.6. References

1. WebElements, *Online Elemental Material Data Resource.* (Accessed:02/08/2006). http://www.webelements.com/webelements/elements/text/Au/phys.html

2. Tydex, *Material Data.* (Accessed:02/08/2006). http://www.tydex.ru

3. Boedecker, *Material Information.* (Accessed:02/08/2006). http://www.boedeker.com/feppfa_p.htm

4. Kittel, *Introduction to Solid State Physics.* 2005, London: John Wiley and Sons.

5. Fox, M., *Optical properties of Solids.* 2001, Oxford: Oxford University Press.

6. Madelung, O., ed. *Semiconductors - Basic Data.* 1996, Springer: Berlin.

7. Adams, W.G. and R.E. Day, *The action of light on selenium.* Proceedings of the Royal Society A, 1876. **25**: p. 113–117.

8. Shockley, W., *The Theory of P-N Junctions in Semiconductors and P-N Junction Transistors.* Bell System Technical Journal, 1949. **28**(3): p. 435-489.

9. Sze, S.M., *Physics of Semiconductor Devices.* 1981, London: John Wiley & Sons.

10. PSpice, *Electronic Device Modelling Package*, Cadence: San Jose, California.

3. The CdS/CdTe photovoltaic device

3.1. Introduction

In order to make a practical CdS/CdTe PV device, in addition to the main *p-n* heterojunction there are several additional functional layers and intermediate treatment steps that need to be applied. In this chapter the individual components of a CdS/CdTe device will be introduced and each growth and treatment step fully described. This is followed by a discussion of the health and safety issues regarding the use of cadmium.

3.2. Device components

3.2.1. Substrate

The functions of the substrate are to provide rigidity to the device, both during fabrication and in use, and to protect the sensitive semiconductor layers from moisture and contamination when in their working environment. Two device configurations are commonly employed, the *substrate* and *superstrate* configurations, as shown in Figure 3.1. In the substrate configuration a metal (often a flexible metal foil) is used as the growth platform and the semiconductor layers are sequentially added, with the final layer being a transparent conducting oxide (TCO) material used for front surface current collection. In the superstrate configuration a rigid transparent material, most often glass, is used as a growth platform and the final step is to deposit a metal which is used as current collecting back contact.

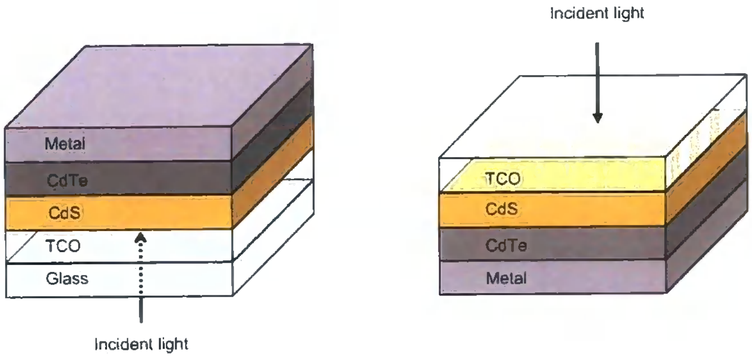

Figure 3.1. a) Superstrate and b) substrate PV device configurations.

Glass is generally used as the transparent material as it is cheap, provides ample transmission in the visible region and can withstand relatively high temperature growth treatments. Soda-lime glass is most often used, however in research devices the more expensive borosilicate glass is sometimes employed as it has better transmission characteristics and contains fewer impurities at reduced concentrations which may diffuse into the semiconducting layers; Emziane et al [1, 2] have showed that this diffusion of impurities from the substrate is of significance in CdS/CdTe devices. In addition, an antireflection coating such as magnesium fluoride (MgF_2) may be applied to the glass surface; this is often used in mass production rather than research-scale devices. In this work the superstrate configuration was used throughout, therefore the following discussion will concentrate on this configuration.

3.2.2. Front contact

The purpose of the front contact is to facilitate current collection from the device whilst allowing as much of the incident light to reach the junction as possible, this is commonly achieved by using a semiconducting TCO material, the properties of this TCO layer have been shown to have substantial effects upon the efficiencies of CdS/CdTe devices [3]. The general properties of a TCO are that i) it should possess a high bandgap (> 3.5 eV) in order allow transmission of a broad wavelength range of light, ii) have a high transmission (> 90%) within this region, iii) should possess a low sheet resistance of the order of 10 Ω/□ and iv) ideally it should also have a crystalline phase and lattice constant similar to that of the material which is to be grown upon it in order to reduce strain and lattice defects. Two common TCO's are generally used, tin oxide doped with indium oxide, known as indium tin oxide (ITO) and fluorine doped tin oxide (FTO). ITO is the more common material in research scale devices as is has a better transmission in the visible region, however as FTO is significantly cheaper to produce (owing to indium being a very expensive metal) it is often used in production PV device modules. Common FTO growth methods are spray pyrolysis and chemical vapour deposition (CVD) of which van Mol gives a comprehensive treatment [4], and ITO is commonly deposited by RF sputtering. Films produced by all these methods are typically polycrystalline.

3.2.3. Cadmium sulphide

In order to maximise PV efficiency, as much incident radiation as possible should reach the *p*-type CdTe absorber layer; therefore it is beneficial for the *n*-type window layer to have as wide a bandgap as possible in order to reduce these absorption losses. CdS possesses a favourably wide bandgap of around 2.42 eV (508 nm) at room temperature [5], however as this absorbs the blue portion of the spectrum, it is advantageous for the CdS layer to be made as thin as possible in order to reduce blue absorption losses. In typical CdS/CdTe devices this layer is around 100 nm thick; it is found that if this layer is made any thinner then incomplete coverage of the substrate tends to produce shunts in the device (refer to section 2.5.2.2). CdS can be grown by numerous techniques including chemical solution deposition, Hodes gives a comprehensive treatment [6], physical vapour deposition (PVD), electrodeposition (ED), metal-organic chemical vapour deposition (MOCVD), sputtering, laser ablation, screen printing, spray pyrolysis and close space sublimation (CSS). The main growth method used in this study, chemical solution deposition (note that the alternate term *chemical bath deposition* (CBD) is often used in the literature), has been shown to produce the most efficient devices to date [7], however it is generally regarded necessary to apply a post-growth annealing treatment in order to improve the crystalline quality of these films; this topic will be treated comprehensively in chapter 6.

3.2.4. Cadmium telluride

A polycrystalline CdTe layer forms the *p*-type absorber layer of the CdS/CdTe device. CdTe possesses two properties which make it close to ideal as an absorber material: firstly the room temperature bandgap is very close to the calculated theoretical maximum figure of 1.5 eV for a single junction absorber under $AM_{1.5}$ radiation.[8], and secondly CdTe possesses a direct bandgap and therefore has a high absorption coefficient, absorbing 99% of all incident radiation of energy greater than the bandgap in a path length of only 1 micron. This allows the absorber layer to be made very thin, decreasing the amount of material needed to make the device. As a comparison, a typical silicon PV device is approximately 200-250 microns thick, compared to 8 microns in a commercial CdS/CdTe device. Note that 8 microns of CdTe is used in order to compensate for material defects in this layer; it is envisaged that when these problems are better understood thinner devices of the order of 1 micron thickness (of the order of the depletion width) will be feasible. CdTe can be grown by many methods including PVD, ED, MOCVD [9], sputtering, laser ablation, screen printing, spray pyrolysis and CSS. It has been found that the CSS method produces devices of consistently high efficiency, and this is the method used in this study.

It has been found experimentally that in order to generate respectable efficiencies from CdS/CdTe devices, it is necessary to perform an annealing treatment. A $CdCl_2$ layer is generally applied to the surface of the CdTe layer and then an anneal is performed; typical device improvements of a factor of five (2% efficiency without treatment to around 10% upon treatment) are commonly found. Although the mechanisms involved are still being investigated it is thought that the improvement is due to three factors, i) the conversion of the material from *n*-type to *p*-type, ii) the intermixing of CdS and CdTe in the junction region reducing recombination centres [10] and iii) an improvement in carrier collection due to CdTe grain boundary passivation.

3.2.5. Back contact

The back contact is a crucial element of any PV device, however this is especially the case in CdS/CdTe. As discussed in section 2.3.1.2, in order to make an ohmic contact to a *p*-type semiconductor the metal must have a larger work function than the semiconductor:

$$\Phi_m > \Phi_p \tag{3.1}$$

or alternatively the height of a Schottky barrier of a metal to the material should be less than or equal to zero:

$$\phi_b = \frac{E_g}{q} + \chi - \phi_m \tag{3.2}$$

$$\phi_b \leq 0 \tag{3.3}$$

where ϕ_b is the barrier height, χ is the electron affinity of CdTe and ϕ_m is the metal work function. For CdTe there is no metal with a work function high enough, and therefore a barrier will be formed by a contact of this type. One way around this is to create a $p+$ layer on the CdTe surface, this has the effect of reducing the work function at the surface, and thus it is then possible to produce a quasi-ohmic contact with a metal. In practice this is done by etching the CdTe layer with an acid that leaves a tellurium rich layer at the surface. Another approach is to apply a copper doped graphite paste to the CdTe layer and then perform an annealing step; the copper ions diffuse into the CdTe layer and again produce a p^+ surface layer. Finally, another method which has been applied to a set of device structures in this study involves depositing antimony telluride (Sb_2Te_3) onto the CdTe layer before applying the metal molybdenum, Sb_2Te_3 is a semiconductor which has a higher work function than CdTe; this contact this has been shown to produce devices with notable efficiencies [11].

3.3. Growth and treatment methods

In the following section, the practical details of all preparation, growth and treatment steps are outlined.

3.3.1. Substrate and front contact

Glass substrates with TCO layers were purchased direct from suppliers; three types were used in this study:

Supplier	Glass Substrate	TCO	Sheet Resistivity (Ω/□)
Merck	Soda-lime (0.75 mm)	ITO (100 nm)	15
VisionTek	Soda-lime (1 mm)	ITO (100 nm)	12
Pilkington	Soda-lime (3 mm)	FTO (500 nm)	8

Table 3.1. TCO substrates used in this study, data are manufacturer's specification.

Additionally, where plain glass slides were used, these were commonly available 1 mm thick soda-lime glass microscope slides. The following standard cleaning procedure was applied to all substrates:

- Rinse and ultrasonic treatment (10 minutes) in 4% Decon 90© soap solution in 18 MΩ deionised water
- Rinse and ultrasonic treatment (10 minutes) in 18 MΩ deionised water
- Ultrasonic treatment (10 minutes) in acetone
- Reflux (minimum of 5 cycles) in isopropyl alcohol (IPA).

These were then stored in individual petri dishes under moderate vacuum (approximately $1\mathrm{x}10^{-2}$ mbar) in a desiccator jar until ready for use.

3.3.2. CdS

3.3.2.1. Growth

In this study CdS was grown using two methods, chemical solution deposition (SD), often referred to in the literature as chemical bath deposition (CBD), and CSS. SD, which is based on the deposition of CdS from an aqueous solution is the main topic of this work and will be discussed fully in chapter 5. CSS is a vacuum based method which works on the principle of the reversible disassociation of the CdS compound at high temperatures:

$$2CdS \leftrightarrow 2Cd + S_2 \qquad (3.4)$$

the two species (Cd and S_2) diffuse across the short source-substrate gap (shown in Figure 3.2) and recombine on the substrate forming near stoichiometric CdS.

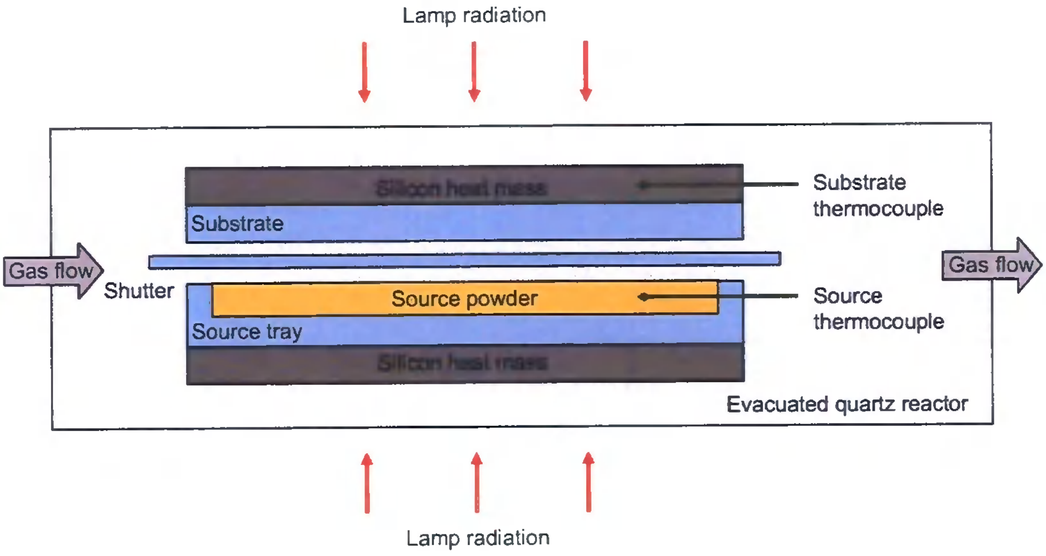

Figure 3.2. Schematic of CSS reactor.

The reactor used in this study was of novel design, with the entire internal assembly made from quartz (with the exception of the thermocouples and the high purity silicon absorber material) in order to minimise the level of impurity incorporation in the growing film. The reactor is enclosed inside a quartz vessel which can be evacuated to

0.1 mbar, and the partial pressures of the ambient gasses hydrogen, nitrogen and oxygen can be accurately controlled by individual mass flow controllers connected to each gas line. The assembly is heated from above and below by two separately controlled lamp sources. The substrate is placed above the powder CdS source (5N purity), the temperature of source and substrate are set and then the quartz shutter is removed. After a controlled period of time (typically of the order of minutes) the heating is switched off and the system is cooled down rapidly by flushing with pure nitrogen gas.

3.3.2.2. Anneal

After growth, a separate annealing treatment is often performed on CdS films; this is carried out by placing the CdS film onto a quartz substrate holder and then inserting it into a preheated quartz furnace tube at the required temperature. The gas ambient can be set to air, nitrogen or a hydrogen forming gas mixture (4% H_2, 96% N_2). After annealing for the required time interval the holder is moved to a cool part of the furnace. Three variables can be controlled in this treatment:

- Ambient gas (air, N_2, forming gas)
- Annealing temperature (~ 100-600 °C)
- Annealing time (~ 5-30 minutes).

Additionally, it is common to add a layer of the fluxing agent $CdCl_2$ to the surface of the film before the anneal is performed, this is done by evaporating the required thickness of $CdCl_2$ onto the film using PVD. In PVD the sample is placed in a vacuum chamber and the pressure is reduced to around 1×10^{-5} mbar with rotary and diffusion pumps. The temperature of the source, in this study 5N purity (99.999%) $CdCl_2$ powder contained within a ceramic crucible, is slowly ramped up to 400 °C, when this temperature is reached the shutter is opened and deposition will start. The $CdCl_2$ film thickness is monitored by a calibrated quartz crystal monitor; after the required thickness is reached the shutter is closed, the source heater is switched off and the apparatus is left to reach room temperature before it is opened to air.

3.3.3. CdTe

3.3.3.1. Growth

In this study CdTe was grown by CSS, the apparatus and technique used was identical to that described in section 3.3.2.1. A 5N purity powder CdTe source was used throughout and several calibration runs were performed in order to ensure the film thickness could be controlled to reliably over the range 4-10 μm.

3.3.3.2. Anneal

The post-deposition anneal of the CdTe layer was performed as follows:

- A 100 nm layer of 5N purity $CdCl_2$ was evaporated on to the CdTe surface
- Annealed at 400°C for 20 minutes in air
- Rinsed in boiling 18 MΩ deionised water
- Dried in nitrogen gas.

After this anneal an etching step was then typically applied.

3.3.3.3. Etch

The etching step was performed as follows:

- Sample is placed in a nitric-phosphoric acid (NP) etch solution (1% nitric acid by volume, 70% phosphoric acid (85% wt) solution by volume, 29% deionised water by volume). The samples are immersed for 10 seconds, measured from the moment when bubbles of gas start to form on the surface
- Rinsed in DI water
- Dried in nitrogen gas
- Immediately put into a vacuum dessicator to stop oxidation of the CdTe/Te surface.

3.3.4. Metallisation

The required metal contacts were applied by PVD. The principle of operation is the same as that described for $CdCl_2$ (section 3.3.2.2), however the metal (gold or indium are used in this study) is placed in an electrically heated molybdenum boat rather than a ceramic crucible, requiring the charge of metal to be replaced after each deposition run. In order to make a back contact for a CdS/CdTe PV device (refer to section 3.2.5) or a Schottky contact for a CdS film, a gold film of approximately 100 nm thickness was applied; to produce an ohmic contact to CdS an indium film of approximately 100 nm thickness was used.

3.4. Health and environmental issues

Elemental Cd and many of its compounds are known carcinogens, therefore the question of health and environmental impact must be addressed if this technology is to be commercialised on a large scale.

Cd metal is a by-product of existing zinc, lead and copper production, the amount produced globally is of the order of 20,000 tonnes [12], around 65% of which is used in NiCd batteries; although it is possible to recycle these after their useful life the vast majority (around 95% [13], corresponding to 12,350 tonnes of Cd) are disposed of in ordinary landfill sites. It is interesting to compare this level of Cd waste to the amount of Cd that would be required to build a 1 GW PV power facility (the equivalent output of a medium sized conventional power station): 10,000,000 one square meter panels (equal to an area of approximately 3.2 km square) with an efficiency of 10% would be required, assuming each module contains approximately 10 g of Cd (equivalent to three AA NiCd batteries), this corresponds to 70 tonnes of Cd, only 0.5% of the amount of Cd that is disposed of in landfill sites each year. It is also important to note that at the end of the life of such a facility, likely to be in the region of 30 years, this Cd would certainly be recycled, and so in effect the net Cd use is close to zero.

Another factor is that fossil fuels contain high Cd levels themselves, which when burnt release significant Cd pollution. It is estimated that for every GWh of electricity generated by a coal fired power station, as well as generating 900 tonnes of CO_2, 7.2 tonnes of SO_2 and 2.7 tonnes of NO_x, 142 g of Cd is released from the coal in the process (2 g in the form of escaped gaseous emissions and 140 g in recovered ash).

Therefore, producing electricity using Cd based PV would actually substantially reduce Cd emissions to the environment. This argument of course does not deal with the energy required to manufacture these modules, the majority of which will be derived from burning fossil fuels, however the estimated energy pay-back time for a CdS/CdTe module is calculated to be under one year [14] and so this is not considered to be a major factor.

Another important consideration is the risk that Cd from PV modules may find its way into the environment. The possibility of release by three scenarios, i) accidental module breakage, ii) leaching by water and iii) exposure to fire has been studied by Steinberger [15]. It was concluded fire was the only scenario for potential exposure; further more in-depth work by Fthenakis [16] concluded the same result by performing fire tests, that during fire the present encapsulation schemes prevent any considerable release of Cd.

The concern regarding cadmium exposure to staff working in the PV manufacturing industry has been studied by Bohland [17]. In this study the levels of Cd present in blood tests carried out at Firstsolar, the largest CdS/CdTe module manufacturer were monitored. No Cd presence above normal background levels were found, concluding that careful manufacturing procedures are adequate to prevent adverse health effects to staff.

3.5. References

1. Emziane, M., K. Durose, D.P. Halliday, N. Romeo, and A. Bosio, *SIMS depth profiling of CdTe-based solar cells grown on sapphire substrates.* Thin Solid Films, EMSR 2005 - Proceedings of Symposium F on Thin Film and Nanostructured Materials for Photovoltaics, 2006. **511-512**: p. 66-70.

2. Emziane, M., K. Durose, N. Romeo, A. Bosio, and D.P. Halliday, *Effect of CdCl2 activation on the impurity distribution in CdTe/CdS solar cell structures.* Thin Solid Films, EMRS 2004, 2005. **480-481**: p. 377-381.

3. Romeo, N., A. Bosio, V. Canevari, M. Terheggen, and L. Vaillant Roca, *Comparison of different conducting oxides as substrates for CdS/CdTe thin film solar cells.* Thin Solid Films, 2003. **431-432**: p. 364-368.

4. van Mol, A.M.B., *Chemical Vapour Deposition of Tin Oxide Thin Films.* 2003, University of Eindhoven: Eindhoven, The Netherlands.

5. Archbold, M.D., D.P. Halliday, K. Durose, T.P.A. Hase, D.S. Boyle, S. Mazzamuto, N. Romeo, and A. Bosio, *Development of low temperature approaches to device quality CdS: A modified geometry for solution growth of thin films and their characterisation.* Thin Solid Films, 2007. **515**(5): p. 2954-2957.

6. Hodes, G., *Chemical Solution Deposition of Semiconductor Films.* 2003, New York: Dekker.

7. Wu, X., J.C. Keane, R.G. Dhere, C. DeHart, D.S. Albin, A. Duda, T.A. Gessert, S. Asher, D.H. Levi, and P. Sheldon. *16.5%-Efficient CdS/CdTe polycrystalline thin-film solar cell.* in *17th European Photovoltaic Solar Energy Conference.* 2001. Munich, Germany.

8. Loferski, J.J., *Theoretical Considerations Governing the Choice of the Optimum Semiconductor for Photovoltaic Solar Energy Conversion.* Journal of Applied Physics, 1956. **27**(7): p. 777-784.

9. Zoppi, G., *Studies of CdTe Thin Films and Solar Cells Grown by MOCVD*, in *Physics*. 2005, University of Durham: Durham, U.K.

10. McCandless, B.E., L.V. Moulton, and R.W. Birkmire, *Recrystallization and sulfur diffusion in CdCl2-treated CdTe/CdS thin films.* Progress In Photovoltaics, 1997. **5**(4): p. 249-260.

11. Romeo, N., A. Bosio, R. Tedeschi, A. Romeo, and V. Canevari, *A highly efficient and stable CdTe/CdS thin film solar cell.* Solar Energy Materials and Solar Cells, 1999. **58**(2): p. 209-218.

12. USGS, *US Geological Survey Cadmium Production Statistics.* (Accessed:02/08/2006). http://minerals.usgs.gov/minerals/pubs/commodity/cadmium/

13. WasteOnline, *Battery Recycling Information.* (Accessed:02/08/2006). http://www.wasteonline.org.uk/resources/InformationSheets/Batteries.htm

14. Fthenakis, V.M. and H.C. Kim, *Energy use and greenhouse gas emissions in: The life cycle of CdTe photovoltaics*, in *Life-Cycle Analysis Tools for Green Materials and Process Selection.* 2006. p. 83-88.

15. Steinberger, H., *Health, safety and environmental risks from the operation of CdTe and CIS thin-film modules.* Progress in Photovoltaics, 1998. **6**(2): p. 99-103.

16. Fthenakis, V.M., M. Fuhrmann, J. Heiser, A. Lanzirotti, J. Fitts, and W. Wang, *Emissions and encapsulation of cadmium in CdTePV modules during fires.* Progress in Photovoltaics, 2005. **13**(8): p. 713-723.

17. Bohland, J.R. and K. Smigielski, *First Solar's CdTe module manufacturing experience; Environmental, health and safety results*, in *Conference Record of the Twenty-Eighth Ieee Photovoltaic Specialists Conference - 2000*. 2000. p. 575-578.

4. Characterisation techniques

4.1. Introduction

In this chapter the characterisation techniques used in this work are described in detail. For each technique it is explained what information is acquired about the material or device, on what physical principles the technique is based and also the practical experimental apparatus used in this study. The techniques have been split into two sections, those which deal with the properties of thin film materials in isolation, and those that are more often used to characterise full PV device structures.

4.2. Characterisation of thin films

4.2.1. Optical methods

Optical methods characterise materials by their interaction with electromagnetic radiation, they are generally non-destructive and do not require sample preparation or contacting. In this work photoluminescence spectroscopy and optical transmission spectroscopy have been used extensively.

4.2.1.1. Photoluminescence spectroscopy

Photoluminescence (PL) spectroscopy is an optical characterisation tool that is commonly used to probe many key material parameters. Some typical properties that can be investigated include:

- Bandgap
- Impurities, type and concentration
- Crystallinity
- Strain
- Surface behaviour, including trapping states

- Homogeneity, through surface mapping.

The technique when applied to semiconductor materials, here we assume a direct bandgap semiconductor as all the materials used in this work fall into this category, relies on the absorption of a photon which has energy greater than or equal to the bandgap of the material (this process is described in detail in section 2.2):

$$E_{photon} = h\upsilon \geq E_g \qquad (4.1)$$

The absorption of the photon will create an electron-hole pair and if the photon energy is greater than the bandgap, the excess energy of each photogenerated carrier:

$$E_{excess} = E_{photon} - E_g \qquad (4.2)$$

will be quickly lost by thermalisation (Figure 4.1) and as a result there will be an electron at the conduction band edge and a hole at the valence band edge.

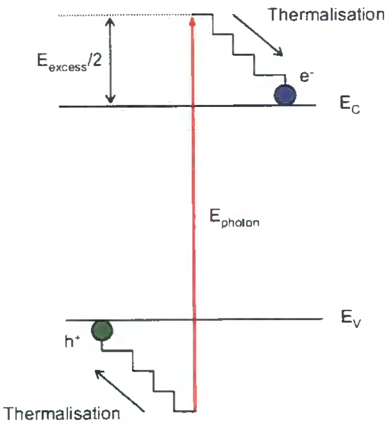

Figure 4.1. Thermalisation of photogenerated carriers.

With relatively pure semiconductors at cryogenic temperatures this generally leads to the formation of an excitonic state (a bound electron and hole system) as the typical electron and hole binding energy will be greater than k_BT and so there will not be any thermal phonons with sufficient energy to destroy this state. This free exciton (or unbound electron-hole pair in the case of relatively impure semiconductors or in a high temperature instance) will subsequently recombine, thus releasing a photon via one of several radiative routes dependent on the material; here only radiative routes are considered:

- CB to VB transition
- Donor/acceptor to VB/CB edge transition
- Donor-acceptor pair transition
- Free exciton recombination
- Donor bound excitons (D^0X, D^+X) or acceptor-bound excitons (A^0X, A^-X), formed when a donor or acceptor state (which can be ionised or neutral) traps an exciton and this subsequently recombines.

Each of these recombination pathways will have an associated characteristic photon energy which can be thought of as a fingerprint for the recombination route, therefore the PL spectrum can be used to identify many of the states responsible for the transitions. Donor and acceptor levels, trapping states and recombination centres can originate from many sources, in CdS, the main object of study in this work, these levels may be present due to the following:

- Extrinsic dopants species, for example indium (donor) or copper (acceptor)
- Lattice vacancies, for example sulphur V_S (donor) or cadmium V_{Cd} (acceptor)
- Lattice interstitials, for example cadmium I_{Cd} (donor) or sulphur I_S (acceptor)
- Surface defects, due to the presence of broken bonds or extrinsic impurities which may occur at the sample surface or concentrated along grain boundaries
- Line defects such as screw and edge dislocations.

The above transitions can also couple with lattice vibrational modes, or *phonons*, to create phonon replicas, this effect is manifested by the appearance of additional peaks, these are positioned at energies equal to an integer number times the characteristic phonon energy $(\hbar\omega_{phonon})$. The most common type of coupling is found to be due to longitudinal optical (LO) phonons, when this effect is strong there can be several peaks present due to one optical transition, with LO phonons they are denoted LO_1, LO_2, LO_3 etc. PL is generally carried out at low temperatures to minimise thermal broadening and also minimise non-radiative transitions, thus sharpening and maximising the signal, however by investigating the temperature dependence of emissions this can also give information on the centres responsible for recombination. The temperature dependence of excitons bound at trap centres to a first approximation are related by:

$$I = \frac{I_0}{1 + A\exp\left(-\frac{E_a}{k_B T}\right)} \tag{4.3}$$

where I_0 would be the intensity of the emission peak at absolute zero, A is a constant and E_a is the activation energy of the trap centre. Therefore by plotting an Arrhenius plot of ln(I) against 1/T the energy of the centre responsible for the transition can be extracted.

Figure 4.2 shows a schematic of the apparatus used in this work. A Coherent Innova 90 argon ion laser was used as the excitation source, this water cooled continuous wave laser has a power consumption of 50 kW and a total output power of 250 mW at the sample. Four main laser lines were available (457.9 nm, 477.2 nm, 488.0 nm and 514.5 nm), however only the 457.9 nm line (a deep violet colour) was used in this study, as this is the only line with an energy great enough to excite PL from CdS and also be significantly far away from the band edge (approximately 512 nm or 2.42 eV), not to interfere with the CdS band edge PL signal. A tuning prism and a further line filter were used to select only this laser line, this beam was then directed and focused using two mirrors and a lens onto the sample. The 70 mm diameter custom made aperture in the cryostat was made of water-free fused silica which has excellent transmission in the 200-2000 nm range. At the sample the beam was incident at approximately 30° to the normal perpendicular to the plane of the sample, and the circular beam diameter was approximately 1 mm, corresponding to a power density of up to 8 W/cm^2.

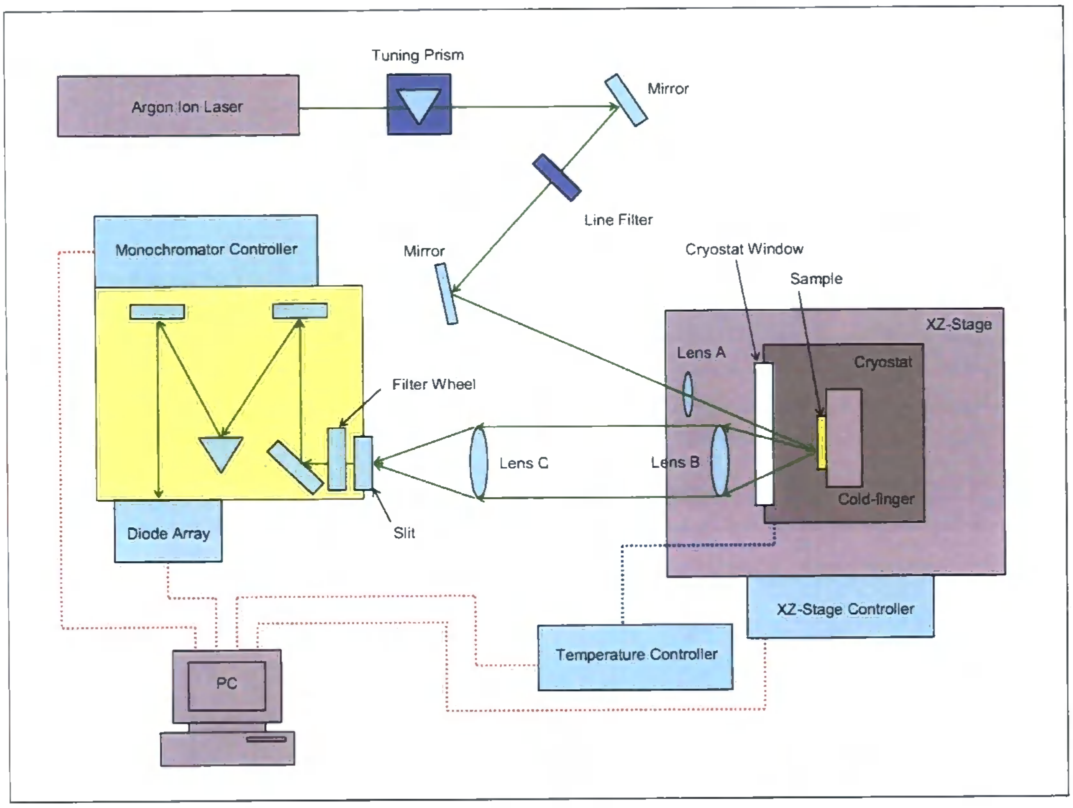

Figure 4.2 PL spectroscopy apparatus.

Samples were held firmly against a copper cold-finger with no need of adhesive by a custom made aluminium sample holder (Figure 4.3); this could hold a maximum of six 7x7 mm samples, and was constructed as it was found that both copper and all the adhesives that were tried in order to attach samples to the cold-finger luminesce strongly themselves in the 600-800 nm wavelength range, therefore obscuring the actual signal from the material being investigated.

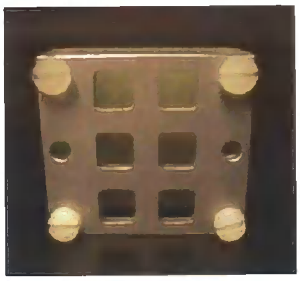

Figure 4.3. Aluminium sample holder.

A Cryomech ST405 closed cycle helium cryostat was used to produce sample temperatures down to 3.2 K, this was controlled by a Scientific Instruments 9650 proportional integral derivative (PID) temperature controller programmed externally from a PC via a general purpose interface bus (GPIB). The cryostat sits on a precision-controlled xz-stage to enable two dimensional surface scans, this was actuated by two independent stepper motors computer controlled via a serial port. Additionally, eight electrical feed-throughs were fitted to the cryostat to enable electrical connections to the samples, however this feature is not used in the work presented here. The PL signal emitted from the sample is collected by a lens (lens B) which forms a parallel beam to a subsequent lens (lens C) which focuses the light onto the slit of a monochromator. The Bentham TM300V monochromator is PC controlled via a serial connection, which encompasses:

- Manually adjustable input slit
- Two diffraction gratings, 150 and 1200 lines/mm giving a spectral range of approximately 550 nm and 60 nm respectively
- Filter wheel comprising interchangeable filters:
    - Order sorting filters, OS400 and OS700
    - Long wavelength pass filters, 457.9 nm and 514.5 nm cut-off
    - Shutter, 0% transmission
    - Empty slot, 100% transmission.

The output of the monochromator is incident upon a 1024 element EG&G PARC 1453A silicon photodiode array; this is peltier cooled with cooling water assistance to -20 °C with a flow of N_2 gas to avoid internal condensation. The data from this photodiode is captured by an EG&G PARC 1471 detector interface via a GPIB computer link. To certify the wavelength accuracy of collected data, it was necessary to fully calibrate the monochromator and photodiode system; two calibrations were performed, one to ensure that the diffraction gratings were showing true wavelength positions, and another to normalise the intensity of the PL peaks. The wavelength position calibration was carried out by using a series of laser lines and spectral lines from halogen lamps (13 lines in total, covering the wavelength range 457.9-1029 nm), each diffraction grating stepper motor was moved over its maximum range to give accurate centre wavelength values as a function of steps. This was then adjusted by the spectral range of the grating at each centre wavelength, and finally this function was fitted by a second order polynomial. The error in this calibration was found to be ±0.7 nm and ±0.3 nm for the 150 and 1200 line gratings respectively, better than the manufacturer's specification. The peak intensity was normalised by taking the manufacturers spectral response data for the diffraction gratings and the diode array, taking the normalised product and then fitting the results with an eighth order polynomial. The measured signal is then simply multiplied by a normalisation factor given by this polynomial to give the true intensity value. These calibrations were built-in to the PL measurement and control software, and therefore all output data is automatically normalised; the raw data was also output to file for consistency. A screenshot of the measurement and control software, created by the author specifically for this task, is shown in Figure 4.3, this was written in Labview 7 and controls all parts of the PL apparatus, it is designed to automate data collection as much as possible as well as to obviate the need for excessive data manipulation.

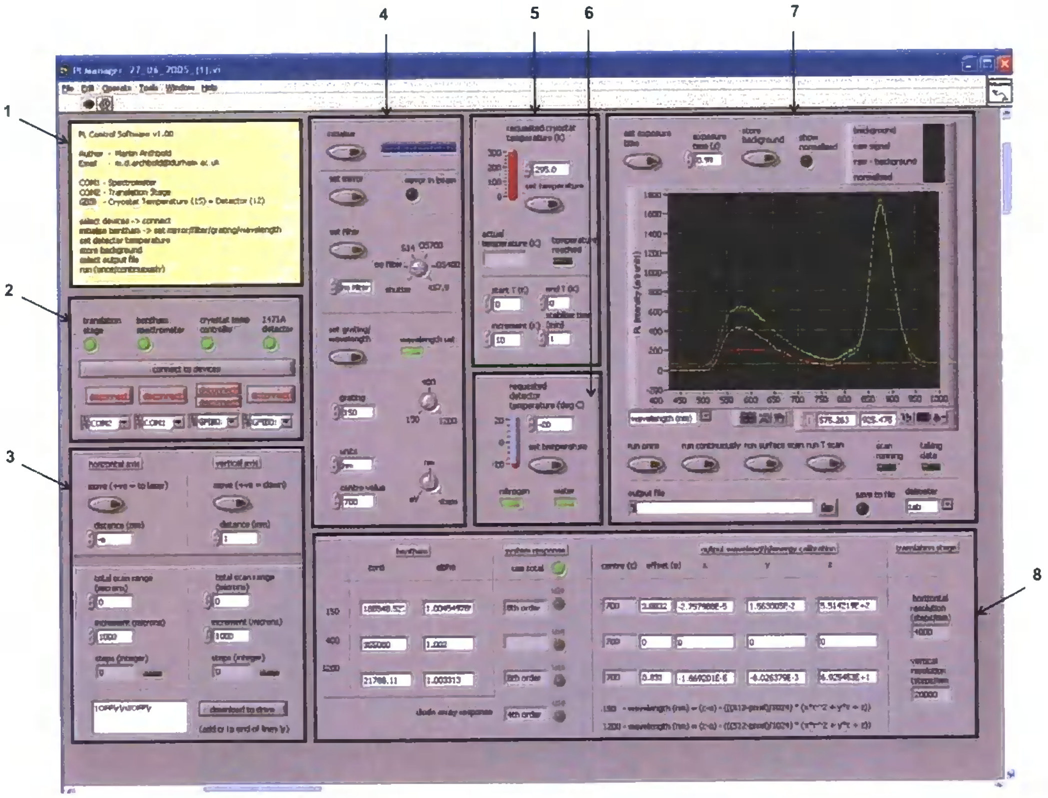

Figure 4.3. PL apparatus control software. Refer to text for description of numbered sections.

There are eight sections of the software controlling various aspects of the apparatus:

1. Software revision version and brief usage instructions
2. Device connection management
3. XZ- stage
    - Manual movement
    - XZ-scan control
4. Monochromator
    - Initialisation
    - Filter wheel
    - Grating selection
    - Grating central wavelength
5. Cryostat temperature controller
    - Manual control
    - Temperature scan
6. Diode array peltier cooler
7. Diode array data acquisition and file output
8. Initialisation conditions, calibration parameters and system response normalisation parameters.

The output of the software is a delimited text file containing the fully normalised PL intensity data with respect to wavelength (and corresponding photon energy). Peaks were fitted using the Peakfit software program using a Gaussian lineshape:

$$G(x;x_0,\sigma)=\frac{1}{\sigma\sqrt{2\pi}}\exp\left(-\frac{(x-x_0)^2}{2\sigma^2}\right) \qquad (4.4)$$

where, x_0 is the mean, σ is the standard deviation, with the full width half maximum (FWHM) equal to $2\sigma\sqrt{2\ln(2)}$.

4.2.1.2. Optical transmission spectroscopy

In optical transmission spectroscopy an incident light beam is scanned over a wavelength range, and the portion of the beam which is transmitted through the material is measured. This gives some important properties of the material, including:

- Bandgap, and whether it is direct or indirect
- Crystallinity
- Film thickness
- General level of transmission, indicative of scattering.

As shown in Figure 4.4, an incident beam may interact in four ways when incident at a solid material, it may be reflected (R), transmitted (T), scattered (S) or absorbed (A).

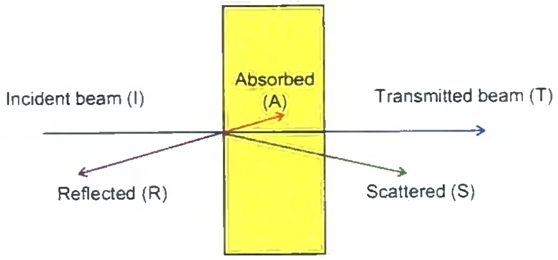

Figure 4.4 A light beam incident at a sample may be i) reflected (R), ii) transmitted (T) iii) scattered (S) or iv) absorbed (A).

If the intensity of the light from these processes is integrated over a sphere surrounding the sample, the total intensity of the incident beam can be given in the following way:

$$I_{incident} = I_R + I_S + I_T + I_A \tag{4.5}$$

where I_R, I_S, I_T and I_A are the reflected, scattered, transmitted and absorbed intensities respectively (note that the absorbed beam will not be detected). In the apparatus used in this study, the detector lies directly behind the sample and there is no spherical integration, therefore only the transmitted beam intensity (I_T) is measured:

$$I_{measured} = I_T \tag{4.6}$$

$$I_{measured} = I_{incident} - \left(I_R + I_S + I_A\right) \tag{4.7}$$

where $I_{measured}$ is the intensity measured at the detector. As there is no facility to integrate over a sphere, it is not possible to give absolute values for the reflected or scattered beams, and therefore the assumption is made that both I_R and I_S are zero and that any loss in the incident beam is due to absorption:

$$I_{measured} = I_{incident} - I_A \tag{4.8}$$

This assumption is satisfactory as long as both I_R and I_S are wavelength independent, if this is the case then only the magnitude of $I_{measured}$ will be lowered by scattering or reflection, whilst it is the change of $I_{measured}$ with wavelength that is the most important parameter in this experiment. The absorption coefficient of the material is then given by:

$$\alpha = \frac{1}{d}\ln\left(\frac{I_{incident}}{I_{measured}}\right) \tag{4.9}$$

where d is the thickness of the film. As discussed in section 2.2 the absorption coefficient in a direct bandgap semiconductor is given by:

$$\alpha = 0 \qquad \text{for } h\upsilon < E_g \tag{4.10}$$

$$\alpha \propto \left(h\upsilon - E_g\right)^{1/2} \qquad \text{for } h\upsilon \geq E_g \tag{4.11}$$

Therefore by plotting α^2 versus $h\upsilon$, the resultant graph should be a straight line which intersects the $h\upsilon$ axis at $h\upsilon = E_g$, thus giving a measure for the bandgap. In addition, the gradient of this intersecting line is a measure of the number density of trapping states which exist near to the CB and VB edges, giving a qualitative measure of crystalline quality. In many films it is also possible to measure the thickness from the presence of interference spectra, however in this study the very thin nature of our CdS films did not allow the use of this technique. The instrument used in this study was a Perkin Elmer Lambda 19 UV-VIS spectrophotometer; the scanning wavelength range was typically between 300-1100 nm, scanning at 30 data points/minute with 1 data point/nm. The instrument utilised a dual beam arrangement (refer to Figure 4.5), and so by using a complimentary substrate reference sample, there is automatic compensation for losses due to the substrate.

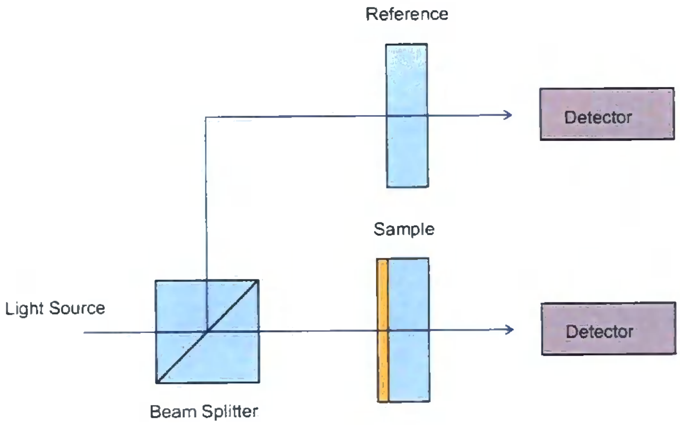

Figure 4.5. Dual beam optical transmission principle.

Resulting α^2 versus $h\upsilon$ data were linearly fitted using Microsoft Excel software, and the absorption coefficient α was compared to data in the literature for consistency.

4.2.2. Structural and chemical methods

4.2.2.1. Film thickness measurement

Film thickness measurements were taken by etching a portion of the film from the substrate with a concentrated acid (hydrochloric acid in the case of CdS), and then using a scanning profilometer to determine the step height. The principle of operation is shown in Figure 4.6.

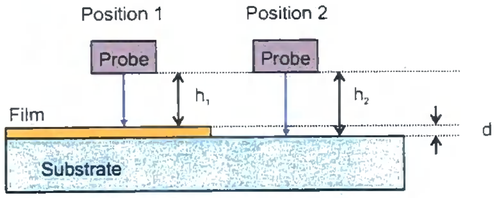

Figure 4.6. Film thickness profilometer.

A mechanical probe is scanned over the surface, from a position on the film (1) to a position on the substrate (2), the height of the probe relative to the detector is measured, and the step height, and therefore the film thickness, is simply the discrepancy between these heights:

$$d = h_2 - h_1 \tag{4.12}$$

The model of profiler used in this study was a Tencor Instruments Alpha-step 200, typically four measurements were taken and subsequently averaged to give an accuracy of the order of 5 nm.

4.2.2.2. X-ray diffraction

X-ray diffraction is an important technique used to investigate the atomic structure of crystalline materials, it is effective in identifying:

- Composition of the material (atom or compound type)
- Crystal phase
- Preferred orientation
- Lattice parameter, indicative of strain
- Grain size (in polycrystalline material).

The technique relies on the diffraction of radiation from the atoms in a crystal lattice; for this to occur the wavelength of the radiation must be of the order of the atomic spacing, this is satisfied by x-rays. Figure 4.7 shows a monochromatic beam of x-rays of wavelength λ incident at a crystal surface at an angle θ, this beam is reflected by a specific hkl crystal plane with a lattice spacing d_{hkl}.

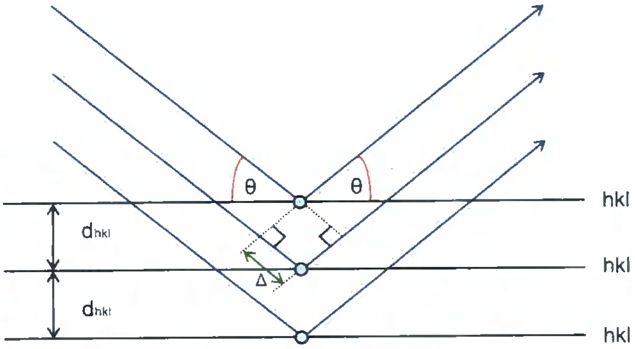

Figure 4.7. Diffraction from the planes of a crystal lattice.

For constructive interference to occur, the path difference Δ must be an integer multiple of half wavelengths of the incoming beam:

$$\Delta = \frac{n\lambda}{2} \tag{4.13}$$

where n is the order of reflection. By geometry this path length is given by:

$$\Delta = d_{hkl} \sin\theta \tag{4.14}$$

and so it follows the constructive interference condition (*Bragg condition*) is satisfied when the lattice spacing d_{hkl} is given by:

$$d_{hkl} = \frac{n\lambda}{2\sin\theta} \tag{4.15}$$

Thus for a crystal plane with the lattice spacing d_{hkl} (considering first order reflections only, $n=1$) there is an angle θ at which this Bragg condition is satisfied, and a strong reflection will occur from this plane:

$$\theta = \sin^{-1}\left(\frac{\lambda}{2d_{hkl}}\right) \qquad (4.16)$$

All crystalline materials possess a crystal structure with characteristic d_{hkl} spacings for each crystal plane, and therefore have unique characteristic diffraction spectra, with strong peaks at specific θ values. By comparing a measured spectrum with values in the literature this can be used to characterise the atomic structure of the material. If we consider the compound CdS, it can exist in two distinct phases, the face centre cubic (fcc) zincblende structure and the hexagonal close packed (hcp) greenockite structure as shown in Figure 4.8 [1].

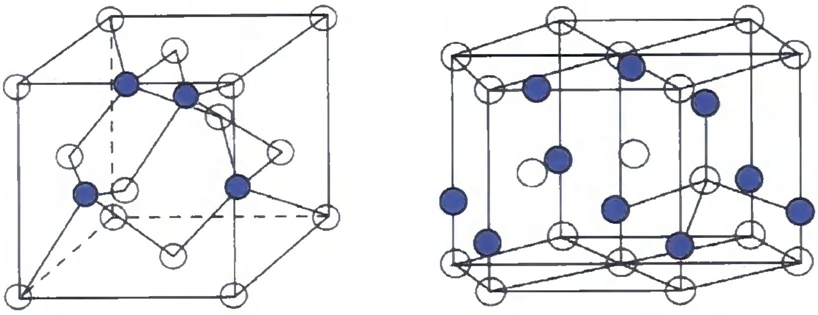

Figure 4.8. Face centre cubic and hexagonal close packed crystal structures, blue and white spheres represent cadmium and sulphur atoms respectively.

The respective d_{hkl} spacings are given by:

$$d_{hkl} = \frac{a}{\sqrt{h^2 + k^2 + l^2}} \qquad \text{(cubic)} \qquad (4.17)$$

$$d_{hkl} = \frac{a}{\sqrt{\frac{4}{3}(h^2 + hk + k^2) + \frac{l^2}{\left(c/a\right)^2}}} \qquad \text{(hexagonal)} \qquad (4.18)$$

where a and c are lattice constants. Tables 4.1 and 4.2 show the d-spacings for each crystal plane and the expected peak position assuming an X-ray wavelength of 1.5418 Å (the mean of the two commonly used Cu K_α lines) and lattice constants a_{cubic} =

5.810 Å, a_{hex} = 4.136 Å and c_{hex} = 6.714 Å [2]. Note that planes with a zero structure factor (for a fcc structure *h*, *k* and *l* are a mixture of even and odd integers and for a hexagonal structure *l* is odd and *h*+2*k* is 3 times an integer) have been omitted, the relative intensities, obtained from the structure factor, are also included as percentages of the highest intensity peak.

h	k	l	d-spacing (Å)	Peak Position (°)	Relative Intensity (%)
1	1	1	3.354	26.573	100
2	0	0	2.905	30.779	40
2	2	0	2.045	44.086	80
3	1	1	1.752	52.218	60
2	2	2	1.677	54.729	10
4	0	0	1.453	64.113	20
3	3	1	1.333	70.673	30
4	2	0	1.299	72.797	10
4	2	2	1.186	81.089	30
5	1	1	1.118	87.176	30
3	3	3	1.118	87.176	30

Table 4.1. Expected *d*-spacings, peak position and relative intensity values for crystal planes in a cubic structure.

h	k	L	d-spacing (Å)	Peak Position (°)	Relative Intensity (%)
1	0	0	3.582	24.858	62
0	0	2	3.357	26.552	91
1	0	1	3.160	28.238	100
1	0	2	2.449	36.690	29
1	1	0	2.068	43.775	48
1	0	3	1.898	47.930	50
2	0	0	1.791	50.993	8
1	1	2	1.761	51.933	31
2	0	1	1.730	52.911	15
0	0	4	1.679	54.683	5
2	0	2	1.580	58.403	3
1	0	4	1.520	60.957	3
2	0	3	1.398	66.915	15
2	1	0	1.354	69.442	5
2	1	1	1.327	71.028	8
1	1	4	1.303	72.532	4
1	0	5	1.257	75.632	9
2	0	4	1.225	78.023	2
3	0	0	1.194	80.434	9
2	1	3	1.158	83.445	14

Table 4.2. Expected *d*-spacings, peak position and relative intensity values for crystal planes in a hexagonal structure.

After obtaining an x-ray diffraction spectra for our material, in order to extract data a fit is made to each identifiable peak using a pseudo-Voigt line shape, along with an exponentially decaying background peak to eliminate the amorphous signal from our glass substrate. The pseudo-Voigt peak shape which fits our experimental data well, takes the form:

$$PV(x;x_0,\sigma,\gamma) = aG(x;x_0,\sigma) + (1-a)L(x;x_0,\gamma) \tag{4.19}$$

This is a linear combination (a is a constant) of a Gaussian $G(x;x_0,\sigma)$ and a Lorentzian $L(x;x_0,\gamma)$ (also known as a Cauchy-Lorentz) function:

$$G(x;x_0,\sigma) = \frac{1}{\sigma\sqrt{2\pi}}\exp\left(-\frac{(x-x_0)^2}{2\sigma^2}\right) \tag{4.20}$$

$$L(x;x_0,\gamma) = \frac{\gamma}{2\pi\left((x-x_0)^2 + \left(\frac{\gamma}{2}\right)^2\right)} \tag{4.21}$$

where x_0 is the mean, σ is the standard deviation of the Gaussian (with the FWHM $=2\sigma\sqrt{2\ln(2)}$ as stated in equation 4.4).and γ is the FWHM of the Lorentzian. By performing this fit using the PeakFit software program we can extract the following data for each peak:

- 2θ position, and standard error
- Amplitude
- FWHM peak width.

The procedure for analysing the material is then as follows:

- Any peaks due to the substrate (for example InO_2 or SnO_2 peaks) are removed from the analysis
- By comparing the measured 2θ positions of the remaining peaks and the data in Tables 4.1 and 4.2 the crystal phase of the material is identified
- The lattice parameter is calculated (assuming either cubic or hexagonal phase) by computing the error between the observed and expected peak positions, and then minimising the sum of these errors by solving for the lattice parameter in the appropriate d_{hkl} equation (equation 4.17 or 4.18).

- If the material is polycrystalline then the grain size can be calculated using the FWHM peak widths. Peak broadening is described by the Scherrer formula:

$$D = \frac{\kappa\lambda}{\Delta(2\theta)\cos\theta} \tag{4.22}$$

where D is the grain size, κ is the Scherrer constant which deals with geometric factors and is usually taken to be equal to unity, λ is the x-ray wavelength, and $\Delta(2\theta)$ is the width of the diffraction peak (in radians). It is important to note that additional broadening of diffraction peaks is caused by strain within a material, this is often resolved by plotting a Williamson-Hall plot [3], however in this work on CdS there are insufficient diffraction peaks to use this method. It is also important to note that the instrument itself will cause peak broadening, however the magnitude of this term is considerably smaller than the other factors mentioned, and therefore this is not considered in the analysis.

- By comparing the measured peak intensities with the intensities in table 4.1 or 4.2 (cubic or hexagonal phase must first be assumed), the preferential orientation or texture of the CdS can be determined.

It is important to note however that to fully determine the texture of a sample it is necessary to perform x-ray diffraction in more than one geometry. Due to the thin nature of typical CdS films used in this study (< 100 nm) it was not possible to perform conventional Bragg-Brentano XRD, and only grazing incidence x-ray diffraction (GIXRD) was carried out. This is because when performing conventional XRD on structures which are extremely thin two problems are present: firstly, the signal strength of the refracted x-ray beam is generally very small as the path length of the beam is short in the thin film, and secondly the signal from the substrate will tend to dominate; these problems can be overcome by utilising the GIXRD geometry. In this modification the x-ray beam is incident at a shallow angle of incidence (Figure 4.9), this creates a significantly longer path length in the material which is essential for maximising signal intensity, and also the x-ray beam does not penetrate as far into the substrate due to total internal reflection within the film, and therefore the signal from the substrate is greatly reduced.

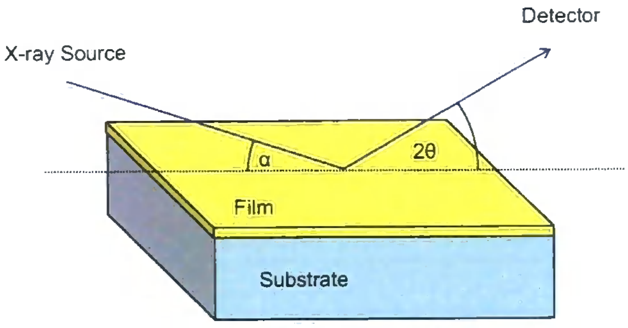

Figure 4.9. Grazing incidence x-ray diffraction geometry, note that the size of angle α is exaggerated and is typically less than 1°.

In practise the incident beam is set to a constant angle α of the order of 0.1 - 1°, and the x-ray detector is scanned from $2\theta = 0°$ to 90° in the plane perpendicular to the film and containing the incident beam. A Bede D1 diffractometer was used in this work, the Cu K_α x-ray line was used, at an angle of incidence of 0.5°. Although the Cu K_α line has two components (1.540562 Å and 1.544390 Å with an intensity ratio of 2:1) this only becomes important at long 2θ values where the separation of the two peaks become evident. As the main CdS peaks appear at small 2θ values, in this work data were fitted with a single pseudo-Voigt lineshape, and the weighted average wavelength (1.541838 Å) of these two lines was used.

4.2.2.3. Scanning electron microscopy

The scanning electron microscope (SEM) is an instrument used to probe the morphology of surfaces in high resolution, the technique enables good depth of field and can typically magnify up to 300,000 times. A tightly focussed beam of electrons, with a beam width on the order of nm, is raster scanned over the sample surface; these are inelastically scattered by atoms in the sample producing interactions which lead to the emission of primary and secondary electrons and radiation (characteristic X-rays and luminescence). In this study the instrument used was a Philips XL FEG in secondary electron imaging mode. It is not necessary to apply a conductive coating in order to stop build-up of charge on the sample surface as the substrates used in most cases were conductive.

4.2.2.4. Atomic force microscopy

The atomic force microscope (AFM) is a high resolution scanning probe microscope used to image the surface of materials. Because a three dimensional profile can be formed, surface topography can be quantitatively assigned parameters, for example height, roughness and particle size. Figure 4.10 shows a schematic of the operation of the microscope. A finely engineered semiconductor tip attached to a flexible cantilever is placed in close proximity to the surface of the material being observed. Due to forces between the tip and the surface (these depend on the mode of the instrument being used, the type of sample and on the proximity of the tip to the surface) the cantilever is deflected and the magnitude of this deflection is measured using a laser beam reflected off the cantilever.

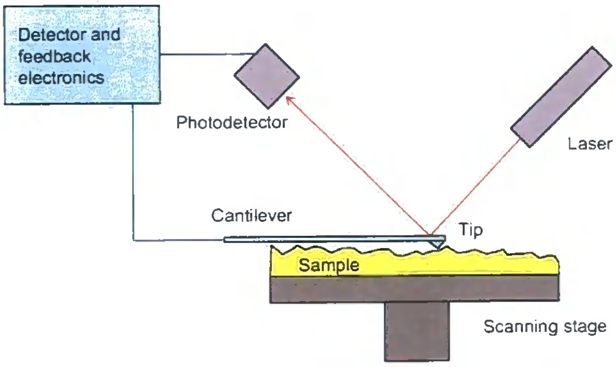

Figure 4.10. AFM principle of operation.

The instrument used in this study was a Digital Instruments Nanoscope IV multimode microscope using commercially available Pelco Tap300 silicon tips with a radius of less than 10 nm.

4.2.2.5. Inductively coupled plasma mass spectrometry

Inductively coupled plasma mass spectrometry (ICP-MS) enables sensitive trace element chemical analysis to part per trillion levels. Samples are decomposed into their elements in a high temperature argon plasma and then subsequently analysed based on their mass to charge ratios. The process involves the following steps:

- Liquid to be analysed is fed into the apparatus using a capillary tube
- It is then passed into a stream of argon gas where it is made into a fine mist
- Mist passes into a radio frequency coupling coil where the elements are separated from their constituent molecules and ionised
- Plasma then passes through a small aperture, into a high vacuum system where it travels through a quadrupole magnet which selects the desired mass to charge ratio
- Signal is detected by an electron multiplier
- Quadrupole can be scanned in order to produce a complete mass spectrum.

In this study both the liquid chemicals that are used in the production of thin film PV devices and also in the solid semiconductor layers themselves are of interest. To analyse solid semiconductor layers they must first be dissolved in a suitable medium. In this study CdS samples were dissolved in a high purity trace metal free 3% hydrochloric acid solution, and then diluted down with DI water to an appropriate concentration in order to be analysed. It is important to note that when using the ICP-MS technique, that each element in the periodic table has a detection limit which is a lower bound to the concentration (normally expressed in parts per trillion (ppt) or parts per billion (ppb)) that can be detected; Figure 4.11 shows these detection limits for the instrument used in this study; the elements indicated in white are not detectable at all, sulphur is detectable at concentrations of > 1 ppb and the elements in dark purple (B, Si, P, Br and I) are detectable at > 0.1 ppb.

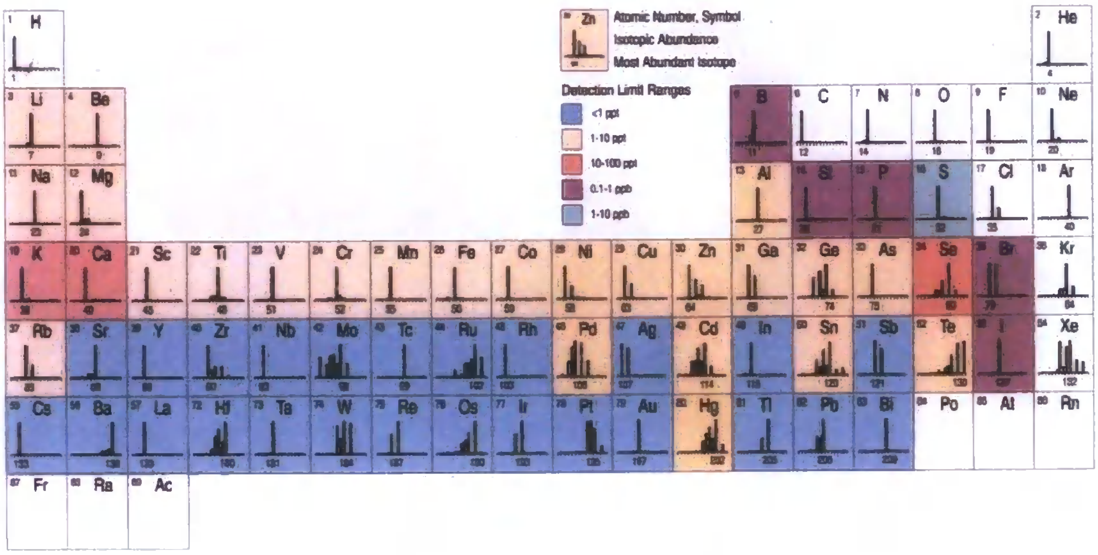

Figure 4.11. Periodic table showing detectable elements and their detection limits [4].

The instrument used in this study was a Perkin Elmer Elan 6000, appropriate calibration runs were performed to ensure that results were consistent.

4.2.3. Electrical methods

Several types of electrical characterisation methods were used in this study, these determine many material characteristics such as sheet and bulk resistivity values, carrier mobilities, donor or acceptor activation levels, photoconductive response and quantum efficiency of electron-hole pair production.

First the necessary electrical contacts are discussed, followed by a detailed description of each of the electrical characterisation methods.

4.2.3.1. Electrical contacts

In order to carry out electrical measurements on semiconductors they must first be contacted in a reproducible way, this is usually performed by evaporating a thin layer of metal onto the clean surface (refer to section 3.3.4). As discussed in 2.3.1 the effect of this will be to form an ohmic or a Schottky contact dependent on the material and the contact used. In this work two geometries of electrical contacts were applied, the *sandwich* contact (Figure 4.12a) in which the semiconductor is grown on a conducting oxide and a metal contact is made on top (here the conduction is perpendicular to the plane of the film), and the *planar* geometry (Figure 4.12b) in which two contacts are made onto a film grown on a non-conductive substrate (here the conduction is parallel to the plane of the film).

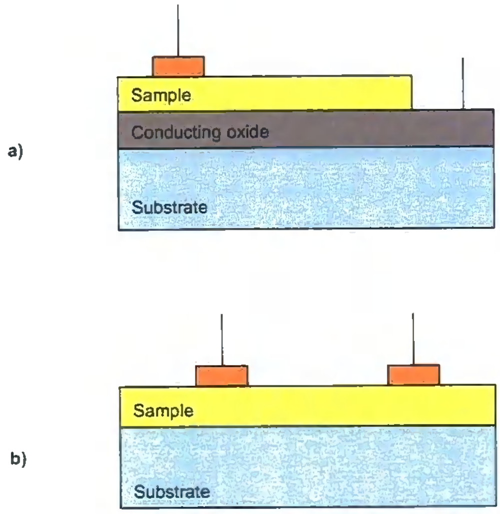

Figure 4.12. a) Sandwich and b) planar electrical contact geometries.

4.2.3.2. Current-voltage measurement

In order to measure the current-voltage characteristics, physical contact is made to each of the evaporated metal contacts by means of a mechanical spring-loaded gold-tipped probe. A GPIB controlled Keithley 2400 source meter is then used to sweep the potential (generally from -1 to 1 V with approximately 50 points/V) and then the corresponding current is measure. A purpose-built data acquisition software package was written in Labview 7 to automate the process; once the sample was in position the sweep was set running and at the end of the sweep the data is output as a tab or space delimited text file.

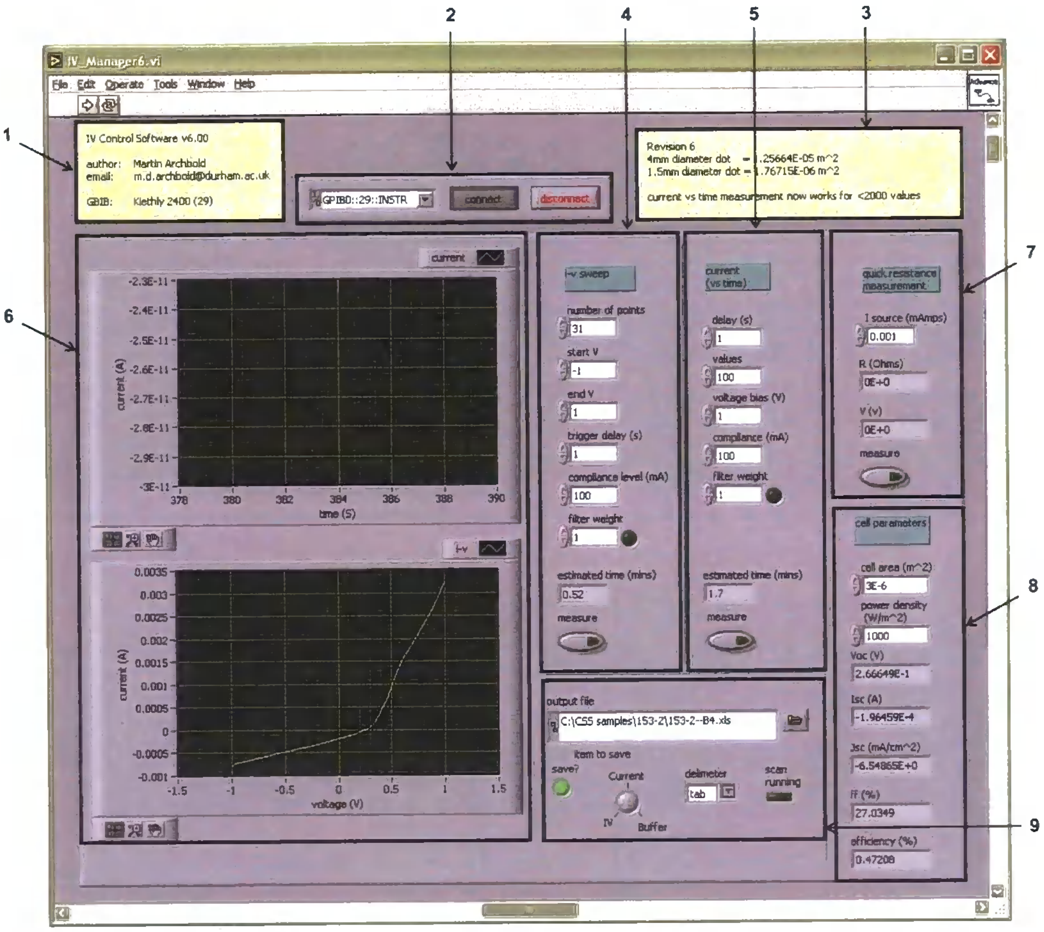

IV Control Software v6.00

author: Martin Archbold
email: m.d.archbold@durham.ac.uk

GBIB: Klethly 2400 (29)

GPIB0::29::INSTR

Revision 6
4mm diameter dot = .25664E-05 m^2
1.5mm diameter dot = .76715E-06 m^2

current vs time measurement now works for <2000 values

number of points: 31
start V: -1
end V: 1
trigger delay (s): 1
compliance level (mA): 100
filter weight: 1
estimated time (mins): 0.52

delay (s): 1
values: 100
voltage bias (V): 1
compliance (mA): 100
filter weight: 1
estimated time (mins): 1.7

I source (mAmps): 0.001
R (Ohms): 0E+0
V (v): 0E+0

cell area (m^2): 3E-6
power density (W/m^2): 1000
Voc (V): 2.66649E-1
Isc (A): -1.96459E-4
Jsc (mA/cm^2): -6.54865E+0
FF (%): 27.0349
efficiency (%): 0.47208

output file: C:\CSS samples\153-2\153-2--B4.xls
item to save
save?
delimeter: tab
scan running

Figure 4.13. IV apparatus control software, refer to text for description of numbered sections.

The control software (Figure 4.13) is composed of nine sections, these are described below (note that sections 5 and 8 will be discussed in sections 4.2.3.3 and 4.3.3.3 respectively):

1. Software revision version
2. Device connection management
3. Software revision information
4. IV sweep input parameters
5. Current versus time sweep input parameters (section 4.2.3.3)
6. Graphical display of results
7. Quick resistance measurement (to check that there is not an open circuit)
8. PV device parameters (section 4.3.3.3)
9. File input/output parameters.

4.2.3.3. Illumination-dependent conductivity

Illumination-dependent conductivity measurements were performed using the same apparatus as described in section 4.2.3.2, however the current versus time sweep option (option 5 in Figure 4.13) is utilised. Here a constant potential is applied to the sample, and the current is measured at set intervals (typically every second), this is done in the dark and under $AM_{1.5}$ illumination in order to assess the effect this has upon the photoconductivity of the sample.

4.2.3.4. Four point probe

The four point probe technique is used to measure the bulk and sheet resistivity values of materials. Four regularly spaced ohmic contacts (Figure 4.14) are made to the surface of the sample which can be of arbitrary shape, a constant DC current is then applied to the outer two contacts and the potential difference is measured between the inner contacts.

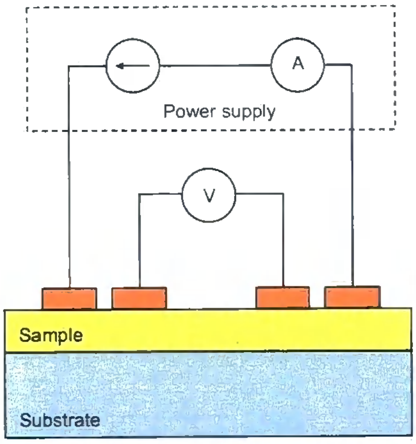

Figure 4.14. Four point probe apparatus.

As negligible current is drawn by the voltmeter, there is no current flowing through the inner contacts and therefore the contact resistance can be neglected. By knowing the current through the sample, the potential drop and the distance between the contacts, the resistivity is given by:

$$\rho_0 = 2\pi s \frac{V}{I} \tag{4.23}$$

[5] where s is the probe spacing. This model assumes that the sample is of semi-infinite volume, in practice two correction factors are applied, C_1 which accounts for the edge effects due to the sample being finite in extent in the plane of the sample and C_2 which accounts for the finite sample thickness (t). The true resistivity is then given by:

$$\rho = \frac{Vt}{I} C_1 C_2 \tag{4.24}$$

and therefore the sheet resistance is given by:

$$R_s = \frac{\rho}{t} \tag{4.25}$$

$$R_s = \frac{V}{I} C_1 C_2 \tag{4.26}$$

Correction factors for many different geometric configurations exist in the literature [6]. The apparatus used in this study consisted of four moveable spring-loaded gold-plate tipped probes, the current source (Keithley 2400) and electrometer (Keithley 6487) were controlled by a Labview software system. Contacts were verified as being ohmic by performing an IV sweep prior to measurement.

4.2.3.5. Van der Pauw

The van der Pauw method [7] is a variation on the four point probe technique mentioned above. It is attractive as it does not require the application of correction factors due to edge effects, and also the geometry lends itself easily to Hall effect measurements (Section 4.2.3.6). An arbitrary shaped sample can be used, however in practice this is usually a square with four small ohmic contacts at the perimeter, most often the corners. The principle relies on measuring two characteristic resistances R_A and R_B as shown in Figure 4.15:

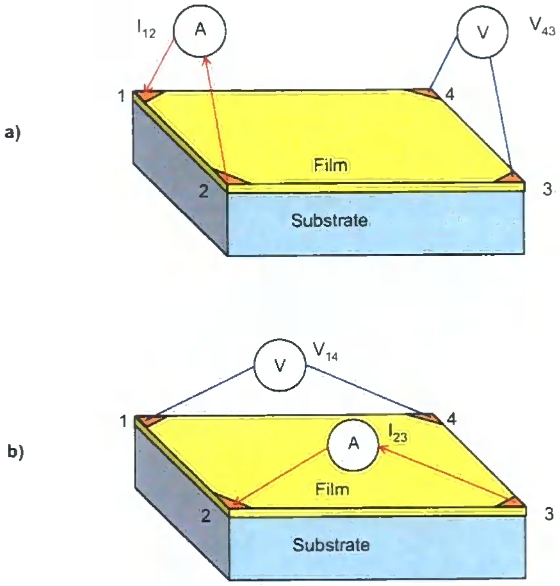

Figure 4.15. Measurement of two characteristic resistances a) R_A and b) R_B.

where:

$$R_A = \frac{V_{43}}{I_{12}} \tag{4.27}$$

and

$$R_B = \frac{V_{14}}{I_{23}} \tag{4.28}$$

The sheet resistance is then related to these two resistances through the following equation:

$$\exp\left(-\frac{\pi R_A}{R_s}\right) + \exp\left(-\frac{\pi R_B}{R_s}\right) = 1 \tag{4.29}$$

This can be solved numerically to give R_S, and then the corresponding bulk resistivity of the sample is given by equation 4.25. In this study the sample was placed in a custom made PTFE holder containing four spring-loaded gold tipped probes, each one making contact to the ohmic evaporated contact at each corner. The current was sourced and potential measured by two Keithley 2400 digital multimeters and a switchbox was used to speed up the process of taking multiple readings; a full detailed account of the technique and switchbox is given by Zoppi [8].

4.2.3.6. Hall effect

The Hall Effect in semiconductor materials [9] is a consequence of the Lorentz force acting on mobile charge carriers in the material. The force on the charge carriers is directed normally to both the applied magnetic field and the velocity of the charge carrier and as a consequence a Hall voltage is generated. The polarity of the Hall voltage tells us the type of charge carrier (electrons or holes) responsible for conduction thus giving the type of the semiconductor (*n*-type or *p*-type) and the sheet carrier density can be calculated from the relations:

$$n_s = \frac{IB}{q|V_H|} \qquad (n\text{-type}) \qquad (4.30)$$

$$p_s = \frac{IB}{q|V_H|} \qquad (p\text{-type}) \qquad (4.31)$$

with the bulk carrier density given by:

$$n = \frac{n_s}{d} \qquad (n\text{-type}) \qquad (4.32)$$

$$p = \frac{p_s}{d} \qquad (p\text{-type}) \qquad (4.33)$$

Then the Hall mobility can be calculated:

$$\eta = \frac{1}{qn_S R_S} \qquad (n\text{-type}) \qquad (4.34)$$

$$\eta = \frac{1}{qp_S R_S} \qquad (p\text{-type}) \qquad (4.35)$$

In practice the experiment is commonly applied using the van der Pauw geometry as described in section 4.2.3.5 with the addition of an applied magnetic field perpendicular to the plane of the sample. In this work the sample was subject to a magnetic field of approximately 3,000 Gauss (0.3 Tesla), generated from an iron core electromagnet; a full detailed account of the technique is given by Zoppi [8].

4.2.3.7. Electrolyte-based measurements

A series of electrolyte-based spectroscopy measurements were carried out at Bath University. These differ from the aforementioned electrical measurements in that the front contact used was not a metal but instead a liquid electrolyte solution, designed to give an ohmic or a Schottky contact dependent on the type of measurement desired. Three measurements types were performed, i) electrolyte-electroabsorbance (EEA) modulation spectroscopy, ii) photoresponse iii) and Mott-Schottky capacitance-voltage measurements. For a full treatment of these methods refer to Bard and Faulkner [10].

4.3. Characterisation of PV devices

4.3.1. Spectral response

Spectral response is a method used to quantitatively measure the external quantum efficiency of a PV device as a function of the wavelength of incident radiation; it is useful in determining many characteristics of a PV device. A schematic of the apparatus used in this study is shown in Figure 4.16.

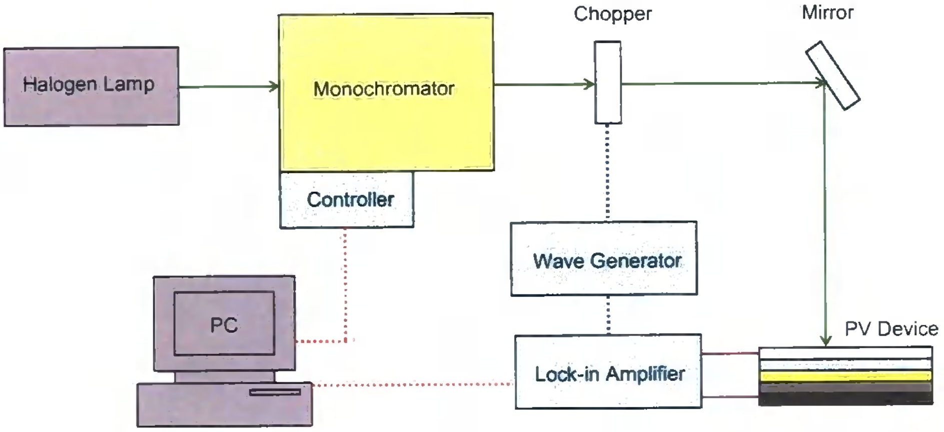

Figure 4.16. Spectral response apparatus.

A beam of monochromatic light is passed through a chopper and is incident on the PV device being investigated; the output current from this device is measured by means of a lock-in amplifier connected to a PC. This process is repeated as the incident beam is scanned through a wavelength range, typically from 400-900 nm in 1.5 nm intervals.

4.3.2. Current-voltage (IV)

The most important characteristic of a PV device is the efficiency at which it converts solar energy into electric power; this is measured by performing a current-voltage sweep (refer to section 4.2.3.2) under illumination. As discussed in section 2.5 many characteristics of a device can be obtained by evaluating the IV curves for a device against the equivalent circuit model. In this work, IV curves were taken under standard $AM_{1.5}$ illumination from an Oriel 81160 solar simulator (Figure 4.17) at a total intensity of 100 mW/cm^2 (calibrated with a standard silicon PV device) at room temperature. The spectrum of this illumination is close to that of natural $AM_{1.5}$ sunlight as discussed in section 1.2, and therefore the device output will be representative of real-world performance.

Figure 4.17. Oriel solar simulator, showing power supply and power output indicator (left bottom and top respectively), light output (centre), sample holder (centre-right) and Keithley sourcemeter (right).

The software and source meter used was as described in section 4.2.3.2, with the potential being swept from -1 to 1 V with approximately 50 points/V. By inputting the cell area the software also calculates the device parameters J_{sc}, J_{mp}, V_{oc}, V_{mp}, efficiency (η) and fill factor (FF) automatically. Additionally, due to the large volumes of IV device data collected during this study, a C++ software application was developed in order to automate the process of extracting device parameters from IV curves of each device.

4.4. References

1. Singh, J., *Semiconductor Devices - Basic Principles.* (Accessed:02/08/2006). http://www.eecs.umich.edu/~singh/bk7ch01.pdf

2. Madelung, O., ed. *Semiconductors - Basic Data.* 1996, Springer: Berlin.

3. Williamson, G.K. and W.H. Hall, *X-Ray Line Broadening from Filed Aluminium and Wolfram.* Acta Metallurgica, 1953. **1**(1): p. 22-31.

4. *Reproduced from the Perkin Elmer Elan 6000 user manual.*

5. Valdez, L.B., *Resistivity Measurements on Germanium for Transistors.* Proceedings of the Institute of Radio Engineers, 1954. **42**: p. 420-427.

6. Smits, F.M., *Measurements of Sheet Resistivity with the Four-Point Probe.* Bell System Technical Journal, 1958. **37**: p. 711.

7. van der Pauw, L., *A method for measuring specific resistivity and Hall effect of discs of arbitrary shape.* Philips Research Reports, 1958. **13**: p. 1-9.

8. Zoppi, G., *Studies of CdTe Thin Films and Solar Cells Grown by MOCVD*, in *Physics.* 2005, University of Durham: Durham, U.K.

9. Hall, E.H., *On a New Action of the Magnet on Electric Currents.* American Journal of Mathematics, 1879. **2**: p. 287-292.

10. Bard, A.J. and L. Faulkner, *Electrochemical Methods: Fundamentals and Applications.* 2001, London.: John Wiley and Sons. 856.

5. Solution deposition of CdS

5.1. Introduction

The main body of this work focuses on the growth and characterisation of CdS grown by the solution deposition (SD) technique. In this chapter the fundamentals of the technique are described, a review on the subject is given with reference to the conditions that control deposition and then the novel SD method devised and used in this work is outlined in detail. In the final section the results of an ICP-MS impurity analysis are described.

5.2. Fundamentals

5.2.1. Chemical route

SD is a simple, low cost method of preparing thin films. The technique involves the controlled precipitation of material onto a target substrate which is typically immersed in a heated liquid solution; the solution is in general aqueous and contains the precursors for the growing film. Many substances can be grown using SD, here the discussion will concentrate on CdS which was one of the first materials to be grown using the technique [1]. Typical solution components are:

- Cadmium source, typically a salt such as cadmium chloride ($CdCl_2$)
- Sulphur source, often thiourea ($SC(NH_2)_2$)
- Complexing agent for the metal, often an amine ligand such as ammonia (NH_3) or ethylenediamine ($NH_2(CH_2)_2NH_2$), this is important in controlling the free metal ion concentration and hence the reaction rate.

Here the process is described briefly, the sulphur source in this example is thiourea, and the complexing agent used is NH_3. The process proceeds by the following steps, firstly equilibrium is set up between the complexing agent and water:

$$2NH_3 + H_2O \rightarrow 2NH_4^+ + 2OH^- \tag{5.1}$$

This has two consequences, firstly the ammonium ion is able to complex the free cadmium ion thus making it unavailable for immediate reaction:

$$Cd^{2+}(aq) + 4NH_3 \rightarrow Cd(NH_3)_4^{2+} \tag{5.2}$$

and additionally the presence of the hydroxide ions bring about the hydrolysis of the sulphur source:

$$(NH_2)_2CS + OH^- \rightarrow S^{2-}(aq) + H_2NCN + 2H_2O \tag{5.3}$$

Thus when the metal ligand complex disassociates:

$$Cd(NH_3)_4^{2+} \rightarrow Cd^{2+} + 4NH_3(aq) \tag{5.4}$$

the CdS solid is formed in a controlled manner:

$$Cd^{2+}(aq) + S^{2-} \rightarrow CdS(s) \tag{5.5}$$

It is important to note that there is almost no dissociation of this CdS by the reaction:

$$CdS(s) \Leftrightarrow Cd^{2+}(aq) + S^{2-}(aq) \tag{5.6}$$

as the solubility product (K_{sp}) of the compound is extremely low:

$$K_{sp} = \left[Cd^{2+}\right]\left[S^{2-}\right] \tag{5.7}$$

$$K_{sp} = 10^{-28} \tag{5.8}$$

The chemical route presented above (termed the *simple ion-by-ion* formulation) is almost certainly a simplification of the actual mechanism that occurs in reality. Hodes [2] gives an in-depth description of other proposed mechanisms.

5.2.2. Nucleation

Nucleation refers to the process of atomic and molecular species (Cd^{2+} and S^{2-} ions in the simple description outlined above) crystallising to form bulk material. There are two methods of nucleation pertinent to the formation of CdS, homogeneous (cluster) and heterogeneous (ion-by-ion) nucleation.

5.2.2.1. Homogeneous

Homogeneous precipitation takes place within the bulk of the solution and not on the substrate or reaction vessel, as such it is an undesirable process and steps are taken to minimise this type of nucleation. CdS will precipitate from solution when the product of the concentrations of Cd^{2+} and S^{2-} exceed the solubility product of CdS, this is known as *supersaturation*. Homogeneous nucleation is thought to occur by the formation of initial small CdS particles, or *embryos*, by the collision between free Cd^{2+} and S^{2-} ions. These embryos will tend to dissolve immediately as they have large surface areas and corresponding high surface energies and so are thermodynamically unstable (Govendar gives a full treatment [3]). However, they can increase in size by further collisions with ions or by coalescescing with other embryos, and in so doing increase their size to a critical radius. A particle of this size is referred to as a *critical nucleus* and is stable due to a balance between the surface energy required to form the embryo and the energy released when the embryo is formed [2]. This will occur more often in solutions with higher levels of supersaturation, and therefore this process can be controlled by modifying the deposition conditions, in particular the free ion concentration. If a substrate is present in the reaction solution, it is possible that some of the clusters will migrate and adhere loosely to the substrate (Figure 5.1).

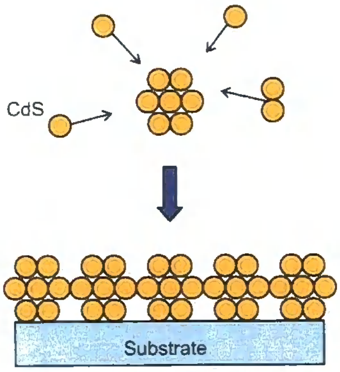

Figure 5.1. Film formation by homogeneous nucleation.

In this case a film may be formed; however the optical, structural and electrical properties of such a film will not be suitable for application in PV devices.

5.2.2.2. Heterogeneous

In this process ions or sub-critical embryos are adsorbed onto the surface of the substrate (the location of adsorption is discussed in 5.2.3). As this is more energetically favourable than homogeneous nucleation (the energy of formation of nuclei on the surface is less than that of a free nuclei in solution), this process will occur at lower levels of supersaturation. In this type of nucleation a continuous film will often be formed (Figure 5.2). Such films will likely be suitable for use in PV devices as the structural, optical and electrical properties will be favourable.

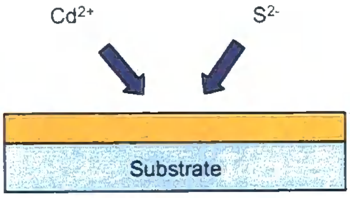

Figure 5.2. Film formation by heterogeneous nucleation.

5.2.3. Crystal growth

In order for a crystalline film to be formed, the constituent growth units must be incorporated onto the substrate surface in a regular manner. For the case of heterogeneous growth, this is thought to proceed by the adsorption of Cd^{2+} and S^{2-} ions at energetically favourable sites. Figure 5.3 shows a crystal surface with three potential growth areas:

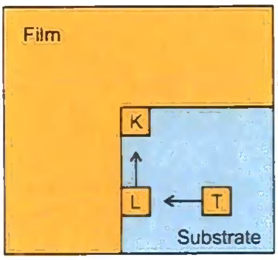

Figure 5.3. Film surface (shown from above) with three potential growth sites: i) terrace (T), ii) ledge (L) and iii) kink (K).

It is energetically favourable for a growth unit to form on a site which minimises its surface area, therefore the order of preference of favoured growth positions will be kink sites, followed by ledge sites followed by terrace sites. It is thought therefore that growth proceeds by the following sequence:

- A growth unit forms on the substrate (T), as this surface represents the majority of the film surface the probability of the unit initially being formed here is high
- The unit migrates to an L site where it has a lower surface area
- The unit migrates to a K site where the surface area is again reduced.

In this way a film is grown from K sites outwards along the plane of the film, thus producing long range crystal order. The adsorption process will continue until all the ions of any one type are used up or the growth is blocked by an irregular growth unit or a foreign adsorbed species. The growth may also be stopped and subsequently continue in a different geometric orientation, giving rise to a polycrystalline film, as is typically the case for SD films. Other growth mechanisms that may also occur include aggregation and coalescence; here two particles attract one another by the van der Waals force and can either coalesce to form a single particle, or aggregate to form a cluster of particles. These mechanisms are treated in detail by by Hodes [2].

It should be noted that typically films are grown on substrates having surface morphologies with features significantly larger than the grain size of the growing film, therefore the idealised discussion mentioned above is substantially modified, this is the case in this study and will be explored in section 5.5.3.

5.2.4. Kinetics

Solution deposition as a function of time is thought to proceed via three steps, i) induction, ii) linear growth and iii) termination; Figure 5.4 shows these three phases for a typical deposition. In the induction phase the sulphur concentration is increasing (via the disassociation of the sulphur source) but is still too low to allow initial nucleation to occur, this represents a delay between the start of the experiment and the onset of film growth. In the growth phase (which is often found to be approximately linear with time) growth occurs on these nuclei, and finally the reaction terminates when the reactants are depleted.

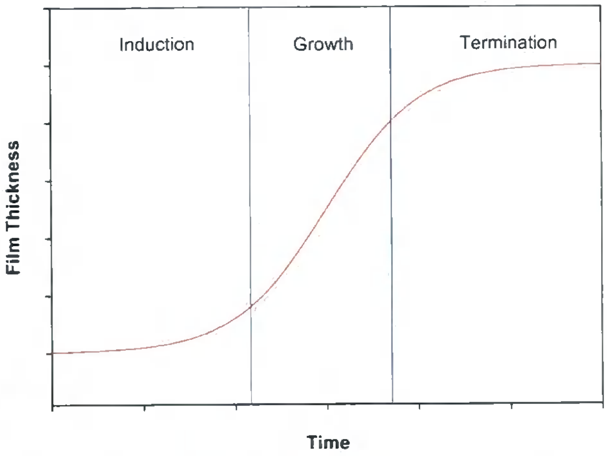

Figure 5.4. Typical growth kinetics for solution deposition film growth.

Section 5.5.3 investigates the growth kinetics for the CdS growth method used in this study.

5.3. Deposition conditions - A literature review

There are many studies in the literature that deal with the solution deposition of thin film CdS; in the following discussion some of the important practical deposition conditions and parameters are discussed along with a selection of research findings.

5.3.1. Temperature

Growing at high temperatures promotes the disassociation of the stable cadmium metal complex, thus increasing the free cadmium concentration and inducing the conditions of supersaturation. One effect of this is that the reaction rate is increased [4], which may have consequences on the character of the growing film. Doña et al [5] found that a variation in deposition temperature produced a marked effect on the bandgap of deposited films, increasing from 2.45 to 2.50 eV at 75°C and 65 °C respectively. Wenyi et al [6] found that at higher temperatures there was a remarkable change in surface topology, with the presence of less pinholes, a smaller grain size and lower surface roughness; they also found a clear reduction in the bandgap of films at higher deposition temperatures, in agreement with Doña. Duncan et al [7] found that the stability of deposition temperature also has an effect, and that films grown with a good temperature stability are stoichometric, and show good adhesion properties.

5.3.2. pH

The pH of the chemical solution determines the extent to which the metal complex is formed and also is important in determining to what extent the undesirable precipitation of cadmium hydroxide occurs. A higher pH (more alkaline) will generally increase the rate of deposition (as the thiourea decomposition rate will be increased, by equation 5.3), however increasing the reaction rate too far will increase the likelihood of homogeneous deposition which will reduce the final film thickness. Studies have shown that solution pH can have a marked effect on the optical and structural properties of solution grown CdS [5, 8], however it is often found that by moving too far away from an optimum pH a film is no longer produced, either no reaction occurs, the reaction is homogenous or cadmium hydroxide is precipitated rather than CdS. There have been studies of CdS grown from acidic baths [9], although this deposition type was not attempted in this study.

5.3.3. Cd salt

Several different salts can be used as the cadmium source, common choices are cadmium chloride ($CdCl_2$), cadmium acetate ($Cd(CH_3COO)_2$), Cadmium sulphate ($CdSO_4$) and cadmium nitrate ($Cd(NO_3)_2$). Studies have investigated the properties of films grown using these different sources (for example [10]), however no appreciable trend has been observed.

5.3.4. Concentration of Cd and S sources

An increase in the cadmium and thiourea concentrations (with constant complexing agent concentration) will lead to an increase in reaction rate as expected; this has been shown to have major effects on film formation and quality. Guillen and Martinez have studied the optical properties of CdS films with changes in the concentrations of the cadmium salt and thiourea [11, 12], they found that good optical transmission, most likely due to heterogeneous film formation, was sensitive to these concentrations and an optimal Cd to S source ratio value was determined for their chemical route. Other studies have found variations in the bandgap energy as a function of source concentrations [5], as well as grain size and photoconductivity values [13].

5.3.5. Complexing agent

The complexing agent is used to buffer the concentration of the free metal ion, therefore limiting global precipitation of CdS in the bulk solution; it follows that if a different complexing agent is used then the reaction chemistry will be modified. The typical complexing agent used is ammonia (NH_3), however many others have been used such as sodium citrate [14], potassium nitrilotriacetate [15], potassium cyanide [16], triethanolamine (TEA) [17], ethylenediamine (EN) [18] and ethylenediaminetetraacetic acid (EDTA) [19]. Other authors have used additional complexing agents with ammonia such as ammonium sulphate [20] and EDTA [21] and found the resulting films to have superior optical transmission than with ammonia alone. This effect has been ascribed to stronger complexation leading to a reduction in homogeneous growth.

5.3.6. Magnetic field

Vigil et al have explored CdS film growth under the influence of a (0.077 Tesla) magnetic field [22, 23]. They studied optical transmission, dark resistivity, surface morphology and x-ray diffraction patterns as a function of magnetic field; preliminary results found that the presence of the field produced thicker films with lower resistivity (as would be expected from thicker films when measured in the coplanar contact geometry, refer to section 5.5.5.3) and a smaller grain size. It is not clear by what possible mechanism these modifications may have occurred.

5.3.7. Ultrasonication

Choi et al [24] have studied the growth of CdS under the influence of ultrasonic agitation. Compared to no agitation they found a marked difference in surface morphology, growth rate and optical properties. It was also found that colloidal particles were not present, which is a sign of homogeneous growth, and surface roughness was found to be reduced by a factor of two. Zhu [25] also found a strong improvement in surface morphology with ultrasonic treatment during growth.

5.3.8. Stirring

The reactant solution is generally stirred using a PTFE coated magnetic follower immersed in the solution, this mixing action is thought to decrease the homogeneous growth in the solution by reducing inhomogeneous temperature variations, and also increasing the growth rate on the substrate surface by transporting a greater flux of precursor material to the substrate. There have been some notable variations on this, Sasikala et al [26] devised apparatus which stirred the substrate itself by using a substrate attached to the axle of an electric motor , whilst Boyle et al [27] used a novel approach designed to reduce the waste incurred by homogeneous reaction by circulating the reactant solution over a heated substrate. This latter geometry was further studied by Archbold et al [28].

5.4. Novel solution deposition method

In this work a novel SD technique [29] was employed in order to overcome many of the problems associated with conventional methods. In the discussion below the problems with conventional SD are outlined and then the solutions applied in this study are discussed.

5.4.1. Issues in solution deposition

5.4.1.1. Pinholes

A common problem with solution based techniques is the formation of gas bubbles on the substrate surface during growth. These have the effect of blocking the reactants from growing on the substrate near the site of bubble residence, and thus a circular area of the substrate remains uncovered, this is known as a *pinhole* (Figure 5.5).

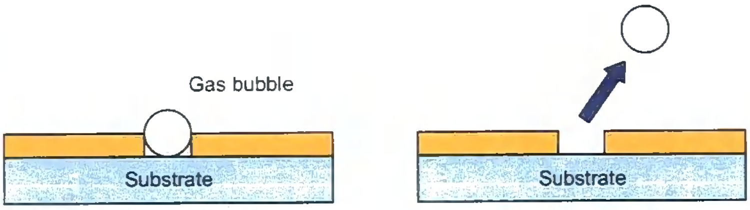

Figure 5.5. Pinhole formation due to a gas bubble resident on the film surface.

Figure 5.6 shows an SEM image of a CdS film, the central area contains a 500 μm diameter pinhole.

Figure 5.6. SEM image of a 500 μm diameter pinhole on a CdS film, magnification used is 72 times.

The low-tech solution to this problem is often to simply tap the substrate to knock the adherent bubbles off, however this requires standing over the reaction for the duration of growth, and also some bubbles not visible to the naked eye may be present and form pinholes. Therefore a novel nitrogen gas bubbling system was employed in this study, this comprised of a PTFE tube below the substrates which had approximately 50 small holes drilled into its length. Pressurised (~2 bar) nitrogen gas was injected into it in order that small nitrogen bubbles escape through the tube and are incident upon the substrate (Figure 5.7), thus knocking of any resident gas bubbles present.

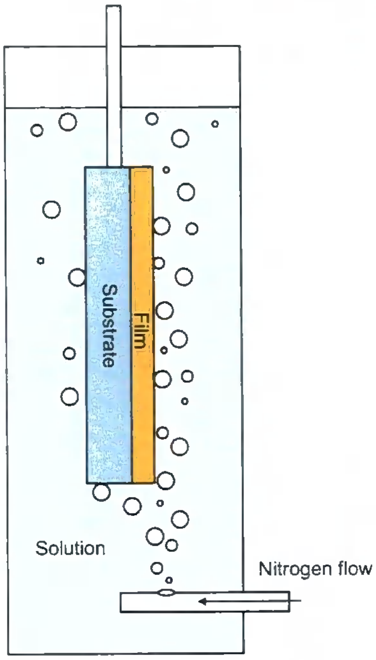

Figure 5.7. Schematic of N_2 bubbling system.

Another feature of the deposition in this study is that a low deposition temperature was used, therefore the volume of gas which will come out of solution will be reduced at source. The total effect of both these features is that both the formation and residence of bubbles is reduced, thus reducing the number of pinholes formed in growing films.

5.4.1.2. Colloidal particles

If the reaction proceeds via a homogeneous nucleation route, the growing film will consist of colloidal clusters as discussed in section 5.2.2.1, an SEM image of actual colloidal clusters with an approximate size of 400-800 nm is shown in Figure 5.8.

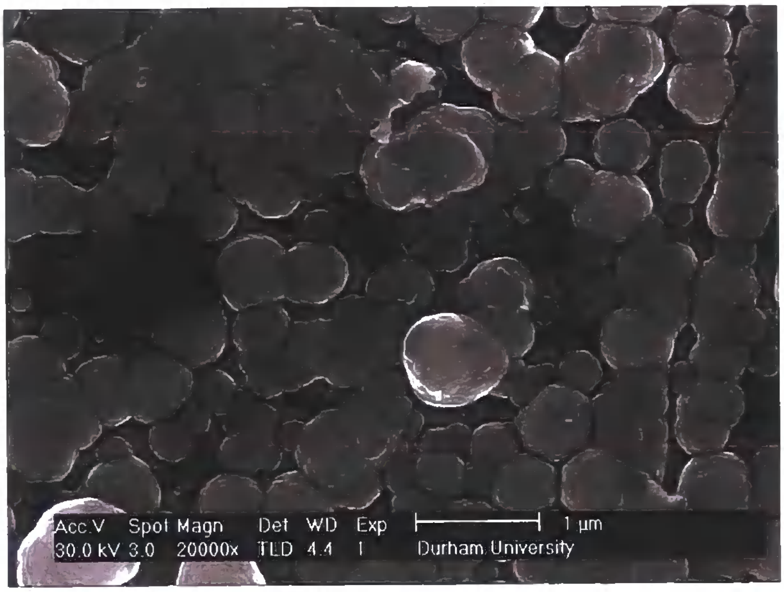

Figure 5.8 SEM image of a CdS film composed of colloidal particles, magnification used is 20k times.

This is undesirable as it results in a greatly reduced level of optical transmission due to increased scattering and therefore this type of growth should ideally be minimised. Two types of chemical route were initially explored in this work, deposition using the conventional complexing agent ammonia (NH_3) and an alternative ethylenediamine (EN) [18, 27, 30]. It was found empirically that the EN route produced films with less colloidal particles, and therefore this was chosen for all further work. This route was subsequently optimised, and it was found that by reducing the temperature of the reaction from the more typically employed 65°C to 30°C a further reduction in colloidal particle formation was observed, this reaction temperature was used in all subsequent work. The use of EN has two further desirable effects described in the following sections 5.4.1.3 and 5.4.1.4.

5.4.1.3. Use of ammonia

Ammonia in aqueous solution is a volatile and hazardous compound, it is irritating to the eyes, skin and the respiratory and digestive systems, highly toxic to aquatic animals and is therefore is classified as dangerous to the environment. Replacing ammonia with EN significantly improves the safety of the process and also reduces the negative environmental impact of ammonia use. Although EN is corrosive and harmful by inhalation, the concentration required in the SD solution is of the order of

500 times less than ammonia due to it being a far stronger complexing agent than ammonia. The enhanced properties of EN as a complexing agent has been discussed by Bayer and Boyle [27, 30].

5.4.1.4. Cd concentration

The Cd concentration used in typical NH_3 based SD deposition solutions is between 2 and 4 mg per ml [14]. The majority of this is precipated homogenously as CdS in the reactant solution and therefore if it is not recycled (which is typically the case in research laboratory work) the majority of Cd will be disposed of as waste. Modelling of six different complexing agent strengths (EN, 1,2-diaminopropane, NH_3, ethanolamine, TEA and hydrazine) for cadmium has been performed by Boyle et al [27], this work showed that EN is a better complexing agent than ammonia for cadmium, as it allows far lower Cd concentration to be used. In this study the EN chemical route is employed, this uses Cd concentrations of around 0.1 mg per ml of starting solution, between 20 and 40 times less than that used by the conventional NH_3 based chemistry. Assuming small batch production methods are used, this concentration reduction would typically corresponds to an actual reduction in Cd usage of around 200 g for every 1 m^2 of 100 nm thick research scale CdS that is deposited; this clearly has beneficial environmental consequences.

5.4.1.5. Uneven film coverage

As discussed in section 5.3.1, high temperatures promote the disassociation of the stable cadmium metal complex, thus increasing the rate of reaction. Therefore if a temperature gradient exists in either the SD solution or substrate, then this may encourage inhomogeneous CdS growth giving an uneven CdS thickness. This is an undesirable effect and so every effort is made to ensure there are no temperature gradients present. In this study a deposition bath was constructed (described further in section 5.4.2) utilising a large surface area in contact with the solution, thus maximising the heat conduction to the solution. Also, by using a water bath with a large reservoir to heat the walls it was ensured that the walls of the reactor are kept at a constant temperature throughout the deposition.

Another common problem often results from over-vigorous stirring of the solution. If rapid currents are present then this may enhance or depreciate growth rate on certain areas of the substrate; therefore ideally the solution should flow smoothly over the substrate. This is performed in this study by utilising only stirring due to the flow of nitrogen gas over the substrate (as described in 5.4.1.1), no magnetic stirring was employed.

5.4.2. Deposition apparatus and conditions

The experimental apparatus used for the main body of this work consists of a reaction bath with two parallel 20x20 cm square glass plates separated by 2 cm, the solution in which the substrates are immersed during growth (maximum volume 600 ml) is held between and heated by these plates. Each plate has a cavity in which heated water is circulated; this is kept at the set temperature (20-90°C) to within a tolerance of 0.05°C by a Grant GD100 water bath. The deposition process proceeds as follows:

- Water heating is turned on and the required temperature is set
- Nitrogen bubbling is turned on
- Chemicals are added to bath:
    - DI Water (460 ml)
    - $CdCl_2$ (43.8 ml of 0.05 M solution)
    - EN (1751 μl of 15 M solution)
    - NaOH (27.4 ml of 0.2 M solution)
- Substrates are placed in solution (supported by a PTFE holder)
- Solution temperature is left to equilibrate
- Thiourea is added (27.4 ml of 0.2 M solution) and timing is started
- After a set time, substrates are removed, rinsed in DI water and dried in a stream of nitrogen gas
- All liquid waste is stored for safe disposal.

The final chemical concentrations used are:

- $CdCl_2$ ($CdCl_2$, 0.004 mol dm^{-3})
- EN ($NH_2.CH_2.CH_2.NH_2$, 0.048 mol dm^{-3})

- NaOH (NaOH 0.01 mol dm^{-3})
- Thiourea ($CS(NH_2)_2$ 0.01 mol dm^{-3}).

A solution pH of 12 (at 20°C) was employed and the bath temperature was held at a constant 30°C for a typical deposition time of 60-140 minutes.

5.5. Results

Detailed below are the results of an investigation into the as-grown CdS films. This includes EDAX data showing film stoichiometry, an investigation into the nucleation processes, a thickness calibration run and a study investigating the effect of film thickness on the optical, structural end electrical properties of films. Finally the results of an ICP-MS chemical composition study are given.

5.5.1. Stoichiometry

In order study the stoichiometry of the as-grown films, EDAX spectra were taken on 100 nm thick CdS samples grown on glass. Figure 5.9 shows a typical spectra,

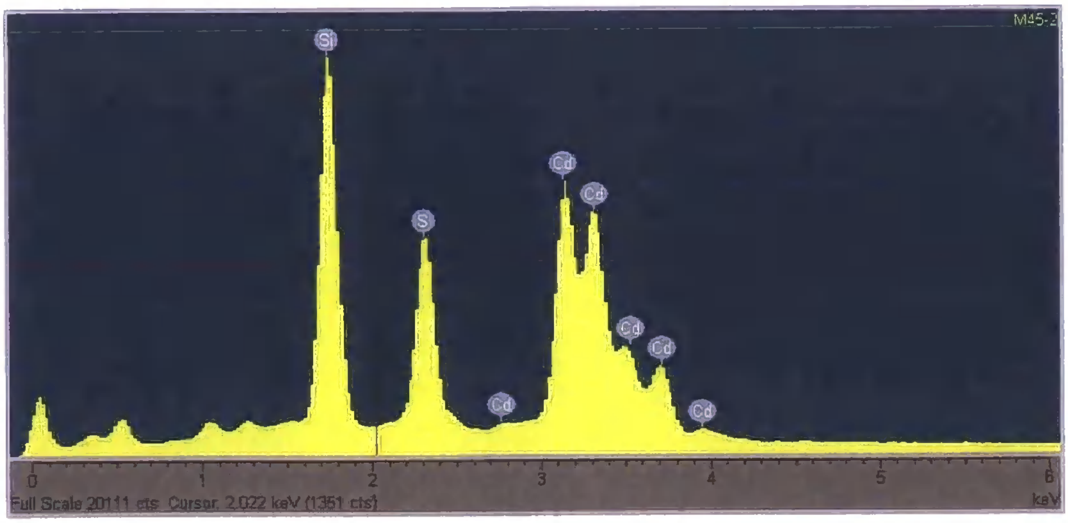

Figure 5.9. EDAX spectra of a CdS film.

The labelled peaks correspond to:

- Silicon L_α line - (1.74 eV)
- Sulphur L_α line - (2.31 eV)
- Cadmium K_α lines - (2.7 - 4.0 eV)

The glass substrate is responsible for the silicon signal, this is because the electron beam energy used in the instrument (20 keV) has a corresponding penetration length (simulated by the Casino Monte Carlo simulation software) of approximately 4 μm, significantly thicker than the CdS layer. By considering only the cadmium and sulphur lines and assuming there is no cadmium or sulphur in the glass substrate, the CdS stoichiometry results as calculated by the microscope software are presented in Table 5.1.

	S (%)	**Cd (%)**
Mean	48.32	51.68
Standard Deviation	0.88	0.88
Standard Error	0.40	0.40

Table 5.1. EDAX stoichiometry results (sample size of 5 measurements).

This shows that the film is cadmium rich in the proportion 1:1.07; this result is commonly found in the literature [2, 11].

5.5.2. Carrier type

Thermally stimulated current, Hall Effect and Mott-Schottky measurements were attempted, however due to the very high resistivity of as-grown CdS thin films, and the inability to form a Schottky junction with SD grown CdS films in this study, no carrier type information was possible. There exist no reports of *p*-type films in the literature, and therefore *n*-type conduction will be assumed henceforth.

5.5.3. Nucleation

A study was carried out in order to understand the process of nucleation and growth in CdS films. Films were grown of varying thicknesses on FTO substrates, and their morphology was examined *ex-situ* using the SEM technique. Figure 5.10 shows four CdS films in various stages of growth (with an FTO substrate for comparison), corresponding to film thicknesses of approximately 15 nm, 30 nm, 45 nm and 60 nm (thicknesses are estimated from calibration results, detailed in section 5.5.4). The initial 15 nm of the CdS layer (film b) appears to form a relatively smooth coating (compared to later growth stages) over the larger featured (100-400 nm) FTO grains. The majority of the film appears to be conformal over the substrate, however there are areas particularly at the boundaries of large FTO grains that appear to exhibit fissures where there may be no coverage or less coverage present. This could potentially cause problems in PV devices made from this material, since as discussed in section 2.5.2.2 short circuit paths in a device lead to high shunt resistances which in turn seriously depreciate performance. As growth progresses (films c and d) there is a clear increase in surface roughness and the appearance of round shaped features of the order of 50-100 nm. These seem to follow the underlying FTO grain structure and it is apparent that this becomes more noticeable in thicker films.

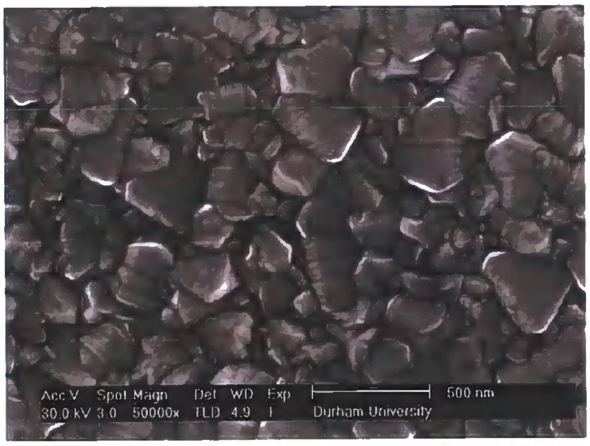

a)

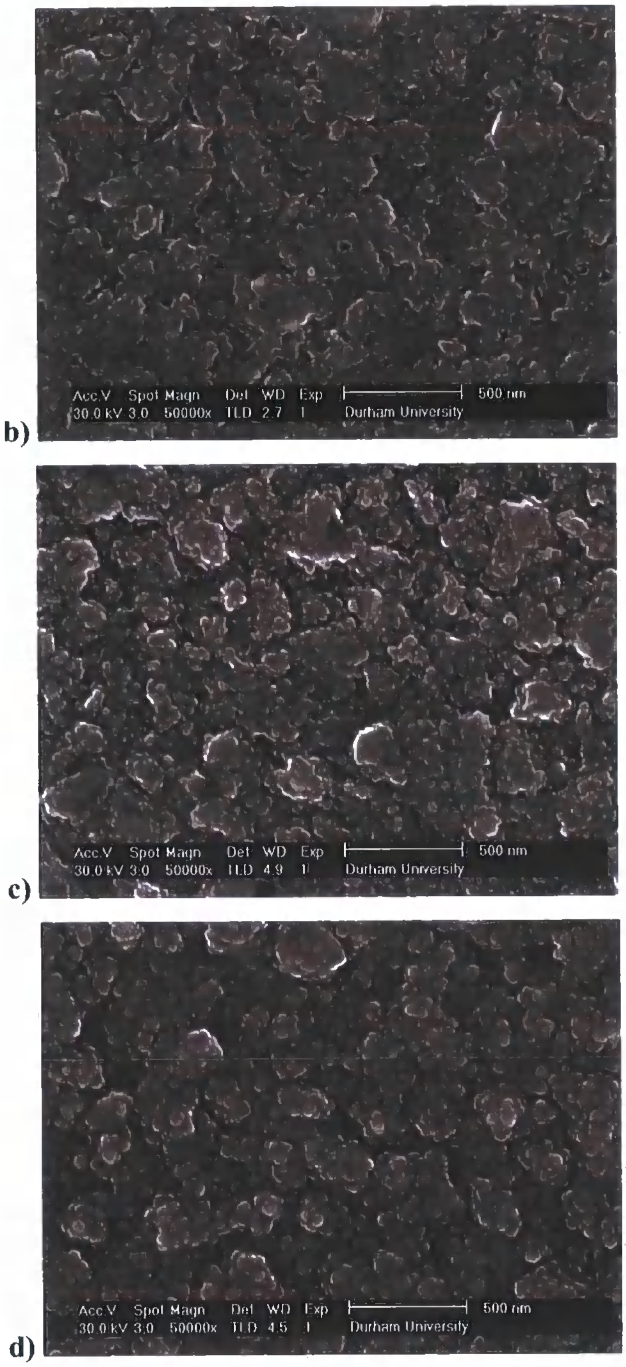
Acc.V Spot Magn Det WD Exp 500 nm
30.0 kV 3.0 50000x TLD 2.7 1 Durham University
b)
Acc.V Spot Magn Det WD Exp 500 nm
30.0 kV 3.0 50000x TLD 4.9 1 Durham University
c)
Acc.V Spot Magn Det WD Exp 500 nm
30.0 kV 3.0 50000x TLD 4.5 1 Durham University
d)

e)
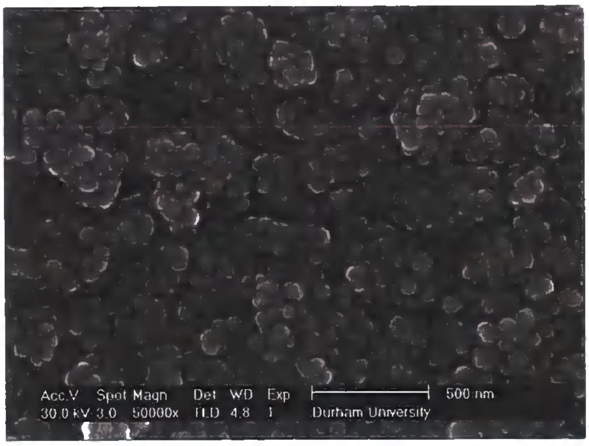

Figure 5.10. SEM images of a) FTO substrate and four CdS films in various growth stages with approximate thicknesses of b) 15 nm, c) 30 nm, d) 45 nm and e) 60 nm. Magnification used is 50k times.

This trend is seen to continue if thicker CdS films are considered, Figure 5.11 shows SEM images of a single 200 nm thick CdS film under magnification ranging from 20k – 150k times, this thickness is of the order of that used in a typical PV device and is therefore of great interest. These images clearly show that the tendency of the film to grow in 'clumps' becomes more pronounced at longer growth times. It is also noticeable in the highest magnification image (image d) that these conglomerations appear to be composed of smaller (~ 50 nm) features which in turn appear to have smaller features within them, however this scale is reaching the maximum resolution of the instrument.

a)
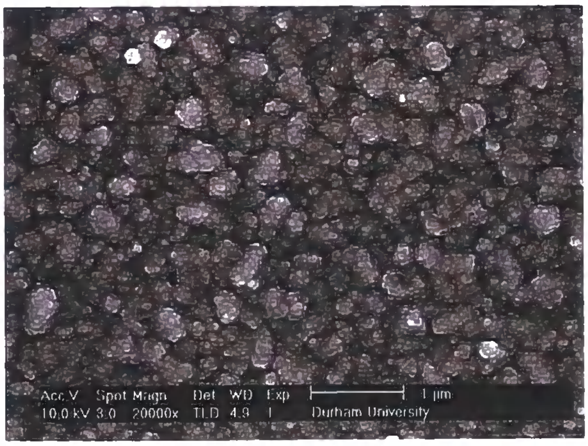

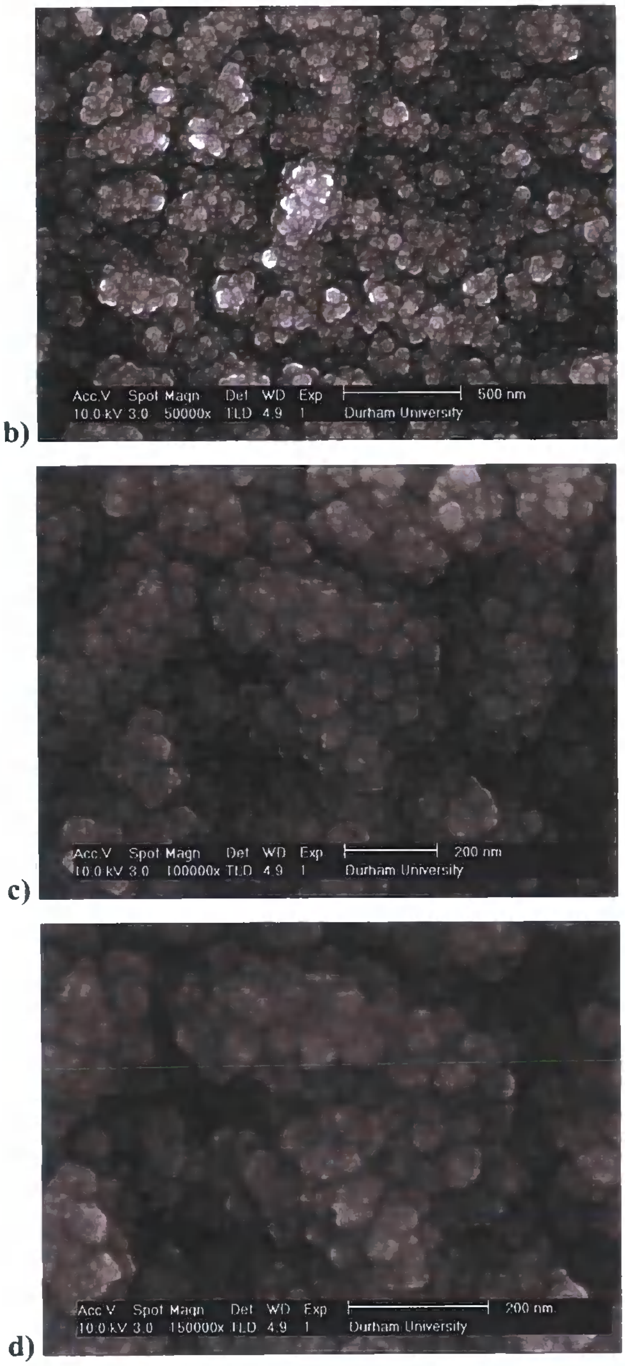

Figure 5.11. SEM images of a 200 nm CdS film, at magnifications of a) 20k, b) 50k, c) 100k and d) 150k times.

5.5.4. Thickness calibration

In order to grow films reproducibly it is necessary to calibrate the film thickness accurately against deposition time. Figure 5.12 shows the film thickness (measured *ex-situ* using a step profilometer) as a function of time; note that the minimum film thickness it is possible to measure using this method is approximately 55 nm.

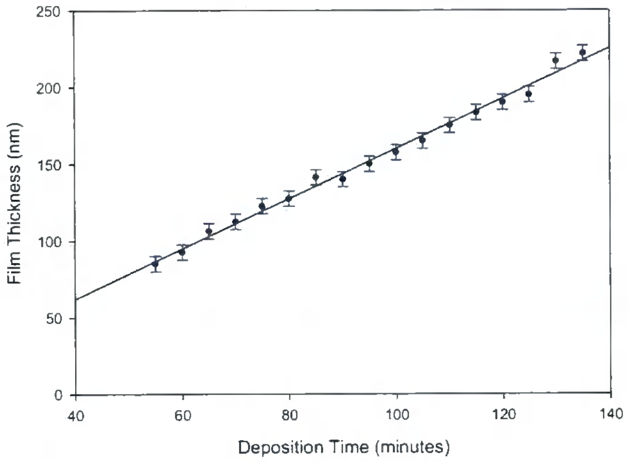

Figure 5.12. Thickness versus deposition time calibration, substrate used is Merck ITO.

As discussed in section 5.2.4 it is generally held that the growth profile is of a sigmoidal shape, however these results clearly indicate a linear growth pattern, suggesting there is little or no 'induction' phase in the growth. From these data it is also apparent that at 140 minutes the precursor materials have not yet been significantly depleted as the film growth is still proceeding. Film thickness calibration plots for other substrate types used in this study (FTO and glass) show identical growth characteristics.

5.5.5. Effects of film thickness

In order to study the effect thickness has on the properties of CdS films, six CdS samples were grown on glass and Pilkington FTO substrates with thicknesses in the range 50-300 nm (all sample thicknesses were measured and found to correspond to their design thickness to an accuracy of ±5 nm). Measurements performed were optical transmission and electrical resistivity.

5.5.5.1. Optical transmission

Optical transmission results for all six films (grown on Pilkington FTO) are shown in Figure 5.13. As expected all films show a strong cut-off in transmission around the 2.4 eV region, corresponding to the typical bandgap value of CdS. It is also apparent that thinner films transmit a higher portion of the light in the 2.6-3.5 eV region, due to incomplete absorption.

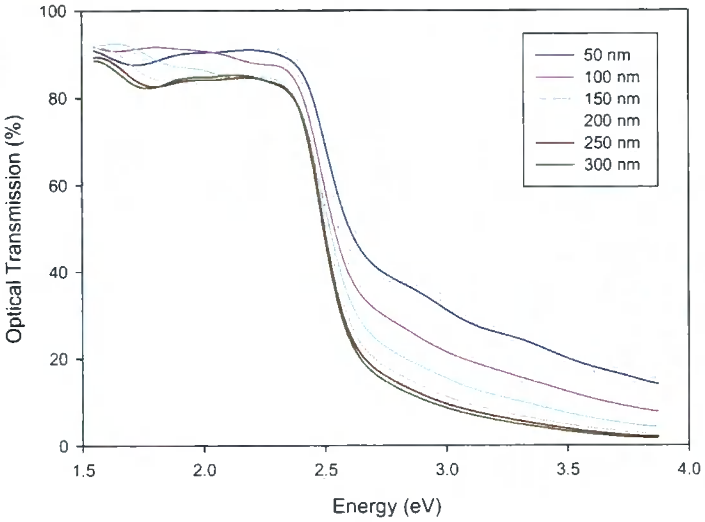

Figure 5.13. Optical transmission spectra for all films.

Figure 5.14 shows a plot of $(\alpha h\nu)^2$ versus energy for all six films.

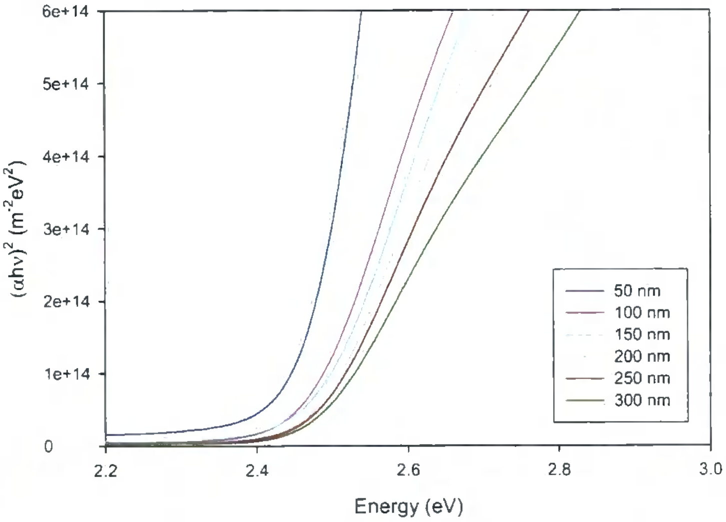

Figure 5.14. $(\alpha h\nu)^2$ as a function of energy for all films.

By taking the intercept of the tangent of each line to the energy axis it is possible to find the bandgap value for each film (section 4.2.1.2), Figure 5.15 shows these results. It is apparent from these data that to within experimental accuracy there is no perceptible change in bandgap value with film thickness; all bandgap values were found to be 2.42± 0.01 eV.

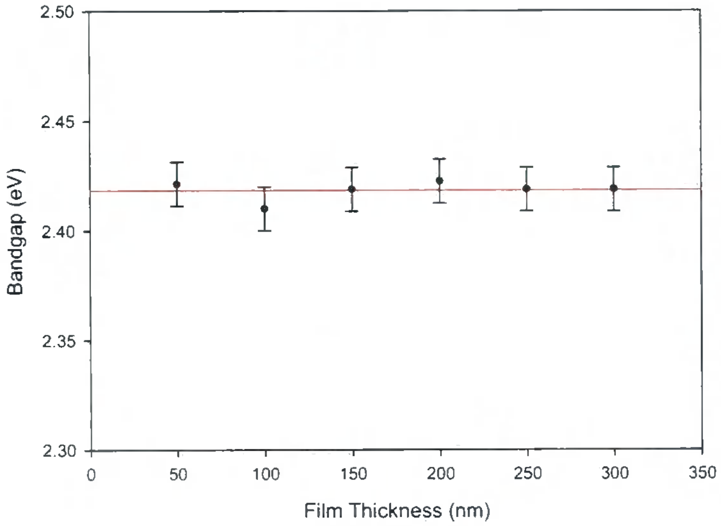

Figure 5.15. Bandgap as a function of film thickness for all films

When the transmission in the high energy region is compared to that of the $AM_{1.5}$ radiation profile (normalised to 100%) in Figure 5.16, it is apparent that a significant part of the energy spectrum of $AM_{1.5}$ radiation is contained at energies >2.5 eV, therefore this portion is essentially being lost through absorption by the CdS layer. The thicker this layer is the higher the blue loss will be which is important as it shows that in order not to lose this portion in a PV device the layer thickness must be minimised. However it is also apparent from Figure 5.16 that even a very thin 50 nm film will absorb a significant portion of the radiation in this region, and therefore significant blue loss is inevitable. This factor continues to motivate work into alternate *n*-type buffer layers with larger bandgaps.

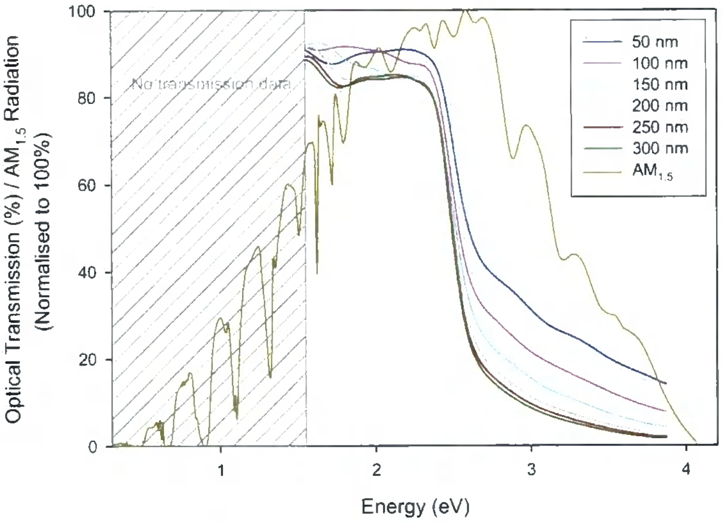

Figure 5.16. Comparison of optical transmission data with the $AM_{1.5}$ spectrum.

5.5.5.2. Electrical resistivity

Four point probe electrical measurements made under laboratory ambient lighting for all six samples are shown in Figure 5.17.

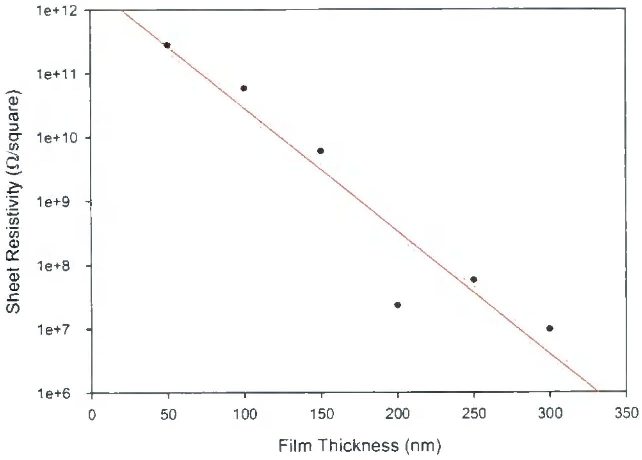

Figure 5.17. Electrical resistivity versus film thickness made by the four point probe technique.

There is a clear trend in that the film resistivity rises exponentially with reducing film thickness (Figure 5.17 is plotted on a log-linear scale), in agreement with previous work by Enriquez [31]. This behaviour cannot be described by treating the film as a continuous layer, but instead must arise from the complicated grain structure of the film and is therefore suggested as a topic for further study.

5.6. ICP-MS impurity analysis

Solution deposition is a method which is typically carried out in a standard chemistry laboratory environment and not under cleanroom conditions. As such it is possible that impurities, whether from impure starting materials, dust contamination, unclean glassware or other non-sterile laboratory practices, will unintentionally be incorporated into grown films. As the vast majority of semiconductor devices are very sensitive to impurities, it is therefore informative to investigate to what extent this type of contamination occurs. In this study this has been done in the following way: firstly the starting chemical solutions are analysed in order to assess their impurity levels, and then secondly CdS thin films are grown by solution deposition and it is investigated whether any of the impurities from starting solutions or impurities from other sources have been incorporated into the films.

5.6.1. Starting solutions

The four chemicals used in the standard SD method in this study (as described in section 5.4.2), including their source and manufacturers specification are shown in Table 5.2.

Chemical	Source	Grade
$CdCl_2$	Acros Organics	98.60%*
EN	Fisher Scientific	98%
NaOH	Fisher Scientific	99.02%*
Thiourea	Fisher Scientific	99.20%*

Table 5.2. Chemicals used in CdS growth starting solutions (* indicates the figure is from a certificate of analysis (COA), no COA is given for EN).

The relatively low grade chemicals are ones typically used in the growth of CdS by SD. To analyse the impurity content of these starting chemicals, two samples of each were added to 18 MΩ deionised water in trace-metal free containers, taking care to minimise cross contamination, ICP-MS data were taken on both sample sets to ensure consistency. Table 5.3 shows the impurities present in the four starting chemicals, bearing in mind the limitations of the ICP-MS apparatus as mentioned in section 4.2.2.5. The figure is an average of the two samples. Note that DI water has been omitted from this analysis as no trace of any impurity was found. The figures have been normalised so that they represent the ppb concentration (equivalent to ng per ml) that would be present in a typical SD starting solution from which CdS films are grown in this study. The respective concentrations in the final solution are: $CdCl_2$ 0.001 mol dm^{-3}, EN 0.012 mol dm^{-3}, NaOH 0.01 mol dm^{-3} and thiourea 0.01mol dm^{-3}.

Element	**$CdCl_2$ (ppb)**	**NaOH (ppb)**	**EN (ppb)**	**Thiourea (ppb)**	**Total (ppb)**	**Impurity:Cd ratio of total (by atom) in solution**
Cr	-	-	-	213.4	213.4	$4.1x10^{-3}$
Mn	5.7	-	-	-	5.7	$1.0x10^{-4}$
Cu	-	-	1.7	1.1	2.8	$4.4x10^{-5}$
Zn	79.5	-	-	-	79.5	$1.2x10^{-3}$
As	-	-	-	6.2	6.2	$8.3x10^{-5}$
Sr	-	8.0	-	47.9	55.9	$6.4x10^{-4}$
Sb	-	-	-	1.2	1.2	$9.9x10^{-6}$
Ba	213.9	-	-	7.7	221.6	$1.6x10^{-3}$
Tl	6.3	-	-	-	6.3	$3.1x10^{-5}$
Pb	1.0	-	-	-	1.0	$4.8x10^{-6}$
Total	306.4	8.0	1.7	277.5	593.6	

Table 5.3. Impurities present in a typical SD starting solution.

The following conclusions can be drawn:

- The largest proportion of impurities originate from the $CdCl_2$ and thiourea sources
- There are ten measurable impurities, in order of abundance these are Ba, Cr, Zn, Sr, Tl, As, Mn, Cu, Sb and Pb
- The level of each impurity present is around 3 to 6 orders of magnitude smaller than the atomic concentration of the Cd atoms in solution.

SD grown CdS film will now be examined to determine whether the above impurities have been incorporated into CdS material, and if so to what extent.

5.6.2. CdS films

In this study two CdS samples were placed in a trace metal-free container and high purity (spectrographic grade) hydrochloric acid (HCl) solution (3% in DI water) was added for five minutes, this was sufficiently long enough to dissolve all the CdS film; this solution was then diluted down and analysed using ICP-MS. One complication that must be noted however is that it is inevitable extra impurities will originate from both the HCl and the substrate (as a small proportion of the substrate will be dissolved by the acid). By considering these interferences it was necessary to exclude the following elements from the analysis:

- Cu, As - due to HCl
- Zn - due to substrate.

Table 5.4 shows the measured number density of impurity atoms present in as-grown CdS films, this is presented alongside the Cd atom to impurity ratio and the percentage of impurity atoms which have been incorporated into the CdS films.

Element	**Measured impurity, shown as number density in CdS films (cm^{-3})**	**Impurity:Cd ratio**	**Percentage of starting impurity atoms incorporated into film**
Cr	$1.8x10^{18}$	$8.8x10^{-5}$	2.1
Mn	$7.3x10^{17}$	$3.6x10^{-5}$	36.3
Cu	-	-	-
Zn	-	-	-
As	-	-	-
Sr	ND	ND	ND
Sb	ND	ND	ND
Ba	$7.8x10^{16}$	$3.9x10^{-6}$	0.2
Tl	$4.1x10^{16}$	$2.1x10^{-6}$	6.6
Pb	$4.0x10^{16}$	$2.0x10^{-6}$	41.9

Table 5.4. Measured impurity values for CdS thin films. (Key: 'ND' = Not detected, '-' = unable to conclude due to interference.

From these data it is possible to conclude:

- Only impurity elements present in the starting solutions have been incorporated into the films and no additional impurities were detected. This strongly suggests that their origin lies in the starting chemicals. Assuming this to be true it can be stated:
    - High levels of Cr are present, however the level of Cr incorporation (assuming the starting solution to be the source) is low at 2%
    - High levels of Mn are present, the level of Mn incorporation (assuming the starting solution to be the source) is high at 36%
    - Pb incorporation (assuming the starting solution to be the source) is high at 42%, however the impurity level in the film is relatively low as the amount of Pb impurity in the starting solution is also low.

It must be noted that although these impurities are present in CdS films and evidence suggest that their origin lie in the starting chemicals, it is not known whether they have been incorporated into the lattice proper as substitutionals, reside as interstitials, or exist as particulates (whether in the film itself or on the surface). In chapter 6 intentional doping of CdS films with electrically active species is performed, and again the ICP-MS technique is used to confirm the presence of dopant species.

5.7. References

1. Mokrushin, S.G. and Y.D. Tkachev, Colloid Journal, 1961. **23**(3): p. 438.

2. Hodes, G., *Chemical solution deposition of semiconductor films*. 2003, New York: Decker.

3. Govendar, K., *PhD Thesis - To Be Published*. 2007, Manchester Materials Science Centre: Manchester.

4. Nair, M.T.S., P.K. Nair, and J. Campos, *Effect of Bath Temperature on the Optoelectronic Characteristics of Chemically Deposited Cds Thin-Films*. Thin Solid Films, 1988. **161**: p. 21-34.

5. Dona, J.M. and J. Herrera, *Dependence of electro-optical properties on the deposition conditions of chemical bath deposited CdS thin films*. Journal of the Electrochemical Society, 1997. **144**(11): p. 4091-4098.

6. Wenyi, L., C. Xun, C. Qiulong, and Z. Zhibin, *Influence of growth process on the structural, optical and electrical properties of CBD-CdS films*. Materials Letters, 2005. **59**(1): p. 1-5.

7. Duncan, P.C., S. Hinckley, E.A. Gluszak, and N. Dytlewski, *PIXE and RBS investigation of growth phases of ultra-thin chemical bath deposited CdS films*. Nuclear Instruments & Methods in Physics Research Section B- Beam Interactions with Materials and Atoms, 2002. **190**: p. 615-619.

8. Prabahar, S. and M. Dhanam, *CdS thin films from two different chemical baths--structural and optical analysis*. Journal of Crystal Growth, 2005. **285**(1-2): p. 41-48.

9. Boyle, D.S., P. O'Brien, D.J. Otway, and O. Robbe, *Novel approach to the deposition of CdS by chemical bath deposition: the deposition of crystalline*

thin films of CdS from acidic baths. Journal of Materials Chemistry, 1999. **9**(3): p. 725-729.

10. Altosaar, M., K. Ernits, J. Krustok, T. Varema, J. Raudoja, and E. Mellikov, *Comparison of CdS films deposited from chemical baths containing different doping impurities.* Thin Solid Films, 2005. **480-481**: p. 147-150.

11. Guillen, C., M.A. Martinez, and J. Herrero, *Accurate control of thin film CdS growth process by adjusting the chemical bath deposition parameters.* Thin Solid Films, 1998. **335**(1-2): p. 37-42.

12. Martinez, M.A., C. Guillen, and J. Herrero, *Morphological and structural studies of CBD-CdS thin films by microscopy and diffraction techniques.* Applied Surface Science, 1998. **136**(1-2): p. 8-16.

13. Jadhav, U.S., S.S. Kale, and C.D. Lokhande, *Effect of Cd:S ratio on the photoconducting properties of chemically deposited CdS films.* Materials Chemistry and Physics, 2001. **69**(1-3): p. 125-132.

14. Ortuno-Lopez, M.B., M. Sotelo-Lerma, A. Mendoza-Galvan, and R. Ramirez-Bon, *Chemically deposited CdS films in an ammonia-free cadmium-sodium citrate system.* Thin Solid Films, 2004. **457**(2): p. 278-284.

15. Nemec, P., I. Nemec, P. Nahalkova, Y. Nemcova, F. Trojanek, and P. Maly, *Ammonia-free method for preparation of CdS nanocrystalline films by chemical bath deposition technique.* Thin Solid Films, 2002. **403-404**: p. 9-12.

16. Call, R.L., N.K. Jaber, K. Seshan, and J.R. Whyte, *Structural and Electronic-Properties of 3 Aqueous-Deposited Films - Cds, Cdo, Zno, for Semiconductor and Photo-Voltaic Applications.* Solar Energy Materials, 1980. **2**(3): p. 373-380.

17. Mondal, A., T.K. Chaudhuri, and P. Pramanik, *Deposition of Cadmium Chalcogenide Thin-Films by a Solution Growth Technique Using*

Triethanolamine as a Complexing Agent. Solar Energy Materials, 1983. **7**(4): p. 431-438.

18. O'Brien, P. and T. Saeed, *Deposition and characterization of cadmium sulfide thin films by chemical bath deposition.* Journal of Crystal Growth, 1996. **158**(4): p. 497-504.

19. Feitosa, A.V., M.A.R. Miranda, J.M. Sasaki, and M.A. Araujo-Silva, *A new route for preparing CdS thin films by chemical bath deposition using EDTA as ligand.* Brazilian Journal of Physics, 2004. **34**(2B): p. 656-658.

20. Soundeswaran, S., O.S. Kumar, and R. Dhanasekaran, *Effect of ammonium sulphate on chemical bath deposition of US thin films.* Materials Letters, 2004. **58**(19): p. 2381-2385.

21. Zhang, H., X.Y. Ma, and D.R. Yang, *Effects of complexing agent on CdS thin films prepared by chemical bath deposition.* Materials Letters, 2004. **58**(1-2): p. 5-9.

22. Vigil, O., Y. Rodriguez, O. Zelaya-Angel, C. Vazquez-Lopez, A. Morales-Acevedo, and J.G. Vazquez-Luna, *Properties of CdS thin films chemically deposited in the presence of a magnetic field.* Thin Solid Films, 1998. **322**(1-2): p. 329-333.

23. Vigil, O., A. Arias-Carbajal, F. Cruz, G. Contreras-Puente, and O. Zelaya-Angel, *Modification of the properties of chemically deposited CdS thin films grown under magnetic field and variable growing parameters.* Materials Research Bulletin, 2001. **36**(3-4): p. 521-530.

24. Choi, J.Y., K.-J. Kim, J.-B. Yoo, and D. Kim, *Properties of cadmium sulfide thin films deposited by chemical bath deposition with ultrasonication.* Solar Energy, 1998. **64**(1-3): p. 41-47.

25. Zhu, Y., *Polycrystalline CdS thin films deposited by chemical bath deposition*, in *Colorado School of Mines*. 1997, Colorado: Colorado. p. 129.

26. Sasikala, G., P. Thilakan, and C. Subramanian, *Modification in the chemical bath deposition apparatus, growth and characterization of CdS semiconducting thin films for photovoltaic applications*. Solar Energy Materials and Solar Cells, 2000. **62**(3): p. 275-293.

27. Boyle, D.S., A. Bayer, M.R. Heinrich, O. Robbe, and P. O'Brien, *Novel approach to the chemical bath deposition of chalcogenide semiconductors*. Thin Solid Films, 2000. **361-362**: p. 150-154.

28. Archbold, M.D., D.P. Halliday, K. Durose, T.P.A. Hase, D.S. Boyle, and K. Govender. *Characterization of thin film cadmium sulfide grown using a modified chemical bath deposition process*. in *31st IEEE Photovoltaics Conference*. 2005. Florida, USA.

29. Archbold, M.D., D.P. Halliday, K. Durose, T.P.A. Hase, D.S. Boyle, S. Mazzamuto, N. Romeo, and A. Bosio, *Development of low temperature approaches to device quality CdS: A modified geometry for solution growth of thin films and their characterisation*. Thin Solid Films, 2007. **515**(5): p. 2954-2957.

30. Bayer, A., D.S. Boyle, M.R. Heinrich, P. O'Brien, D.J. Otway, and O. Robbe, *Developing environmentally benign routes for semiconductor synthesis: improved approaches to the solution deposition of cadmium sulfide for solar cell applications*. Green Chemistry, 2000. **2**(2): p. 79-85.

31. Enriquez, J.P. and X. Mathew, *Influence of the thickness on structural, optical and electrical properties of chemical bath deposited CdS thin films*. Solar Energy Materials and Solar Cells, 2003. **76**(3): p. 313-322.

6. CdS post-growth treatments and alternate growth methods

6.1. Introduction

In this section the structural, optical, electrical and chemical properties of four types of CdS films are investigated. Firstly the results of an annealing treatment study performed on standard SD grown films are presented, this is then followed by an investigation into SD CdS films which have been doped *in-situ* with electrically active species. Results from CSS grown CdS films are presented and finally work on two types of novel bi-layer 'hybrid' CSS and SD grown films are presented.

6.2. Annealed SD films

During the fabrication of CdS/CdTe PV devices it is common practice to anneal the CdS layer, particularly if it is grown by a low temperature method such as SD, often in the presence of $CdCl_2$ prior to CdTe deposition; it is therefore essential to understand how this treatment affects the properties of thin film SD grown CdS. In the following study films were grown on both FTO (Pilkington) and ITO (Merck) substrates, eight sample types were produced, Table 6.1 shows the processing steps used in each. They have been categorised into three groups, the reason for which will become apparent as the characteristics of each are explained in detail.

Sample	Treatment	Group
A	None	1
B	80 nm $CdCl_2$	
C	N_2 anneal	2
D	H_2 anneal	
E	Air anneal	
F	80 nm $CdCl_2$ + N_2 anneal	3
G	80 nm $CdCl_2$ + H_2 anneal	
H	80 nm $CdCl_2$ + Air anneal	

Table 6.1. CdS sample types by treatment used in this study.

Group 1 samples (A and B) were not annealed (B is essentially a control, the purpose of which was to verify that the $CdCl_2$ evaporation process itself did not affect the sample), group 2 samples (C, D and E) were annealed with no $CdCl_2$ coating whereas group 3 samples (F, G and H) were coated with an 80 nm evaporated layer of $CdCl_2$ before being annealed. Where applicable the annealing step was performed in a quartz tube furnace at 400°C for 20 minutes. The ambient atmosphere was either air, nitrogen or 4% hydrogen (96% nitrogen), after annealing each $CdCl_2$ coated sample (including sample B) was washed in methanol in order to remove any remaining $CdCl_2$. It was found that by applying treatment H the CdS layer was delaminated from the substrate, this processing step was attempted several times with the same result and the phenomena is currently being studied, however in the following work results from H-type samples will not be discussed.

6.2.1. Structural

6.2.1.1. SEM

Figure 6.1 shows SEM images of sample types A, C and F grown on FTO substrates (with a bare FTO substrate for comparison), corresponding to sample groups 1, 2 and 3. Results from other films are not shown as there was found to be no noticeable difference between films belonging to each group.

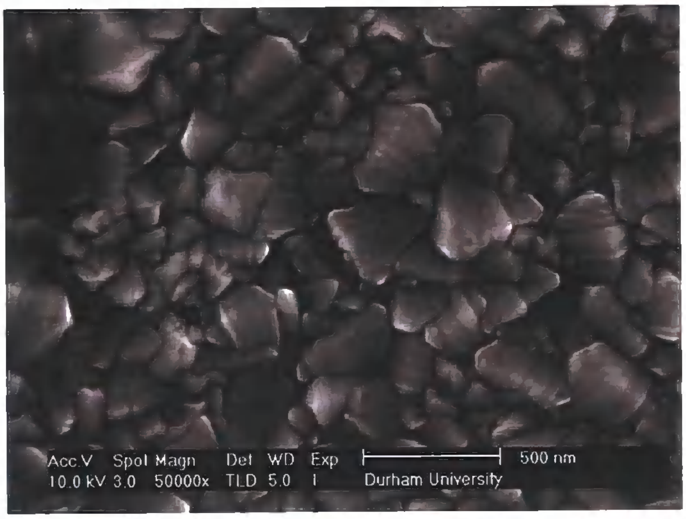

a)

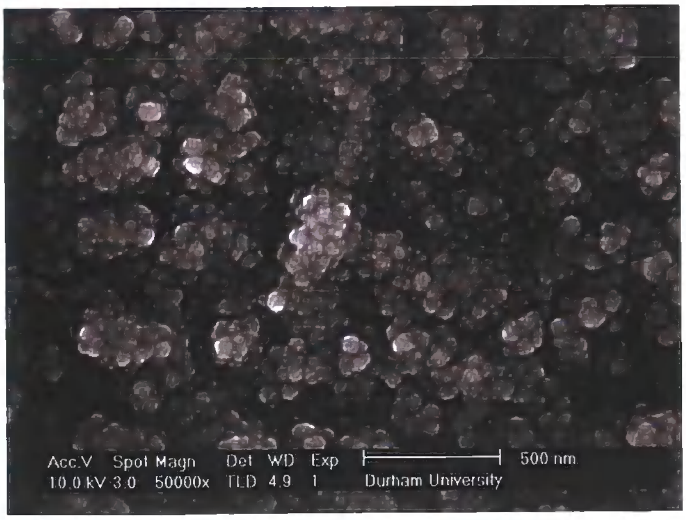

b)

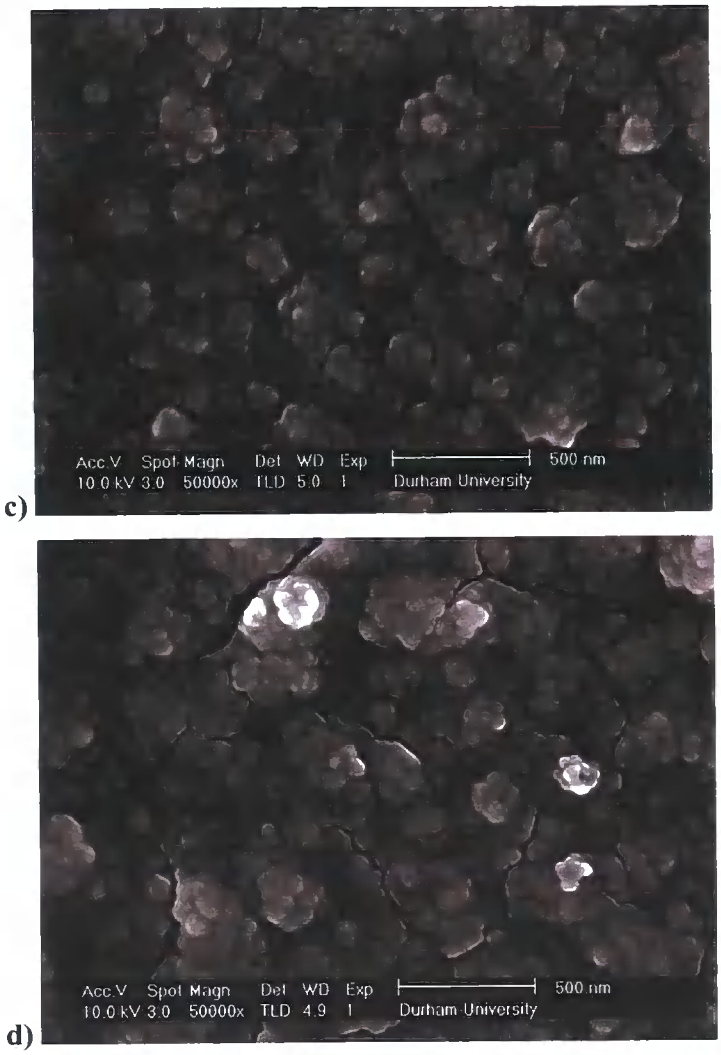

Figure 6.1. SEM images of a) a bare FTO substrate, b) a group 1 CdS film (A), c) a group 2 CdS film (C) and d) a group 3 CdS film (F).

It is apparent that there are considerable changes in morphology due to the applied annealing treatments. In group 2 films (C, D and E) the surface appears marginally more uniform than those of group 1, this suggests that the grains or crystallites are agglomerating to form a smoother top layer. It is also noticeable that small fissures have appeared on the sample surface, it is speculated that this is due to the presence of strain within the as-grown film and subsequent release of this strain upon annealing, this hypothesis is supported by GIXRD results presented later in section 6.2.1.2. In group 3 films (F and G) the effects are more pronounced, there is again evidence of crystallite agglomeration, but in this case the crystallites appear to be infilling into the larger features of the TCO substrate, suggesting that there is significant recrystallisation occurring. There is also the presence of even larger fissures, again it is hypothesised that the presence of these is due to the reduction in strain caused by the annealing treatment.

6.2.1.2. GIXRD

GIXRD scans of all CdS films grown on ITO substrates, with a substrate for comparison, are shown in Figure 6.2. In group 1 films (A and B) one clear peak can be distinguished at 27.08°, this can be assigned to either the CdS hexagonal (h) (002) or the cubic (c) (1 1 1) reflection, and a second considerably smaller shoulder at 28.87° which is assigned to the h(101) peak. From these data it is not possible to determine whether the film is present in the thermodynamically stable hexagonal phase, metastable cubic phase, a mixture of these phases or a polytype [1], nevertheless it is possible to conclude that the film is highly textured in either the [002] direction if in the hexagonal modification or the [1 1 1] direction if in the cubic modification. With only two diffraction peaks, it is not possible to distinguish between grain size and strain within the film using a Williamson-Hall plot, therefore the Scherrer formula was applied to the main h(002)/c(1 1 1) peak with the assumption that all of the peak broadening is due to particle size alone. Using this assumption the grain size was found to be 15 nm and 11 nm for A and B-type films respectively (refer to Table 6.2). It is also noticeable that the position of both these peaks in these films are shifted to higher detector angles than expected for CdS (it was first verified that the ITO peaks were not shifted from their expected positions in order to exclude the possibility that there was an offset in the detector angle), indicating qualitatively that there is a considerable amount of compressive strain contained within the as-grown CdS films.

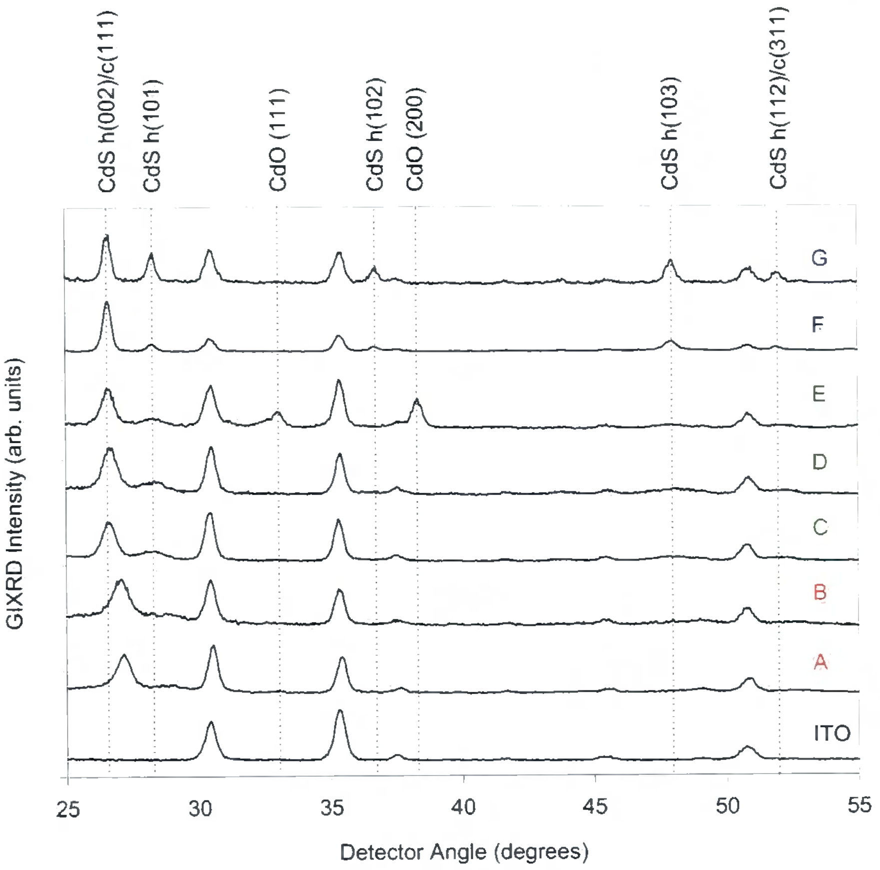

Figure 6.2. GIXRD spectra for all films in this study.

In group 2 films (C, D and E) which have been annealed without $CdCl_2$, there is a marked difference. Although there is evidence of the appearance of the hexagonal (101) peak at ~28°, this feature is broad and has a small amplitude, suggesting that although there has been some recrystallisation the film it is still textured in either the h[002] or c[111] direction. This is further evidenced by noting that there has been no significant change in the grain size (16 nm, 15 nm and 18 nm for films C, D and E respectively, from Scherrer formula calculations). Although there has been a reduction in strain (by inspection of peak positions), there is still qualitatively a moderate amount of compressive strain within the film. It is interesting to note, that the ambient gas used during annealing seems to produce little change in the crystal structure of the films, with the only exception to this being the air annealed film E, where there is clear evidence of cadmium oxide (CdO) formation. As no CdO is apparent in any other film, this is strong evidence that it is formed from the reaction of cadmium species with atmospheric oxygen rather than oxygen-containing species within the film, this confirms the findings of other authors [2]. Applying the Scherrer formula this CdO has an approximate grain size of 25 nm.

Sample	Grain Size (nm)
A	15
B	11
C	16
D	15
E	18
F	27
G	28

Table 6.2. Grain sizes for all films in this study, determined by the Scherrer formula.

In group 3 films (F and G), the h(002)/c(111) peak is found at 26.57°, the h(101) peak is clearly observed at 28.25°, the h(102) at 36.69°, the h(103) at 47.90° and a peak at 51.91° which can either be ascribed to h(112) or c(311). The existence of several clear hexagonal peaks suggests that these films are in the hexagonal phase and are polycrystalline. It is also noticeable that the main h(002)/c(111) peak has a considerably smaller width than for group 1 films, by applying the Scherrer formula to this peak the grain size was calculated to be 27 nm and 28 nm for F and G-type films respectively, inferring there has been considerable grain growth upon $CdCl_2$ annealing. It is also noticeable that the main h(002)/c(111) peak has been shifted close to its expected position, indicating qualitatively that the $CdCl_2$ anneal has significantly reduced the level of compressive strain within the film. Taken as a whole this evidence suggests that a complete recrystallisation has occurred in the $CdCl_2$ annealed films. Additionally, the Scherrer relation can also be applied to the bare substrate to calculate the ITO grain size; this was found to be 20 nm, of similar order to the grain sizes of all CdS layers.

6.2.2. Optical

6.2.2.1. Transmission

Optical transmittance spectra for all films are shown in Figure 6.3. As expected, for all films there is a reduction in transmission level at the bandgap value (E_g), this is a weak feature as the film is relatively thin, which also accounts for the high transmission (~ 60%) at energies above E_g. Table 6.3 shows the bandgap values for all films.

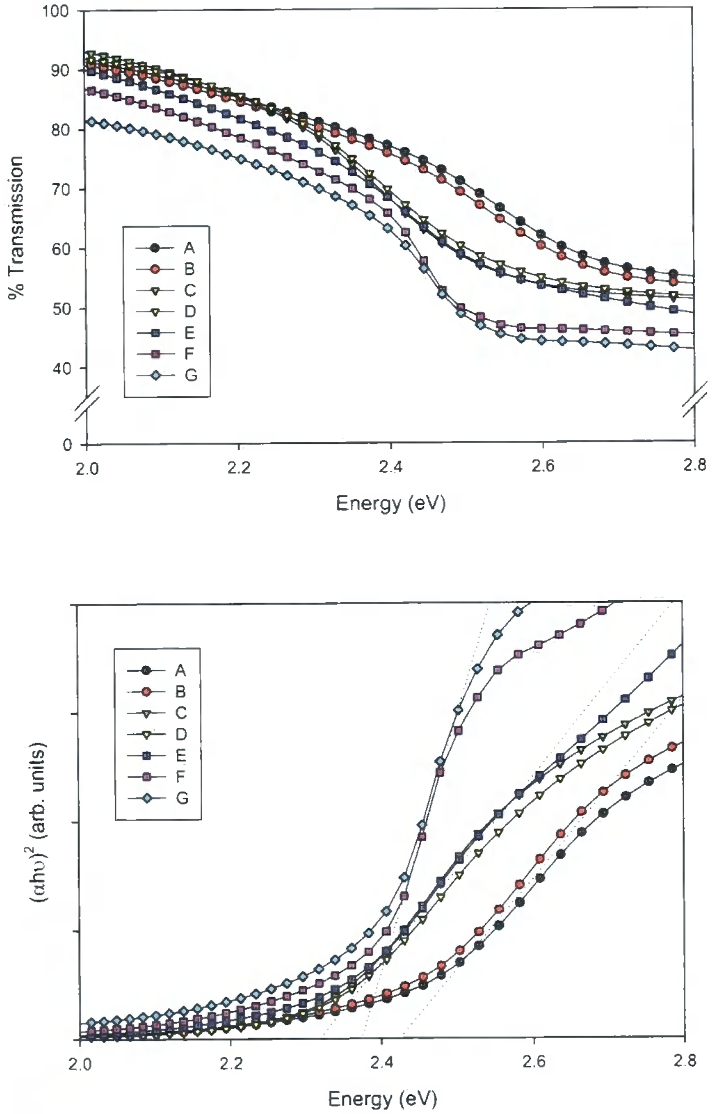

Figure 6.3. Transmission spectra for all films.

It is proposed that these changes in bandgap are a direct consequence of the partial recrystallisation to the polycrystalline hexagonal phase in group 2 films and a full recrystallisation in group 3 films; this is in accordance with x-ray diffraction data and also evidence from other authors [3-7]. It is also noticeable that the annealing atmosphere does not appear to affect the bandgap value of the films, and in particular the presence of CdO in film E does not have any perceptible effect.

Sample	**E_g (eV ±0.01)**
A	2.43
B	2.42
C	2.32
D	2.32
E	2.32
F	2.38
G	2.37

Table 6.3. Bandgap values for all films.

6.2.3. Electrical

6.2.3.1. EEA

Electrolyte electro-absorbance spectra for samples A, C and F corresponding to groups 1-3 respectively are shown in Figure 6.4. These have been fitted with the model of Aspnes [8] from which it is possible to extract the bandgap value and the broadening parameter (Γ) which is directly related to the crystalline quality of the films (refer to section 4.2.3.7).

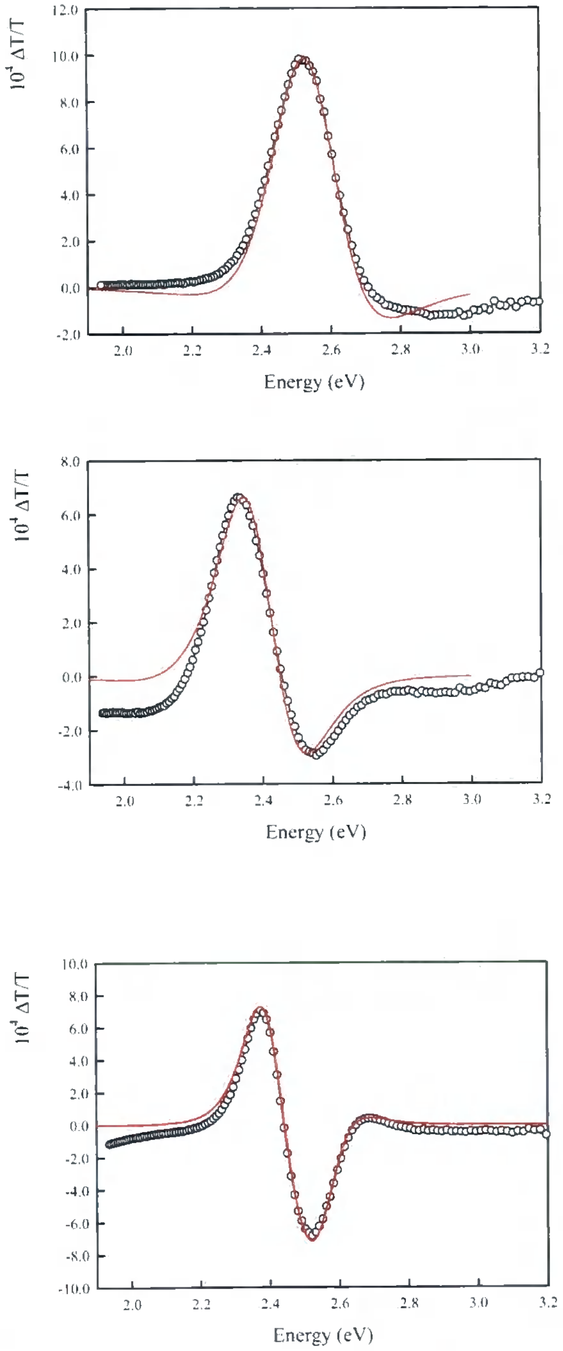

Figure 6.4. EEA spectra for a) sample A (group 1), b) sample C (group 2) and c) sample F (group 3).

From these data it is possible to conclude that a significant change has occurred in the film properties upon annealing. In group 1 films the curve comprises one peak centred at around 2.4-2.6 eV, when fitted this results in a broadening parameter Γ of 206 meV and a bandgap of 2.58 eV. This bandgap value is considerably larger than that observed by optical transmission results, however it must be noted that given the large peak width in the EEA data it is likely that the errors in this data set are more significant than for optical transmission results. In group 2 films the spectra have the same general lineshape, however the curve has been shifted to lower energies, indicating a reduction in bandgap (2.40 eV). The broadening parameter Γ has also increased slightly (220 meV) which suggests a small decrease in crystalline quality, both these findings are in agreement with the work of other authors [9]. For group 3 films the curve has changed considerably to a double peak, when fitted the calculated bandgap is found to be shifted to 2.42 eV, smaller than that observed in group 2 films and consistent with results obtained by optical transmission, bearing in mind that EEA bandgap values are in this instance higher than those obtained by optical transmission. Another effect seen in group 3 films is the large reduction in the gamma parameter (140 meV), this indicates there has been a significant improvement in crystalline quality upon $CdCl_2$ annealing. Table 6.4 shows the bandgap and gamma parameters for films A, C and F. Again these data are consistent with the work of other authors [9].

Sample	**Γ (meV)**	**E_g (eV)**
A (Group 1)	206	2.58
C (Group 2)	220	2.40
F (Group 3)	140	2.42

Table 6.4. Broadening parameter and bandgap values by the EEA technique for films A, C and F.

6.2.3.2. Capacitance-voltage

Figure 6.5 shows a Mott-Schottky plot for a type A (group 1) CdS film grown on an FTO substrate, a rectifying electrolyte configuration was used. It was found that all other film types in this study produced similar curves.

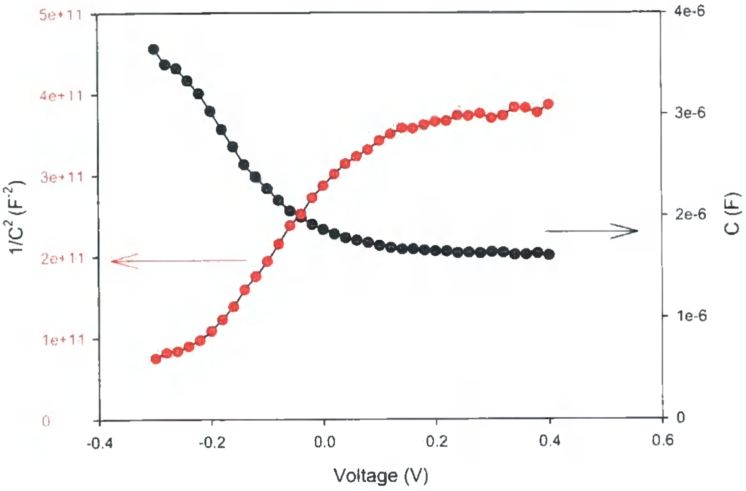

Figure 6.5. Mott-Schottky plot for a type A (group 1) CdS film.

By evaluating the gradient of the Mott-Schottky plot it was found that the donor density (the results indicate *n*-type conduction) in each case was of the order of $1\text{x}10^{20}$ cm^{-3}. This value is orders of magnitudes higher than would be expected for CdS, however it is consistent with the expected carrier density of the conductive FTO substrate (refer to section 7.2). Therefore it is concluded that either i) there are pinholes or scratches in all CdS films which allows conduction directly through to the substrate, or ii) the films are porous; work is currently being carried out to investigate this effect.

6.3. Doped SD films

In this study SD grown CdS films have been intentionally doped with electrically active species. The motivation for this work was to modify the electrical characteristics of this layer in such a way as to positively influence the properties of the CdS/CdTe junction region, and thus enhance the characteristics of these PV devices. Both *n*-type (In, B and Ag) and *p*-type (Cu) dopants were investigated, in addition to Mn for which it is not generally known whether the element is electrically active in CdS. To the authors knowledge, no study has analysed the inclusion of Mn as a dopant in polycrystalline CdS thin films.

The addition of sufficient levels of *n*-type dopant atoms into to the CdS lattice will create an n^+ type CdS film, intuitively the inclusion of such a layer into a CdS/CdTe junction would form a structure where the depletion layer has been shifted farther into the CdTe material, thus enhancing carrier collection. In addition, more conductive CdS will also result in a reduction in the series resistive losses in this layer. The motivation for the inclusion of *p*-type species is less clear. Previous studies have shown Cu inclusion into CdS/CdTe device structures to be beneficial, this is thought to be due to Cu being a quickly diffusing species in II-VI semiconductors, and therefore the Cu diffuses into the CdTe layer resulting in enhanced *p*-type doping of this region. The details of this process are however not well understood.

In this study six CdS samples were grown by the SD technique, five of these were intentionally doped by simply adding an accurately controlled volume of aqueous dopant containing solution directly to the chemical bath in order to produce a Cd:Dopant concentration of 100:1. The dopant compounds used in this study are shown in Table 6.5, these particular compounds were chosen for their ease in forming an aqueous solution and their lack of toxicity.

Dopant	**Doping Type**	**Compound**
In	n	$In_2(SO_4)_3$
B	n	H_2BO_3
Cu	p	$CuCl_2$
Ag	n	$AgNO_3$
Mn	Unknown	$MnCl_2$

Table 6.5. Dopant compounds used in this study.

It was found however that on addition of $AgNO_3$ and $MnCl_2$ to the chemical bath, a precipitate was immediately formed (brown and orange for the respective chemicals) which it is believed directly led to a greatly inhibited growth rate of CdS film on the substrate surface. Ag and Mn doped films will therefore be excluded from the following discussion. An appropriate growth time was chosen in order to produce CdS films of approximately 100 nm thickness, after deposition these thickness values were accurately measured using a surface profilometer. It was found that film thickness values could be accurately controlled (± 5 nm) for B and Cu doped films, however In doped films were typically of the order of 40 nm thick, this was repeated several times and the same outcome was found in each run. It is likely that again a change in the growth chemistry occurred, however the film was of good enough quality to perform characterisation. Films were structurally characterised using GIXRD and SEM, optically characterised by optical transmission and PL and a chemical analysis was carried out by ICP-MS.

6.3.1. Structural

Grazing incidence x-ray diffraction scans were taken for all films, however comparing these to undoped films no additional features or differences in crystallographic structure were found. This suggests that i) no other compound is formed in percentage quantities and ii) if any dopant has been incorporated into the lattice it has had no macroscopic effect on the structure of the lattice. These facts are explained by the extremely low concentration of any dopant present in the film as the dopant:Cd concentration present in the starting solution was so low; this is confirmed by ICP-MS results discussed in section 6.3.3.

SEM micrographs were taken for all films, however no difference was observed between doped and undoped films, suggesting that the nucleation process is unchanged by the presence of the dopant species. This is unsurprising for B and Cu doped films where the growth rate is unchanged, however it is an interesting result for In doped films where the growth rate has been more than halved.

6.3.2. Optical

6.3.2.1. Transmission

Figure 6.6 shows optical transmission spectra for all three films used in this study.

At energies below the bandgap region (< 2.5 eV) all films have the same general lineshape, however it is apparent that the B-doped film exhibits a marginally higher transmission value, the source of this characteristic is not known and is suggested as a topic for further study. At energies greater than the bandgap the In doped film has a much reduced transmission level as would be expected for a much thinner film, this is due to incomplete absorption.

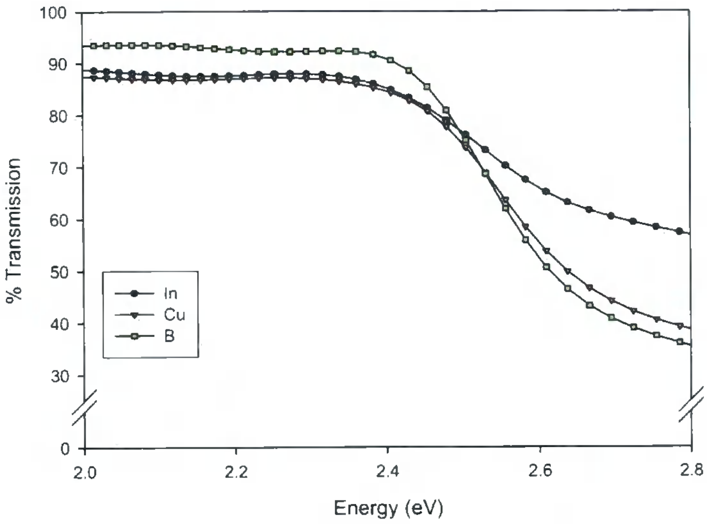

Figure 6.6. Optical transmission spectra for In, B and Cu doped CdS films.

The bandgap values for the three doped CdS films are shown in table 6.6. B and Cu doped CdS samples exhibit a bandgap of 2.52 eV significantly larger than that of undoped material (2.42 eV) whilst the In doped sample possesses a significantly lower bandgap of 2.46 eV. It has already been shown that the bandgaps of CdS films are not dependent on their thickness (section 5.5.5.1) therefore this must be due to some other aspect of film structure; this attribute is suggested as an area for future study.

Dopant	**E_g ($eV \pm 0.01$)**
In	2.46
B	2.52
Cu	2.52

Table 6.6. Bandgap values for all three films used in this study.

6.3.2.2. PL

PL scans were taken for all films at 3 K, it was found however that there was no discernable difference between samples, Figure 6.7 shows a PL spectra for a Cu doped film.

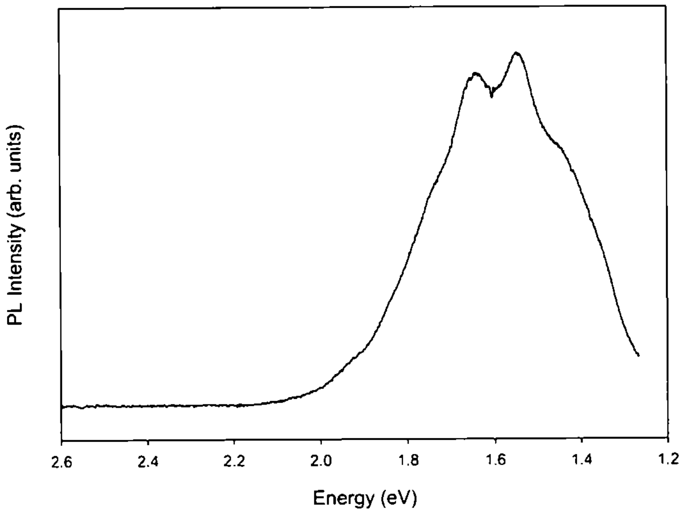

Figure 6.7. A photoluminescence spectrum of a Cu doped CdS film taken at 3K.

All samples exhibited the broad luminescence feature located at around 1.2-2.0 eV, this is typical for SD grown CdS and is referred to as the *red band*. The red band is commonly ascribed to either sulphur vacancy states [10] or surface states [11].

6.3.3. ICP-MS impurity analysis

The ICP-MS technique was employed in order to assess the extent to which intentional dopant atoms were incorporated into the grown CdS films. It is important to note however that although this gives information on the presence of the species, it does not give any information on whether the dopant has been incorporated into the lattice proper forming an electrically active centre, for example in a substitutional or interstitial position, or whether the dopant resides in a non-electrically active position, for example in a cluster in either elemental or compound form.

Table 6.7 shows dopant species incorporation data for both Cu and In. Data for Boron is not available as the ICP-MS technique is insensitive to this element (as discussed in section 4.2.2.5).

Element	**Number density (cm^{-3})**	**Dopant:Cd ratio**
Cu	3.73×10^{19}	1.87×10^{-3}
In	3.23×10^{19}	1.62×10^{-3}

Table 6.7. Dopant impurity incorporation into CdS films.

Column 2 shows the number density of the dopant atoms incorporated into the grown CdS film and column 3 is the ratio of the dopant concentration to the Cd concentration (by atom) in the films.

From these data it is possible to conclude:

- Both Cu and In have been incorporated into the films
- For every Cd atom in solution incorporated approximately 20% of all dopant atoms present in solution have been incorporated in each case (18.7% and 16.2% for Cu and In respectively)
- If these dopants are incorporated as electrically active species (within the crystal lattice proper) then as a consequence these very high doping levels would considerably alter the electrical properties of the CdS layer.

6.4. CSS and SD hybrid films

In this section work is presented on two types of CdS layer, i) films grown solely by the CSS technique and ii) those grown by a novel 'hybrid' approach involving both CSS and SD growth methods. To the authors knowledge this hybrid method is novel and has not been reported elsewhere.

The motivation for investigating hybrid CdS films is to combine the properties of SD and CSS CdS films with the anticipation that the resulting properties will be advantageous to PV device performance. SD films generally give excellent substrate coverage with no pinholes on account of their small adherent grains, whilst CSS films generally possess relatively large well defined polycrystalline grains (of the order of hundreds of nm) with excellent crystallinity and little strain [12].

The two types of hybrid films are shown in figure 6.8, H1 films consist of a 300 nm thick CSS CdS layer followed by a 100 nm SD layer, whilst type H2 films have first[13] had a 100 nm thick SD CdS layer applied, followed by a 300 nm CSS layer.

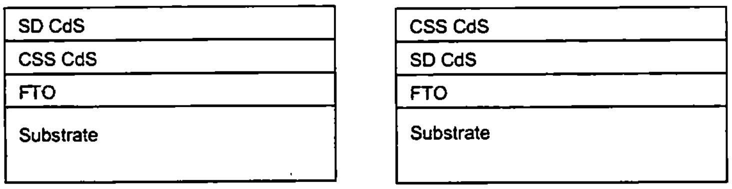

Figure 6.8. Type H1 and H2 hybrid CdS films.

The three film types have been characterised by SEM and optical transmission.

6.4.1. Structural

6.4.1.1. SEM

SEM images of CSS films and hybrid type H1 and H2 films are shown in Figure 6.9. As expected the CSS film possesses a much different grain structure to the SD films discussed earlier, this is likely due to the nature of the high temperature nucleation process [13]. The grains are much larger, of the order of 200 nm, and are regularly shaped with sharp facets. It is also apparent that within the film there are small fissures present between grains. If this is compared to type H1 films (CSS/SD) there is a noticeable difference, although there is still evidence of grain regularity (this is especially noticeable if compared to standard SD grown films) the surface grain size is noticeably smaller, of the order of 100 nm. It appears as if the SD CdS has grown conformally on the underlying CSS CdS crystal structure. In the case of H2 films (SD/CSS), the surface appearance is rather surprising in that the surface morphology resembles SD CdS rather that CSS CdS. This implies that the underlying SD CdS influences the nucleation of CSS CdS to a high degree. This interesting effect is an ideal topic for further study.

a)

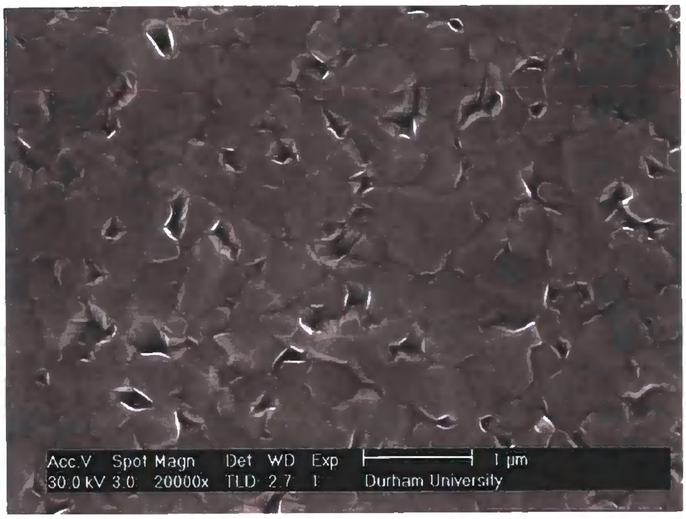
Acc.V Spot Magn Det WD Exp
30.0 kV 3.0 20000x TLD 2.7 1
1 µm
Durham University

b)

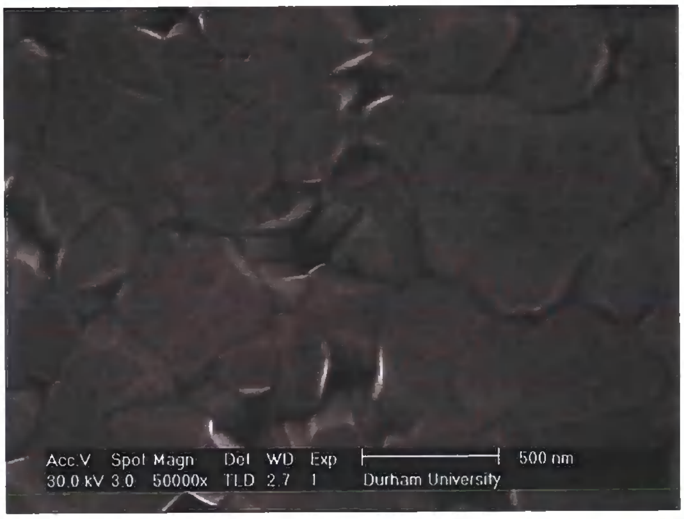
Acc.V Spot Magn Det WD Exp
30.0 kV 3.0 50000x TLD 2.7 1
500 nm
Durham University

c)

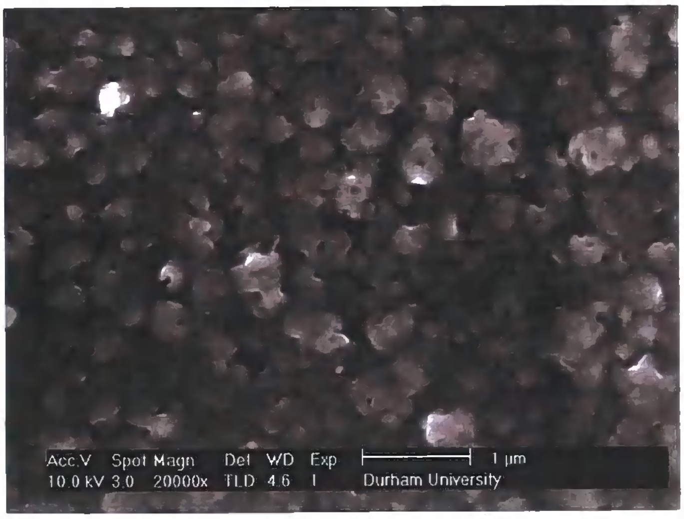
Acc.V Spot Magn Det WD Exp
10.0 kV 3.0 20000x TLD 4.6 1
1 µm
Durham University

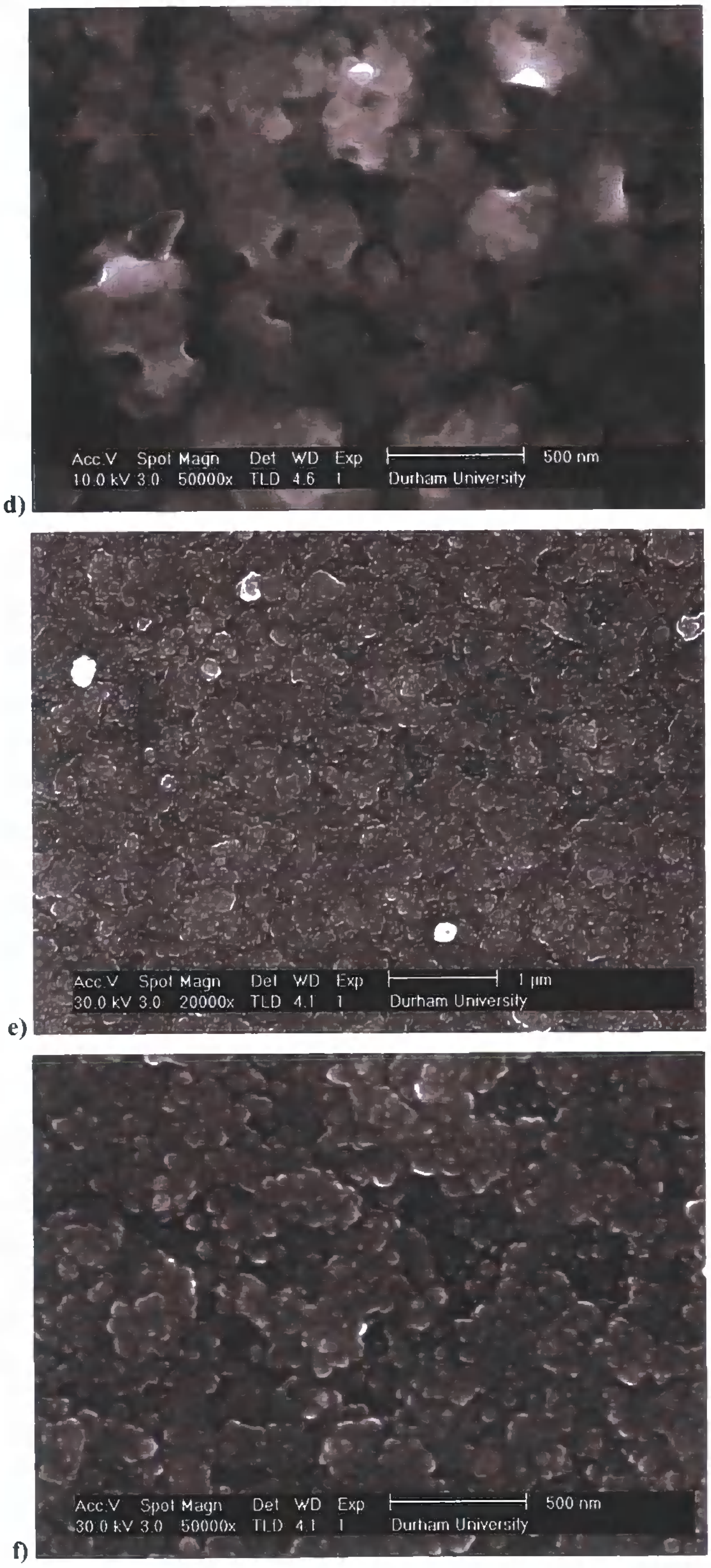

Figure 6.9. SEM images of a) CSS film at 20 k magnification, b) CSS film at 50 k, c) H1 (CSS/SD) at 20 k, d) H1 (CSS/SD) at 50 k, e) H2 (SD/CSS) at 20 k and f) H2 (SD/CSS) at 50 k.

6.4.2. Optical

6.4.2.1. Transmission

Optical transmission spectra of CSS films and hybrid type H1 and H2 films are shown in Figure 6.10, with an SD grown film for comparison. It is apparent that H1, H2 and CSS films possess similar transmission spectra, these are very different to the example SD film in that the rate of transmission cut-off at the bandgap region is much sharper (the gradient is steeper) than that of SD films, indicating that the films containing CdS grown at high temperature possess less trapping states near the band edge regions. It is also notable that this is also true for the $CdCl_2$ annealed films presented in section 6.2.2.1.

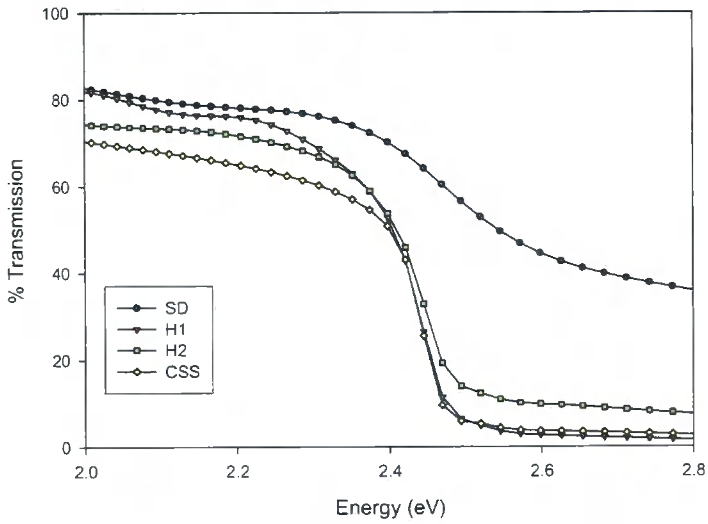

Figure 6.10. Transmission spectra for all films.

Table 6.8 shows bandgap values for all films, H1, H2 and CSS films all possess the same bandgap (2.43-2.44 eV) to within experimental error.

Film	**E_g (eV ± 0.01)**
SD	2.42
CSS	2.44
H1	2.44
H2	2.43

Table 6.8. Bandgap values for all films.

In chapter 7 CdS/CdTe photovoltaic devices are fabricated using the four growth methods presented above, SD, CSS, H1 and H1; the IV and spectral response characteristics are then compared.

6.5. References

1. Gibson, P.N., M.E. Ozsan, D. Lincot, P. Cowache, and D. Summa, *Modelling of the structure of CdS thin films*. Thin Solid Films, 2000. **361**: p. 34-40.

2. Nair, P.K., O. Gomez Daza, A. Arias-Carbajal Readigos, J. Campos, and M.T.S. Nair, *Formation of conductive CdO layer on CdS thin films during air heating*. Semiconductor Science and Technology, 2001. **16**(2001): p. 651-656.

3. Zelaya-Angel, O., A.E. Esparza-Garcia, C. Falcony, R. Lozada-Morales, and R. Ramirez-Bon, *Photoluminescence effects associated with thermally induced crystalline structure changes in CdS films*. Solid State Communications, 1995. **94**(1): p. 81-85.

4. Zelaya-Angel, O., L. Hernandez, O. de Melo, J. Alvarado-Gil, R. Lozada-Morales, C. Falcony, H. Vargas, and R. Ramirez-Bon, *Band-gap shift in CdS: phase transition from cubic to hexagonal on thermal annealing*. Vacuum, 1995. **46**(8-10): p. 1083-1085.

5. Lozada-Morales, R., M. Rubin-Falfan, O. Zelaya-Angel, and R. Ramirez-Bon, *Characterization of cubic CdS thin films annealed in vacuum*. Journal of Physics and Chemistry of Solids, 1998. **59**(9): p. 1393-1398.

6. Lozada-Morales, R. and O. Zelaya-Angel, *Photoluminescence analysis of CdS thin films under phase transition*. Thin Solid Films, 1996. **281-282**(1-2): p. 386-389.

7. Lozada-Morales, R., O. Zelaya-Angel, and G. Torres-Delgado, *Photoluminescence in cubic and hexagonal CdS films*. Applied Surface Science, 2001. **175**: p. 562-566.

8. Aspnes, D.E., *Handbook of Semiconductors*, ed. M. Balkanski. Vol. 2. 1980, Amsterdam: North-Holland. 109.

9. Ozsan, M.E., D.R. Johnson, M. Sadeghi, D. Sivapathasundaram, G. Goodlet, M.J. Furlong, L.M. Peter, and A.A. Shingleton, *Optical and electrical characterization of CdS thin films.* Journal of Materials Science-Materials in Electronics, 1996. **7**(2): p. 119-125.

10. Aguilar-Hernandez, J., G. Contreras-Puente, A. Morales-Acevedo, O. Vigil-Galan, F. Cruz-Gandarilla, J. Vidal-Larramendi, A. Escamilla-Esquivel, H. Hernandez-Contreras, M. Hesiquio-Garduno, A. Arias-Carbajal, M. Chavarria-Castaneda, and G. Arriaga-Mejia, *Photoluminescence and structural properties of cadmium sulphide thin films grown by different techniques.* Semiconductor Science and Technology, 2003. **18**(2): p. 111-114.

11. Agata, M., H. Kurase, S. Hayashi, and K. Yamamoto, *Photoluminescence spectra of gas-evaporated CdS microcrystals.* Solid State Communications, 1990. **76**(8): p. 1061-1065.

12. Albin, D., D. Rose, R. Dhere, D. Levi, L. Woods, A. Swartzlander, and P. Sheldon. *Comparison study of close-spaced sublimated and chemical bath deposited CdS films: Effects on CdTe solar cells.* in *Conference Record Of the Twenty Sixth IEEE Photovoltaic Specialists Conference.* Anaheim, CA, 29 Sep - 3 Oct 1997: IEEE.

13. Major, J.D., Y.Y. Proskuryakov, K. Durose, and S. Green, *Nucleation of CdTe thin films deposited by close-space sublimation under a nitrogen ambient.* Thin Solid Films. **In Press, Corrected Proof.**

7. CdS/CdTe devices

7.1. Introduction

In this section the results of full CdS/CdTe PV device structures are described. Three types of device are outlined, in each case the CdTe layer was grown by CSS and the growth method of the CdS layer was varied. The types of CdS layer used were i) SD (section 5.4), ii) CSS (section 6.4) and iii) hybrid films (section 6.4).

For devices described in section 7.4, the CdTe layer was deposited by the CSS method by collaborators at the University of Parma Italy according the procedure set out in [1, 2]. For all other devices (section 7.3) the CdTe was grown at Durham by CSS and following CdTe growth (8 μm thickness), the cells were $CdCl_2$ annealed using four different $CdCl_2$ thicknesses: 150 nm, 100 nm, 50 nm and 0 nm as a control. These were then NP etched and metallised with 1.5 mm diameter gold dot contacts as outlined in sections 3.3.3 and 3.3.4 and subsequently characterised by IV and spectral response. Typically on each 2.5 cm square substrate, 25 gold dot contacts were applied in five rows (1-5) of five columns (A-E), these were then labelled from top left (A1) to bottom right (E5). For each substrate the position of the gas inlet of the CSS reactor during CdTe growth (and CdS growth where appropriate) was recorded, this was done in order to ascertain whether any device trends were dependent on orientation during growth. IV curves were recorded row by row (from row 1 to row 5) and the contact to the FTO substrate was in each case made at the bottom left hand corner (near cell E5).

It should be noted that the current collection area of dot contact devices are generally underestimated due to additional current collection occurring from outside the dot contact region, therefore J_{sc} values and therefore efficiency values may be overestimated.

7.2. FTO substrate Hall measurements

All devices fabricated in section 7.3 were grown on 5x5 cm square Tec-8 FTO substrates, the electrical characteristics of these substrates were investigated using Hall effect and Van der Pauw electrical measurements. Table 7.1 shows these results, which confirm the manufacturers specification of better than 8 $\Omega\square^{-1}$ sheet resistance.

Sheet carrier density n_s (cm^{-2})	2.73×10^{16}
Bulk carrier density n (cm^{-3})	5.47×10^{20}
Hall mobility μ_h (cm^{2}v^{-1}s^{-1})	29.43
Sheet resistance Ω_s ($\Omega\square^{-1}$)	7.77

Table 7.1. Sheet carrier density (n_s), bulk carrier density (n), Hall mobility (μ_h) and sheet resistance (Ω_s) values for Pilkington Tec-8 FTO substrates.

7.3. Durham devices

7.3.1. IV results

7.3.1.1. SD CdS

Figure 7.1 shows V_{oc}, J_{sc}, FF and efficiency values for 126 PV devices utilising SD grown CdS, the green and red lines represent the mean and one standard deviation respectively, Table 7.2 shows the best, mean and standard deviation for each of these parameters. The most obvious feature of these devices, and indeed all the devices with CdTe layers and back contacts grown at Durham, is the poor efficiency values. If this is contrasted with one of only two devices in which the CdTe layer and back contact were grown at Parma (section 7.4), which possess identical CdS in some cases, this has an un-optimised efficiency of 9.80%, compared to 0-4% for several hundred devices fabricated at Durham, this is a clear indication that either the CdTe layer or the latter processing stages have not been optimised. As well as low best values, the standard deviations of all the parameters are also disappointing. If the best cell of this group is considered, the J_{sc} value, and the V_{oc} to a lesser extent are respectable, however the FF is very poor at 31.2%. This is indicative of i) a high series resistance and/or ii) a low shunt resistance (refer to sections 2.5.2.1 and 2.5.2.2). The low V_{oc} parameter indicates i) a low shunt resistance and/or ii) a high value of junction recombination (section 2.5.2.3). Taking both FF and V_{oc} parameters together suggests that a low shunt resistance is likely to be the cause of these poor quality devices, however more work needs to be done in order to understand this relationship more clearly.

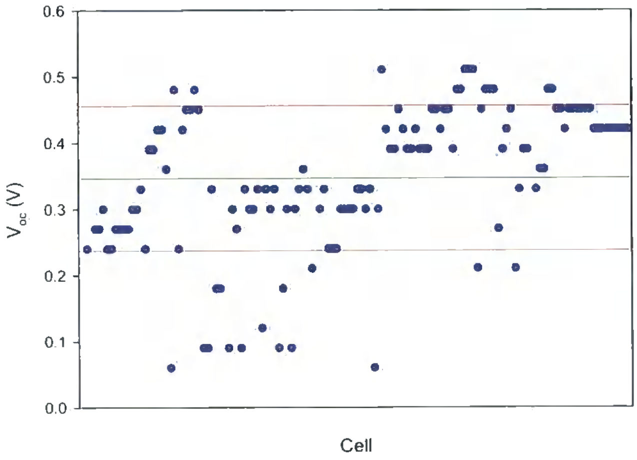

a)

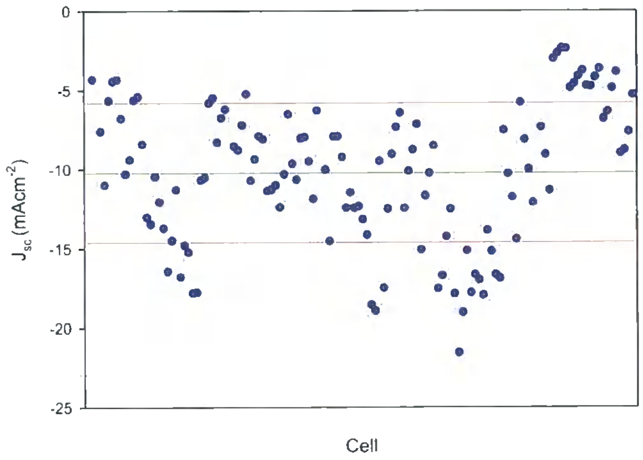

b)

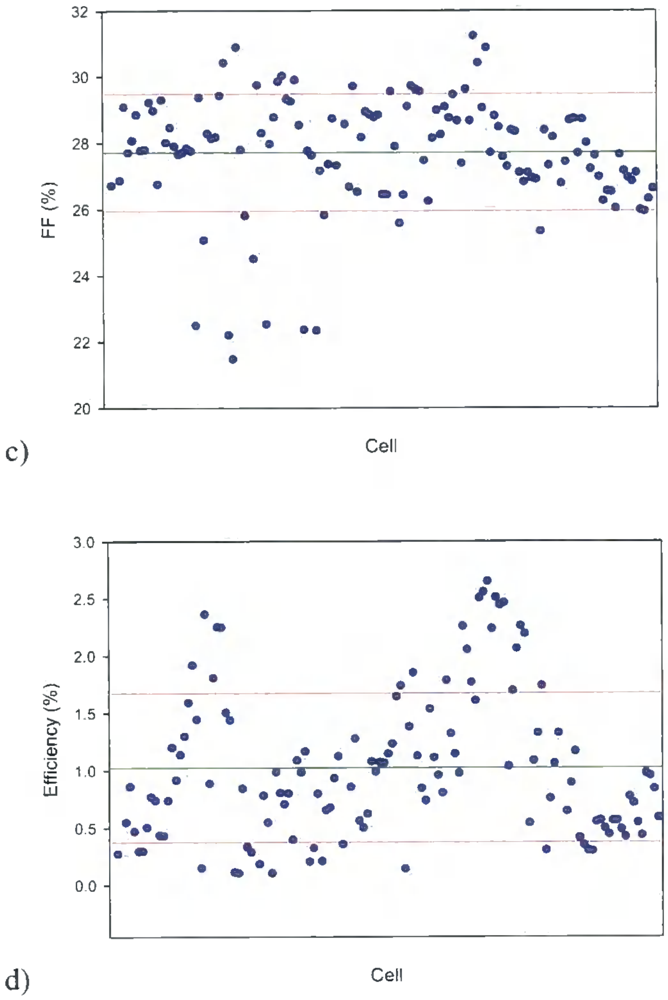

Figure 7.1. Plots of a) V_{oc}, b) J_{sc}, c) FF and d) efficiency for all 126 PV devices made with SD CdS.

	J_{sc} (mAcm^{-2})	V_{oc} (V)	FF (%)	Efficiency (%)
Best Cell	-21.55	0.51	31.23	2.65
Mean	-10.21	0.35	27.71	1.03
Standard Deviation	4.40	0.11	1.76	0.65

Table 7.2 Best, mean and standard deviation values for the characterisation parameters of 126 SD CdS PV devices.

Figure 7.2 shows the efficiency values of each SD CdS device as a function of $CdCl_2$ layer thickness (0, 50, 100 or 150 nm). It is apparent that without a $CdCl_2$ treatment (only an anneal is performed) the efficiencies are constantly low but well grouped (low standard deviation); with the application of $CdCl_2$ the maximum efficiency is increased at the expense of larger deviations in performance. This data however is not well correlated and it is likely that there is more than one effect influencing efficiency values.

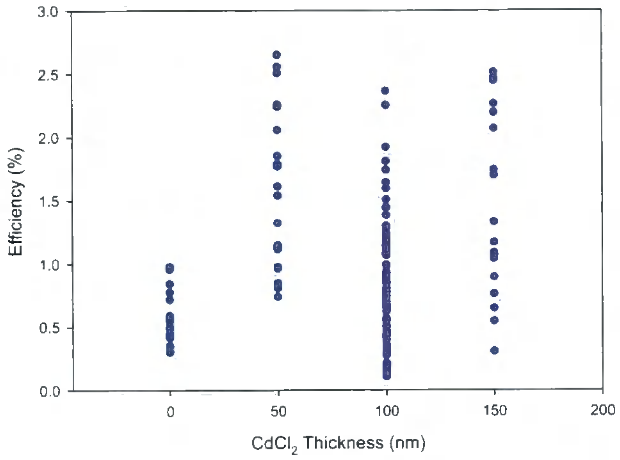

Figure 7.2. Efficiency values as a function of applied $CdCl_2$ layer thickness prior to annealing for 126 PV devices made with SD grown CdS.

7.3.1.2. CSS CdS

Figure 7.3 shows V_{oc}, J_{sc}, FF and efficiency values for 142 PV devices utilising CSS grown CdS, with Table 7.3 showing the best, mean and standard deviation for each of these parameters. These parameters are an improvement over SD grown CdS devices however the efficiencies are still poor. If the best cell of this group is considered, the J_{sc} and the V_{oc} values are respectable, however again the FF is very poor at 43.1%. This is indicative of i) high series resistance and/or ii) a low shunt resistance (refer to sections 2.5.2.1 and 2.5.2.2). Note that the best J_{sc} value (-30.31 $mAcm^{-2}$) is unphysical, it is likely that it arises from additional current collection from outside of the dot contact region.

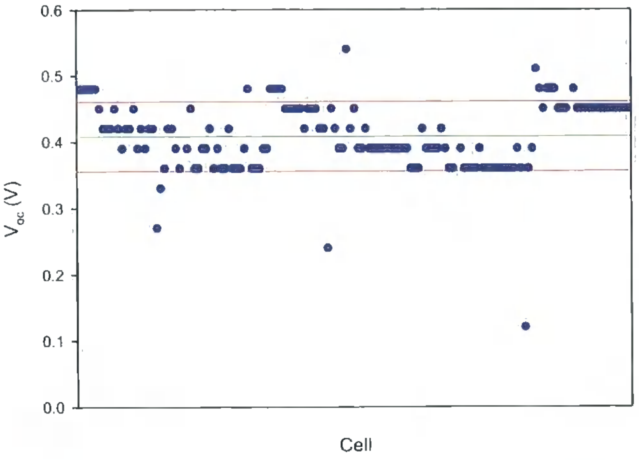
0.6
0.5
0.4
0.3
0.2
0.1
0.0
V_{oc} (V)
Cell

a)

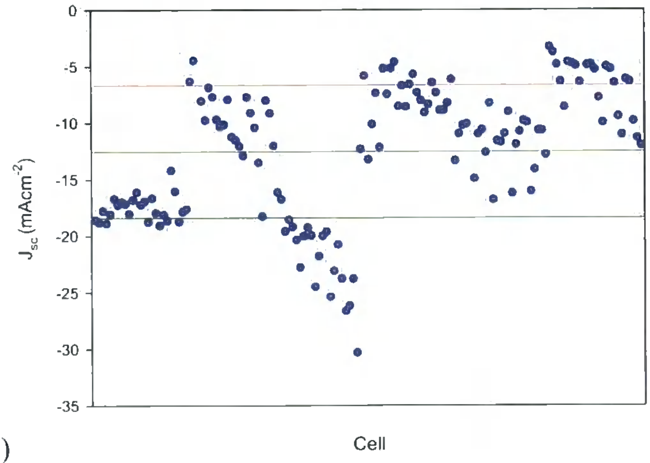
0
-5
-10
-15
-20
-25
-30
-35
J_{sc} (mAcm^{-2})
Cell

b)

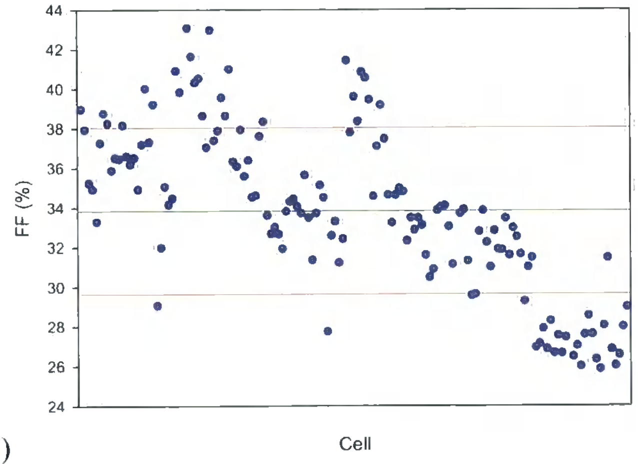
44
42
40
38
36
34
32
30
28
26
24
FF (%)
Cell

c)

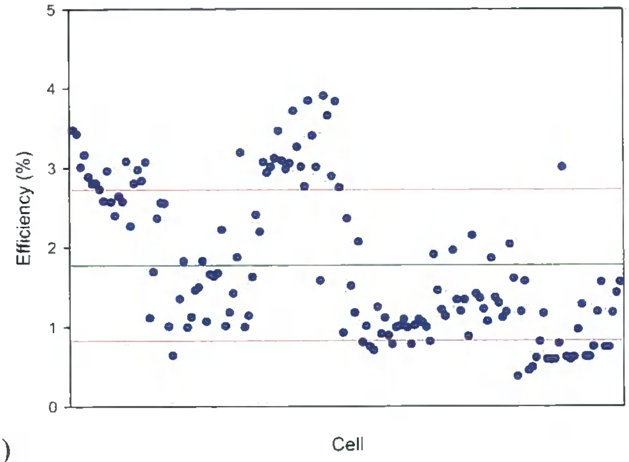

d)

Figure 7.3. Plots of a) V_{oc}, b) J_{sc}, c) FF and d) efficiency for all 142 PV devices made with CSS grown CdS.

	J_{sc} (mAcm^{-2})	V_{oc} (V)	FF (%)	Efficiency (%)
Best Cell	-30.31	0.54	43.08	3.91
Mean	-12.54	0.41	33.84	1.77
Standard Deviation	5.85	0.05	4.20	0.95

Table 7.3 Best, mean and standard deviation values for the characterisation parameters of 142 CSS CdS PV devices.

Figure 7.4 shows the effect of $CdCl_2$ annealing treatments on these films. It is apparent that once again, where no $CdCl_2$ has been applied prior to anneal, this results in low efficiency values with a low corresponding deviation. However, it is apparent that a 100 nm layer improves the efficiency by a substantial amount, more than doubling the mean untreated device efficiency value.

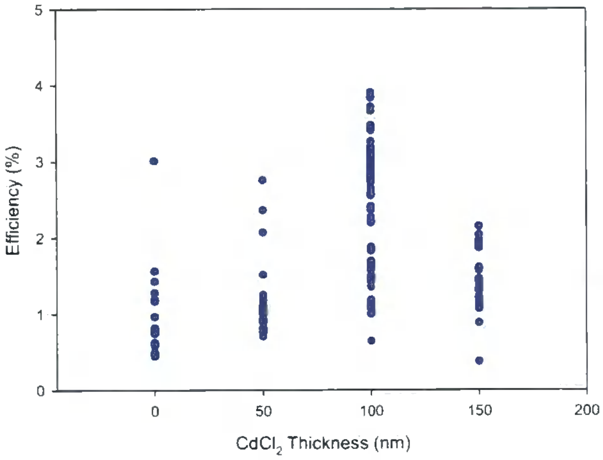

Figure 7.4. Efficiency values as a function of applied $CdCl_2$ layer thickness prior to annealing for 142 PV devices made with CSS grown CdS.

7.3.1.3. Hybrid CdS

Figure 7.5 shows V_{oc}, J_{sc}, FF and efficiency values for 101 PV devices utilising H1 grown CdS, Figure 7.6 shows corresponding data for 85 devices utilising H2 CdS. Tables 7.4 and 7.5 show the best, mean and standard deviation for each of these parameters for H1 and H2 devices respectively.

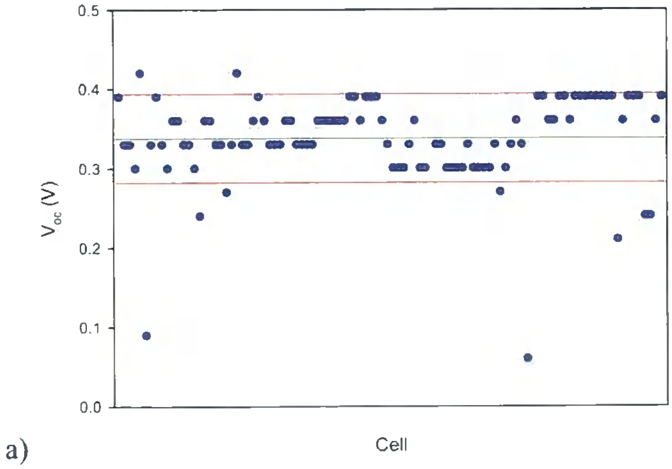

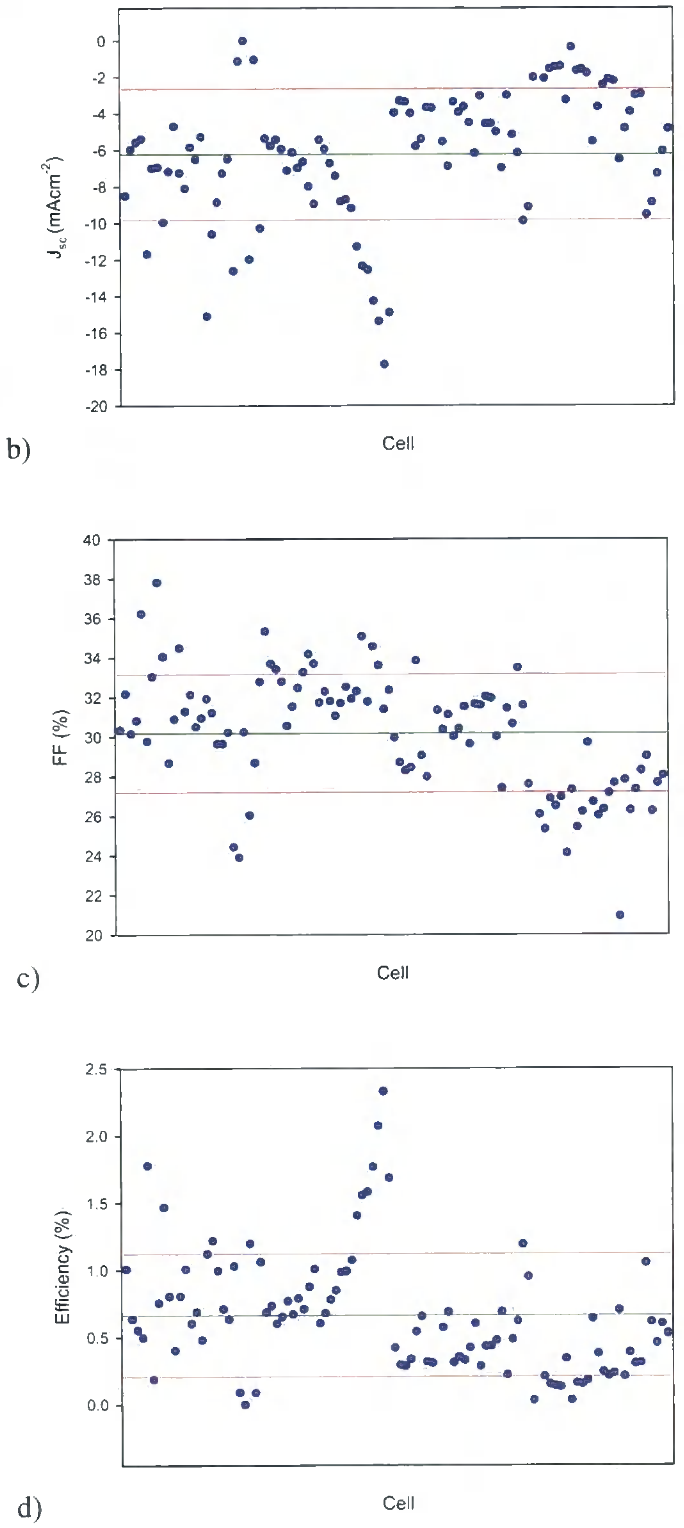

Figure 7.5. Plots of a) V_{oc}, b) J_{sc}, c) FF and d) efficiency for all 101 PV devices made with H1 type CdS.

	J_{sc} (mAcm^{-2})	V_{oc} (V)	FF (%)	Efficiency (%)
Best Cell	-17.75	0.42	37.81	2.33
Mean	-6.31	0.33	29.94	0.66
Standard Deviation	3.66	0.06	3.80	0.46

Table 7.4. Best, mean and standard deviation values for the characterisation parameters of 101 H1 CdS PV devices.

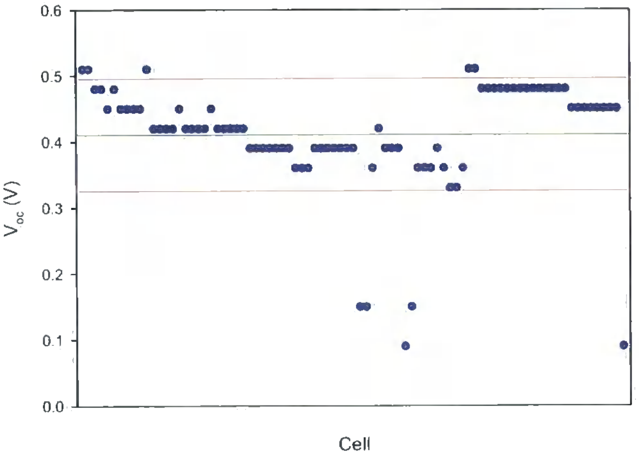

a)

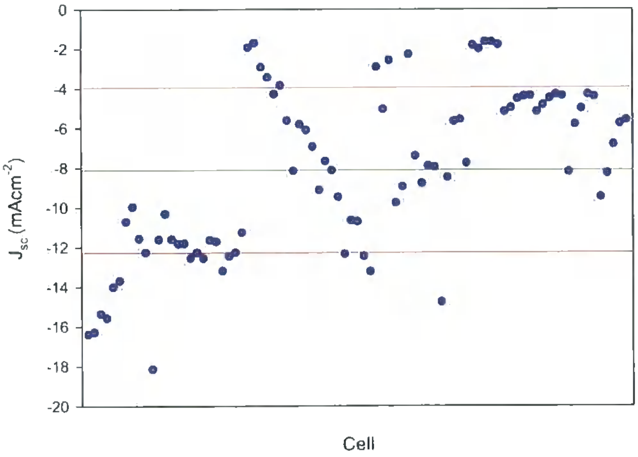

b)

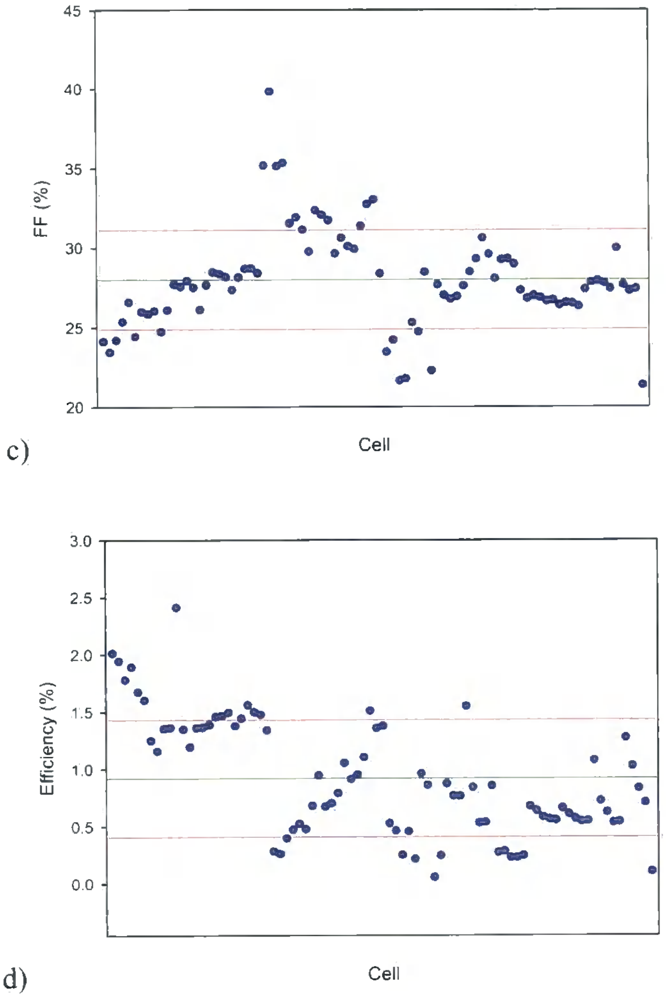

Figure 7.6. Plots of a) V_{oc}, b) J_{sc}, c) FF and d) efficiency for all 85 PV devices made with H2 type CdS.

	J_{sc} (mAcm^{-2})	V_{oc} (V)	FF (%)	Efficiency (%)
Best Cell	-18.13	0.51	39.84	2.41
Mean	-8.12	0.41	28.00	0.92
Standard Deviation	4.17	0.09	3.13	0.51

Table 7.5 Best, mean and standard deviation values for the characterisation parameters of 85 H2 CdS PV devices.

It is apparent from these data that there has been no marked improvement in device performance due to the two layer structure. H1 devices perform in a similar way to their SD CdS counterparts (low V_{oc}'s) whilst H2 films possess qualities similar to their CSS CdS counterparts (high V_{oc}'s). This suggests qualitatively that the junction between CSS CdS and CdTe is superior to that of the SD CdS/CdTe junction.

Figures 7.7 and 7.8 show the effect of $CdCl_2$ annealing treatments on these two types of hybrid devices. It is apparent that H1 devices benefit from a 50 nm $CdCl_2$ layer prior to annealing, whilst H2 devices benefit from 100 nm. Again this is in accordance with data from SD and CSS devices, showing the similarity between H1 and SD devices and H2 and CSS devices.

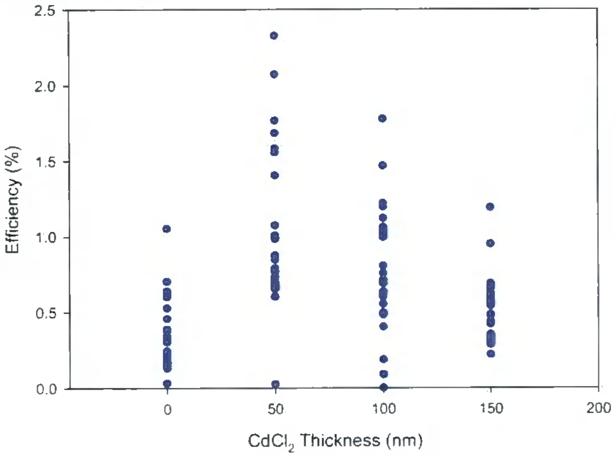

Figure 7.7. Efficiency values as a function of applied $CdCl_2$ layer thickness prior to annealing.for 101 PV devices made with H1 CdS.

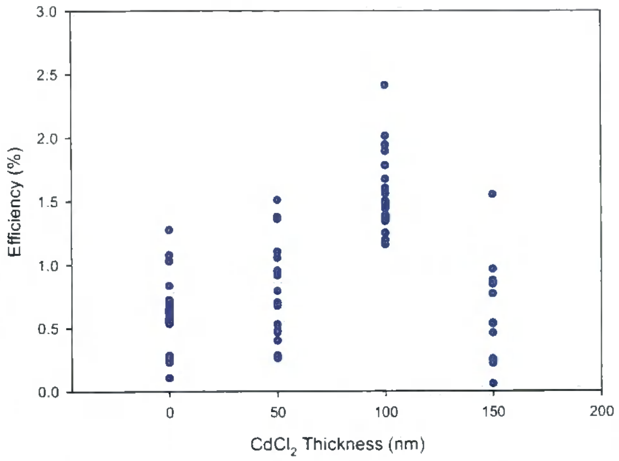

Figure 7.8. Efficiency values as a function of applied $CdCl_2$ layer thickness prior to annealing.for 85 PV devices made with H2 CdS.

7.3.2. Spectral response

Figure 7.9 shows comparative spectral response data for the four classes of device discussed above, for each device type the spectral response curves were found to be similar (although there were differences in absolute magnitude due to the differing efficiency values) and therefore a typical normalised curve for each device type is shown. The $CdCl_2$ thickness applied prior to annealing is the same (100 nm) for each device. It should first be mentioned that the feature located around 1.8 eV in each scan is likely due to an error in the calibration of the photodiode used to record the spectra, and therefore is not physical.

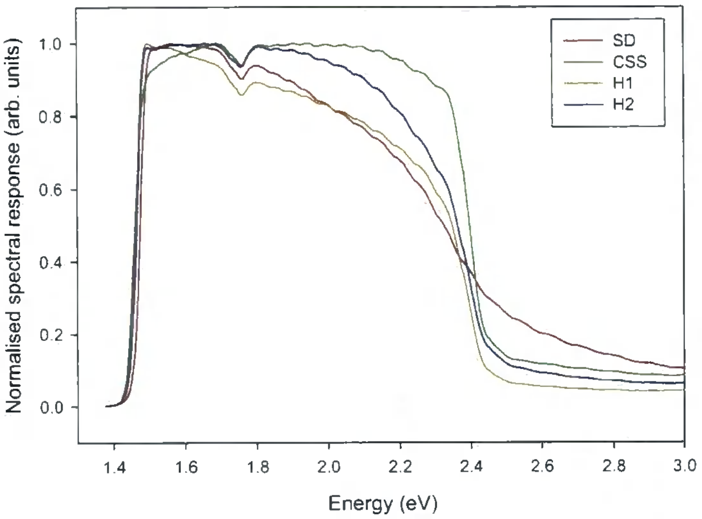

Figure 7.9. Normalised spectral response data for typical devices fabricated with four CdS types.

As expected all devices exhibit a sharp cut-off at 1.4-1.5 eV, all incident photons with energy lower than this pass through the device and are not absorbed. As this value was the same in all cases this suggests that the CdTe bandgap was approximately equal for all devices. There are clear differences between device types, however.

- In the 2.4-3.0 eV region there is a very low spectral response for CSS, H1 and H2 devices, this is consistent with complete absorption of light in this region. This is not the case for SD devices however, and therefore it is clear that a small proportion of light in this energy region is reaching the junction.
- In the 1.6-2.4 eV region, the response of the CSS device remains consistently high, suggesting respectable junction performance. This is in sharp contrast to SD grown CdS in which there is very poor spectral response in this region. This poor performance is also in evidence for H1 type films, however H2 films show better performance in this region. This again suggests that H1 devices (which have an SD CdS/CdTe junction) share similarities with SD devices and H2 devices (which possess a CSS CdS/CdTe junction) share similarities with CSS device structures.

7.4. Parma devices

Two devices were fabricated using a 100 nm thick SD grown CdS [1] layer grown at Durham and subsequent CdTe deposition (9 μm thickness) and back contact application at the University of Parma [2]. The characteristics for the best of these two devices are shown in Table 7.6.

Cell	**Area (cm^2)**	**Voc (V)**	**J_{sc} ($mAcm^{-2}$)**	**FF (%)**	**Efficiency (%)**
M116-b	0.53	0.770	16.52	0.50	9.80

Table 7.6. Device performance characteristics for a CdS/CdTe PV device.

Despite a low fill factor, this cell has a notable efficiency of 9.80%. In contrast to earlier devices the V_{oc} is excellent, and the J_{sc} value is very respectable. These data show that the likely source of cell non-performance in the devices presented in section 7.3 is due to either the CdTe layer or subsequent processing steps. This could be the important $CdCl_2$ treatment and back contact application or a complicated interaction between all these process steps. This data is good evidence that the SD method developed throughout this work has potential for the production of quality CdS/CdTe thin film photovoltaic devices.

7.5. References

1. Archbold, M.D., D.P. Halliday, K. Durose, T.P.A. Hase, D.S. Boyle, S. Mazzamuto, N. Romeo, and A. Bosio, *Development of low temperature approaches to device quality CdS: A modified geometry for solution growth of thin films and their characterisation.* Thin Solid Films, 2007. **515**(5): p. 2954-2957.

2. Romeo, N., A. Bosio, R. Tedeschi, A. Romeo, and V. Canevari, *A highly efficient and stable CdTe/CdS thin film solar cell.* Solar Energy Materials and Solar Cells, 1999. **58**(2): p. 209-218.

8. A novel geometry photovoltaic device

8.1. Introduction

In this chapter work is presented on a photovoltaic device structure which utilises an innovative geometry. The idea was first presented by Weinstein and Lee as a U.S. patent application in 1976 [1], however to the authors knowledge no material device structure has ever been demonstrated and therefore this is the first practical realisation, albeit at an early stage, of such a device. In this chapter the inspiration for this work is presented, the structure is discussed and the motivation for the work is outlined, this is followed by a description of the growth methods used and the characterisation which has been performed.

8.2. Inspiration and device structure

The inspiration for this work was the realisation that the SD technique could be carried out much more safely and effectively using a rigid structure as both a container for reactant chemicals and as a substrate. The work in this chapter outgrew this initial notion as it became apparent that there were numerous reasons why this geometry could be used to successfully realise an improved PV device.

The PV device structure described in this work is composed of a tubular transparent substrate in which the active photovoltaic layers have been grown onto the inside. The layers used in this prototype device are identical to that used in the typical flat plate geometry (TCO/CdS/CdTe), the novelty arises from the tubular geometry. Figure 8.1 shows a schematic of the device.

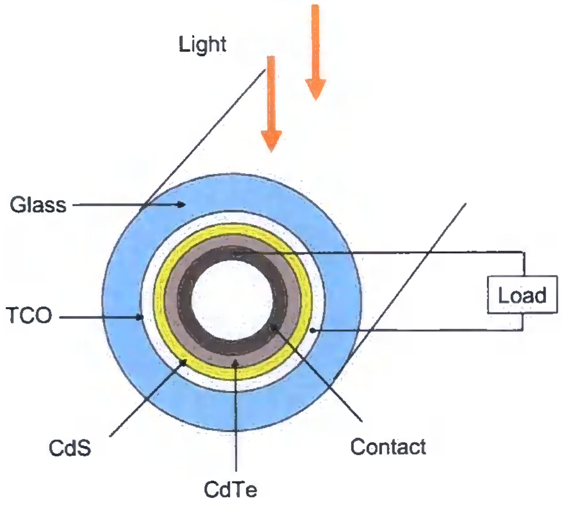

Figure 8.1. Novel tubular device structure.

As with a conventional superstrate device, light enters the glass layer, passes through the TCO and strikes the CdS/CdTe heterojunction where electron-hole pairs are created. The respective carriers are swept to each side of the junction by the built-in field and thus current is generated in an external circuit. As in a conventional design, current is extracted by contacting and providing a load between the TCO and metallic back contact layers. It is envisaged that a production PV module would be constructed by the positioning of several (~ 10-100) of these tubular cells adjacent to one another in a planar geometry (Figure 8.2) with suitable electrical connections, and a reflective material positioned behind to recycle any light that may have passed through the spaces between tubes.

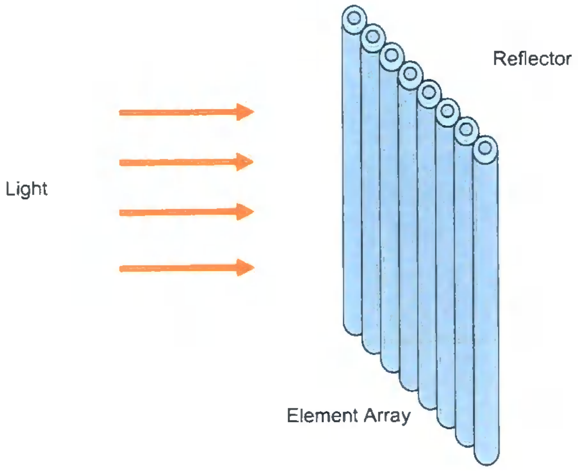

Figure 8.2. Schematic of proposed PV module structure.

Additionally this tubular structure lends itself to the exciting possibility of producing a hybrid photovoltaic and solar thermal generation system by circulating a coolant liquid through the tubular PV devices; this is discussed in section 8.3.3.

8.3. Motivation

Three main advantages that a tubular PV structure will have over conventional flat plate designs are i) reduced complexity (and hence cost saving) in the manufacturing process, ii) the possibility of efficiency gains over conventional flat plate designs and iii) the prospect of hybrid PV/solar thermal devices; these three factors are now discussed.

8.3.1. Manufacturing process

All current CdS/CdTe device manufacturing schemes rely on high temperature growth methods such as CSS or vapour transport. An alternative to this is the solution deposition method which has been detailed throughout this work. It is possible to deposit both CdS and CdTe using this method (although an electrodeposition (ED) modification must be made for CdTe) however it is not generally held to be a viable manufacturing process on a large scale due to the difficulty in confining large baths of Cd containing compounds safely. In the novel geometry described above it becomes possible to contain the growth liquids safely as the tubular substrate itself acts as a reaction vessel, confining the liquid compounds and depositing semiconductor material in one step. There are many potential benefits of this process: first the advantages due to the SD growth method are considered:

- No complicated vacuum equipment is necessary
- The growth temperature will be low by conventional growth techniques (~80°C compared to ~500°C), although some annealing steps will be required
- Solution deposition uses around 95% of the starting material, as compared to around 75% for industrial scale sublimation [2]

The advantages to the manufacturing process of utilising a tubular substrate geometry are:

- The process is self contained
- A one-step production process is possible, as well as a significant cost saving this will minimise contamination to the device during fabrication
- Less module wastage, as complete modules will only be made from fully functioning tubular cells
- The device is already partly encapsulated, it has been calculated that encapsulation and modularisation are the major cost of production PV modules [2].

Most of the points mentioned above will represent a significant cost saving. An in-depth cost analysis study performed by Zweibel [2], concluded that there is a strong economic case for using solution deposition (ED for CdTe) rather than high temperature growth techniques.

It should also be noted that other growth methods are compatible with the tubular geometry, such as MOCVD, CVD and vapour transport, indeed the TCO layer in this prototype device was produced using CVD.

8.3.2. Efficiency gains

It is envisaged that performing film growth and processing steps inside a well controlled and highly symmetric tubular structure will result in several advantageous effects on the semiconductor layers themselves. Firstly the uniformity of growth of the layers may be better controlled due to the symmetry of the growth surface, largely because of the lack of 'edge-effects'. Secondly it will be possible to control more accurately the temperature uniformity and ambient atmosphere of any annealing steps that take place. As the tubular substrates are symmetric again their will be no edge-effects, and accurately controlling the annealing gasses will be simplified as they can be injected directly into the low volume tube. Thirdly, annealing will not result in any loss of semiconductor material, this is because any material which is sublimed will be immediately re-deposited elsewhere on the tube interior. This geometry also opens up the possibility of very high temperature annealing processes (> 750°C if using a borosilicate glass substrate) that would not be possible in conventional flat plate designs.

Considering all these factors together it is highly possible that some advance in efficiency levels can be made with devices of this design.

8.3.3. PV/solar thermal hybrid devices

Solar thermal devices rely on the extraction of energy from the sun by circulating a coolant fluid over a selectively absorbing material (for example CoO, NiO or CuO). This layer absorbs infrared radiation from the sun, the coolant fluid then extracts this thermal energy and transfers it to a domestic hot water system where it is used. By integrating such a coolant system into a household PV array two benefits are realised: firstly the infrared energy that passes through typical PV devices unused is recovered and hence produces useful energy, and secondly the act of cooling a PV device increases its efficiency significantly.

This type of system has been suggested previously (although the author cannot find any example of an actual PV/solar thermal device on the market at the present time) however the reason for making the suggestion here is that the tubular geometry device outlined above lends itself perfectly to this scheme. If the PV device is sufficiently isolated (for instance by adding an inner protective layer or an additional tube, possibly made from a flexible non-reactive polymer) coolant fluid can simply be pumped through the bore of the tube. This is an exciting possibility and is suggested as a topic for future work.

8.4. Device growth

An early prototype CdS/CdTe device has been fabricated, however at the time of publication no device characterisation parameters have been measured, this data will be published at a later date. The fabrication techniques involved are described below.

8.4.1. Substrate and TCO

The TCO coated borosilicate tube was produced by growing a layer of tin oxide (SnO_2) onto a readily available glass tube. The substrate used was a 4 mm inner diameter, 6 mm outer diameter, 1 mm thick borosilicate glass (3.3 ISO 3585) tube. This was chosen as it is sufficiently tough to resist handling, has high softening and melting points (820°C and 1260°C respectively) and is also a common bore size and is therefore inexpensive. The substrate is first thoroughly cleaned by an ultrasonic treatment in Decon 90 detergent, followed by DI water, this is then followed by the application of a transparent conductive SnO_2 film of approximately 1 μm thickness. to the inner surface of the tube by chemical vapour deposition (CVD). A schematic of the CVD apparatus used is shown in Figure 8.3.

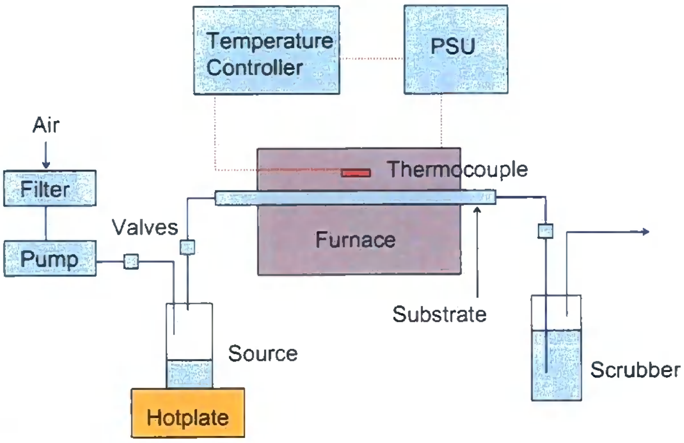

Figure 8.3. TCO deposition apparatus.

The general principle is that the source $SnCl_2$ vapour, heated to its boiling point by the hotplate, is transported to the tube at atmospheric pressure by a flow (1000 sccm) of filtered air. The tube is heated to 400-600°C by a PID controlled resistively heated tube furnace, as the $SnCl_2$ vapour passes over the hot substrate it reacts with atmospheric oxygen on the heated glass surface to form a coating of SnO_2.

$$SnCl_2 + O_2 \rightarrow SnO_2\,(s) + 2Cl\,(g) \qquad (8.1)$$

By accurately controlling the deposition time and substrate temperature, the required thickness of SnO_2 can be applied. It is important to mention that generally a dopant (typically fluorine or antimony) is added to increase conductivity of TCO films grown by this method, however this was not possible in this initial study, therefore the conductivity of the SnO_2 substrates is around two orders of magnitude lower than commercially available TCO substrates. However, this was satisfactory for this initial proof of concept study.

8.4.2. CdS

A CdS window layer was grown by a solution deposition process similar to that described in chapter 5. The difference being that instead of dipping the substrate into the heated chemical bath solution, the bath solution is instead enclosed in the tube (which has been sealed at one end) and is immersed into a beaker of heated (80°C) water as shown in Figure 8.4.

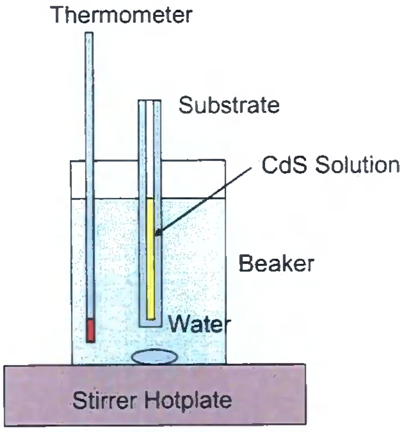

Figure 8.4. CdS deposition apparatus.

This has several advantages:

- Heat is applied to the solution inwardly from the substrate itself, therefore growth will occur directly on the substrate and not in the bulk solution. This has the consequence that less volume of solution is needed per surface area.

This idea is similar in principle to previous work presented by Boyle et al [3] and Archbold et al [4]

- The solution can be heated very rapidly to 80°C, the increased temperature ramp has the effect of increasing the rate of reaction, deposition only takes approximately one minute for a 200 nm film thickness
- The CdS solution is safely enclosed
- Significantly less liquid waste products are produced
- It is a very simple, and therefore cheap, process

8.4.3. CdTe

CdTe was deposited by electrodeposition from an acidic liquid electrolyte containing Cd^{2+} and Te^{2-} ions, for a full discussion of the growth scheme refer to Duffy et al [5-7]. Figure 8.5 shows a schematic of the growth apparatus, the TCO and CdS coated substrate (after an annealing treatment in air at 400°C for 20 minutes) was attached to the working electrode of a potentiometer and was then immersed into the electrolyte solution, a cadmium wire reference electrode and a cadmium foil counter electrode were inserted into the growth cell and a suitable potential was applied. After a growth time of 40 minutes a thin CdTe film was formed, this layer was homogeneous and approximately 100 nm thick by inspection. By increasing the growth time, CdTe layers of several microns in thickness can be grown on a timescale of 2-3 hours.

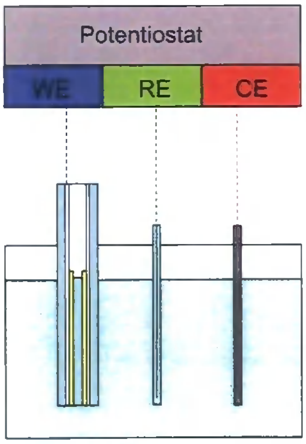

Figure 8.5. CdTe electrodeposition apparatus.

8.5. Characterisation

8.5.1. TCO

The SnO_2 films presented here were grown at a substrate temperature of 500°C for 6 minutes at a gas flow rate of 1000 sccm. These parameters were found to result in films with thicknesses of the order of 1 μm, with excellent transmission in the visible region of the spectrum and adequate electrical conductivity; both these parameters are critical for the fabrication of quality PV devices.

8.5.1.1. Optical transmission

An optical transmission spectrum for a typical SnO_2 film is shown in Figure 8.6, note that the transmission has been normalised to one as the geometry of the measurement precluded absolute transmission levels to be calculated. This exhibits a cut-off in transmission around the 3.5-4.0 eV region. The corresponding bandgap (calculated from the intersection of $(\alpha h\nu)^2$ with the energy axis, Figure 8.7) is found to be 3.96 eV, in accordance with commonly accepted literature values of 3.6-4.0 eV, dependent on the method of deposition [8].

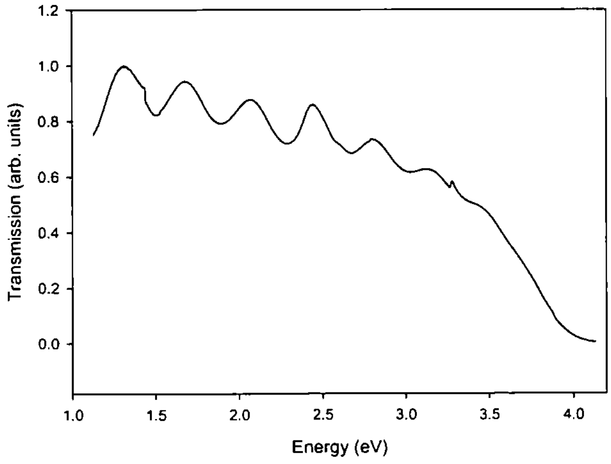

Figure 8.6. Optical transmission spectrum for a SnO_2 film.

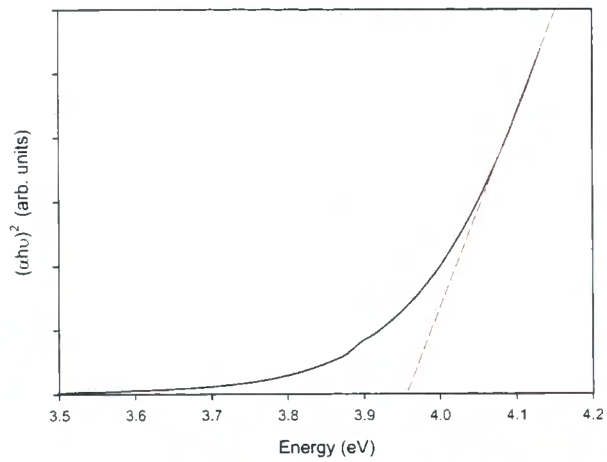

Figure 8.7. Absorption coefficient plot for a SnO_2 film.

The thickness of the film was calculated from the wavelength position of interference peaks in the transmission spectra:

$$d = \frac{\lambda_1 \lambda_2}{2n_{SnO_2}(\lambda_1 - \lambda_2)} \qquad (8.2)$$

where d is the film thickness, n_{SnO_2} is the refractive index of SnO_2 which is taken to be 1.90 [8], and λ_1 and λ_2 are the wavelength positions of successive peaks or troughs in the transmission spectra. By taking four pairs of λ values the thickness of the SnO_2 film was found to be 860 ± 27 nm.

8.5.1.2. Electrical

Simple two point probe measurements were carried out on SnO_2 films; the indicated sheet resistance was of the order of 200-300 $\Omega\square^{-1}$, although this value may be subject to significant experimental error. This is around 20-30 times that of a typical substrate used in cell production, however this was found to be satisfactory for this preliminary study.

8.5.2. CdS

8.5.2.1. Optical transmission

An optical transmission spectrum for a typical CdS film (grown on plain borosilicate glass with no SnO_2 layer) is shown in Figure 8.8, note that the transmission scale has been normalised to one as the geometry of the measurement precluded absolute transmission levels to be calculated. This exhibits a cut-off in transmission around the 2.5 eV region as expected. The bandgap (calculated from the intersection of $(\alpha h\nu)^2$ with the energy axis, Figure 8.9) was found to be 2.34 eV, this is small in comparison with bandgaps of other as-grown CdS films in this work. This difference is likely to be due to modifications within the film (for instance a different level of strain or a different crystalline phase) due to the rapid growth rate and the subsequent modification in the nucleation process. This feature will be explored further in future work.

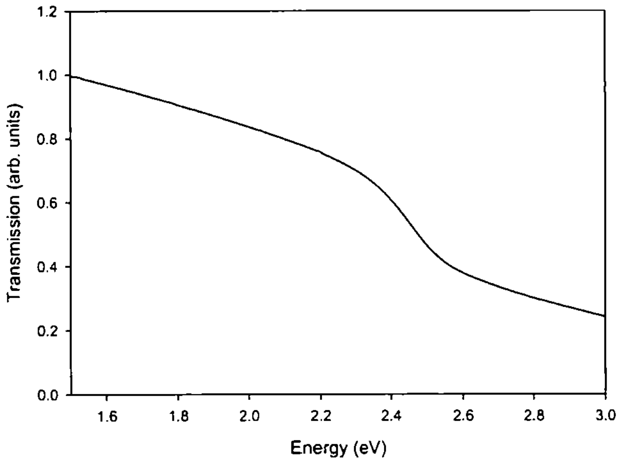

Figure 8.8. Optical transmission spectrum for a CdS film.

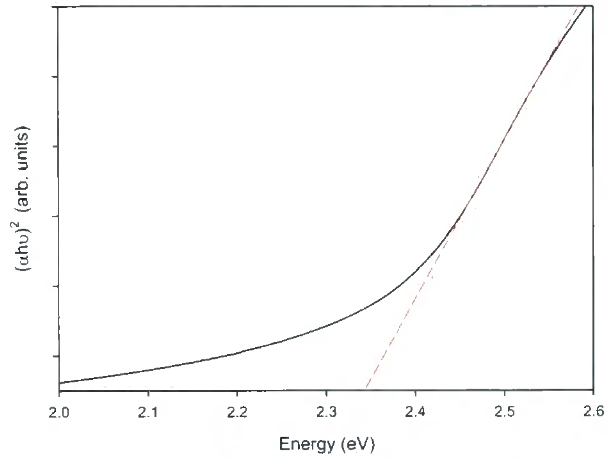

Figure 8.9. Absorption coefficient plot for a CdS film.

8.5.3. CdTe

Figure 8.10 shows an image of three tubular substrates, the first was coated with an 860 nm thick SnO_2 layer, the second was coated with a further 200 nm thick CdS layer and the third was further subjected to an air annealing treatment at 400°C for 20 minutes (hence the colour change of the CdS - refer to section 6.2.2.1), followed by ED growth of CdTe. This layer of approximately 100 nm thickness was deposited on a 4mm length near the bottom of the tube (indicated by the black square in Figure 8.10). Only 100 nm of CdTe was deposited as this was an experimental run in order to gauge the uniformity of growth, although 100 nm CdTe is enough to produce a depletion region with CdS, a thicker film of the order of 2 μm would be required in order to create a working device, this thickness can be easily achieved by allowing the deposition to run for a longer period of time.

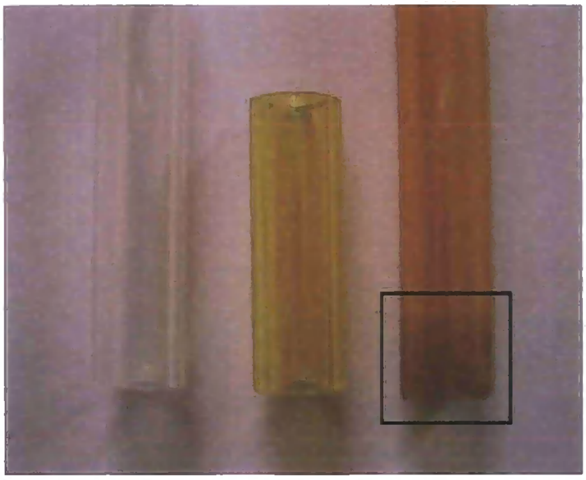

Figure 8.10. Images of tubular PV structures. a) SnO_2 (860 nm) coated substrate, b) SnO_2 (860 nm) substrate with CdS (200 nm) and c) SnO_2 (860 nm) substrate with CdS (200 nm) and a 4mm long 100 nm thick CdTe layer (indicated by the square area near to the bottom of the tube).

Work is currently underway to grow these thicker CdTe layers and a working device with an electrolyte back contact will be demonstrated in the near future, this will be the first ever current generating realisation of this novel device structure.

8.6. References

1. Weinstein, H. and R.H. Lee, *Tubular Solar Cell*, United Sates Patent Office, 3990914, Sensor Technology, Inc., 1976.

2. Zweibel, K., *Issues in thin film PV manufacturing cost reduction.* Solar Energy Materials and Solar Cells, 1999. **59**(1-2): p. 1-18.

3. Boyle, D.S., P. O'Brien, D.J. Otway, and O. Robbe, *Novel approach to the deposition of CdS by chemical bath deposition: the deposition of crystalline thin films of CdS from acidic baths.* Journal of Materials Chemistry, 1999. **9**(3): p. 725-729.

4. Archbold, M.D., D.P. Halliday, K. Durose, T.P.A. Hase, D.S. Boyle, and K. Govender. *Characterization of thin film cadmium sulfide grown using a modified chemical bath deposition process.* in *31st IEEE Photovoltaics Conference.* 2005. Florida, USA.

5. Duffy, N.W., D. Lane, M.E. Ozsan, L.M. Peter, K.D. Rogers, and R.L. Wang, *Structural and spectroscopic studies of CdS/CdTe heterojunction cells fabricated by electrodeposition.* Thin Solid Films, 2000. **361**: p. 314-320.

6. Duffy, N.W., L.M. Peter, and R.L. Wang, *Characterisation of CdS vertical bar CdTe heterojunctions by photocurrent spectroscopy and electrolyte electroreflectance/absorbance spectroscopy (EEA/EER).* Journal of Electroanalytical Chemistry, 2002. **532**(1-2): p. 207-214.

7. Duffy, N.W., L.M. Peter, R.L. Wang, D.W. Lane, and K.D. Rogers, *Electrodeposition and characterisation of CdTe films for solar cell applications.* Electrochimica Acta, 2000. **45**(20): p. 3355-3365.

8. Jimenez, V.M., J.P. Espinos, A. Caballero, L. Contreras, A. Fernandez, A. Justo, and A.R. Gonzalez-Elipe, *SnO2 thin films prepared by ion beam induced CVD: preparation and characterization by X-ray absorption spectroscopy.* Thin Solid Films, 1999. **353**(1-2): p. 113-123.

9. Conclusions

9.1. Summary

This thesis has investigated how different growth methods can influence the structural, electrical and chemical properties of polycrystalline CdS thin films. In addition, the link between the properties of these films and the performance of CdS/CdTe photovoltaic devices made from them has been investigated in detail. During the course of this work a novel solution deposition method has been devised, novel work has been carried out towards the first ever realisation of a tubular geometry photovoltaic device, and many characterisation techniques have been both improved and used in an original manner.

Chapter 1 explored the motivation and goals of the work as well as a discussion of some historical background and a short synopsis of the current status of research into thin film photovoltaics.

Chapter 2 gave a detailed account of the physics of semiconductor materials, the photovoltaic effect and the operation of a *p-n* junction device. This was extended with a discussion of the main parameters used to characterise photovoltaic devices and how non-ideal junction behaviour affects these parameters.

Chapter 3 discussed issues regarding specifically the CdS/CdTe photovoltaic device, including the components of a typical structure and the growth and treatment methods used. Finally there was a discussion of the important environmental and safety implications of using cadmium in production photovoltaics.

In chapter 4 the characterisation techniques used throughout this work were discussed in detail, this included improvements and major modifications made to photoluminescence hardware and software and IV characterisation software.

In chapter 5 a novel thin film deposition system was described. This has several advantages over conventional solution deposition methods: i) a novel nitrogen bubbling system reduced the occurrence of pinholes in growing films, ii) a low temperature EN chemical route was used in order to reduce homogeneous particle formation, eliminate the use of hazardous ammonia and also reduce the amount of Cd wastage by an order of magnitude (between 20-40 times) compared to conventional ammonia based chemistries and iii) a rectangular bath geometry was employed in order to ensure a uniform temperature distribution and therefore produce films with an even thickness over a large area. Good quality films were then grown, and shown to have stoichiometry close to unity, possess a clear bandgap of 2.42 eV (a value which does not change with film thickness) and to be highly oriented in either the h[002] or c[111] direction. A nucleation study was performed in order to investigate the process of initial film formation, and an ICP-MS study showed that impurities present in SD starting solutions are incorporated into growing films in significant amounts. This is an important finding for these materials and devices

Chapter 6 showed that annealing treatments radically affected the properties of CdS films. This is a key result as CdS/CdTe devices are generally subjected to a high temperature $CdCl_2$ anneal in order to maximise performance. Examination by SEM showed that significant modification to the surface morphology occurs upon annealing with $CdCl_2$; further examination by GIRXD showed that a definite conversion to the polycrystalline hexagonal CdS modification occurs. This evidence, along with optical transmission data also suggest a significant reduction in strain within the films upon $CdCl_2$, annealing, further supported by EEA spectra that show a significant increase in crystalline quality. In addition, CV scans somewhat unexpectedly showed that the films are either porous or contain some discontinuities.
A doping study investigated the inclusion of dopant species (In, B, Cu, Ag and Mn) in CdS films, structural investigations proved inconclusive, however there was some modification to optical transmission properties that warrant further study. ICP-MS confirmed the presence of selected dopants in these films.
CSS films were then investigated alongside novel H1 and H2 type hybrid films. Major differences in surface morphology were evident by SEM investigation.

In chapter 7 the results of full CdS/CdTe PV device structures were described. Devices were fabricated with SD, CSS and types H1 and H2 hybrid CdS. All devices with CdTe and back contact grown at Durham showed generally disappointing efficiency values in the region of 0-3.9%. Devices fabricated with CdTe and back contact at Parma showed much better performance, with an un-optimised figure of 9.8% for one of only two devices produced. This device data suggests that the SD method developed throughout this work shows good potential for the production of CdS for thin film photovoltaic devices.

In chapter 8 novel work was presented on the first ever practical realisation of a tubular photovoltaic structure. This was discussed in terms of its potential in reducing manufacturing costs, realising efficiency gains and the exciting possibility of creating PV/solar thermal hybrid devices. Growth methods used in this study were described and then results of an early stage prototype were presented. Future work in this area will aim to produce the first operational, current generating photovoltaic device of this class.